Title
Vacuum UV study of photodissociation of CS and C2

Author
Xu, Zhongxing

Publication Date
2021

Peer reviewed|Thesis/dissertation

Vacuum UV study of photodissociation of CS and C_2

By

ZHONGXING XU

DISSERTATION

Submitted in partial satisfaction of the requirements for the degree of

DOCTOR OF PHILOSOPHY

in

Chemistry

in the

OFFICE OF GRADUATE STUDIES

of the

UNIVERSITY OF CALIFORNIA

DAVIS

Approved:

Kyle N. Crabtree, Chair

Cheuk-Yiu Ng

Lee-Ping Wang

Committee in Charge

2021

Contents

Vacuum UV study of photodissociation of CS and C_2

Abstract

Photodissociation by ultraviolet (UV) radiation is a key destruction pathway for small molecules in regions where the interstellar UV radiation can penetrate, such as the diffuse molecular clouds, protoplanetary disks, and photon-dominated regions. Wavelength-dependent photodissociation data is a critical input for accurately modeling the physical and chemical evolution of these astronomical environments. Carbon monosulfide (CS) and dicarbon (C_2) are two transient molecules widely detected in space and they play important roles in carbon chemistry and/or sulfur chemistry. However, due to the lack of high-resolution laboratory studies and high-level quantum calculations focusing on photodissociation through their highly excited states, their photodissociation cross sections in modern astrochemical models have large uncertainties. Based on previous studies, the $C\,^1\Sigma^+$ state of CS and the $F\,^1\Pi_u$ state of C_2 are predissociative Rydberg states and are considered to be important for their photodissociation. In this dissertation, a combination of laboratory vacuum UV (VUV) spectroscopy and high-level *ab initio* quantum chemical calculations are performed to provide a better set of photodissociation data for CS and C_2.

For the theoretical calculation part, potential energy curves of CS and C_2 electronic states are calculated at the SA-CASSCF/MRCI+Q level using Dunning quintuple-zeta basis sets with additional diffuse functions. By including several additional σ (CS) and σ_g (C_2) molecular orbitals beyond valence orbitals into the active space, the Rydberg nature of these states are successfully obtained. Coupled-channel models involving the $C\,^1\Sigma^+$ state of CS and the $F\,^1\Pi_u$ state of C_2 are built by combining potential energy curves and related transition dipole moments, nonadiabatic couplings, and spin-orbit couplings. The photodissociation cross sections obtained by solving the coupled-channel model are used to calculate the photodissociation rate of CS and C_2 in standard interstellar radiation fields and other astronomical environments.

Experimentally, a state-selective photodissociation study using the vacuum ultraviolet laser pump-probe velocity-map imaging (VUV-VUV-VMI) technique was initiated. CS and C_2 are successfully generated by photolysis of CS_2 and laser ablation of a graphite rod, respectively. A tentative signal is observed in the region where the $C - X$ transition of CS is expected, however, owing to the high vibrational temperature of CS in the experiment, further work is needed. The future plan is to build an electrical discharge source to obtain CS with a cooler vibrational distribution. Besides the main project, the direct C + S_2 channel

in CS_2 photodissociation has been observed, and a new highly accurate photoionization energy for C_3 as 11.8341 ± 0.0025 eV has been derived. Despite the delay of the experimental progress, the photodissociation cross sections obtained in the theoretical part of this dissertation provide much needed improvements to the astrochemical models used to simulate astrochemistry in the diffuse interstellar medium.

Acknowledgments

I would first express sincerest thanks to my advisor, Prof. Kyle Crabtree for his support and guidance during my Ph.D. studies. His enthusiasm for both science and life inspired and infected me profoundly. Kyle is always ready to share his knowledge and skills with me and provide all kinds of support he is able to provide. I'm grateful for the opportunities to work on this NASA photodissociation project, to collaborate with others, and to attend academic conferences. From these experiences, I learned how to present my ideas and work and how to carry on experimental and theoretical studies. I would have been unable to finish my Ph.D program and become a independent researcher without his input. Also I'd like to thank Kyle for his help in improving my language skills during preparation of this dissertation.

Prof. Cheuk-Yiu Ng, Prof. Lee-Ping Wang, Prof. William M. Jackson, and Prof. S. R. Federman are collaborators on the NASA photodissociation program. I've been very lucky to work with all these experts in different fields with a broad range of skills and experiences. I'd like to thank Prof. Ng and Prof. Jackson for the chance to carry out experiments with the state of the art vacuum ultraviolet laser pump-probe velocity-map imaging apparatus in their lab. They shared their technical knowledge and scientific skills in photodissociation spectroscopy accumulated over so many years for me unreservedly. I extend my sincere thanks to Lee-ping for his training and guidance in computational methodologies. Lee-Ping contributed heavily to the work presented in Chapters 3 and 4 of this dissertation. Thanks also to Prof. Federman for insightful conversations on astronomical observations and theoretical modeling over the years. Here, I'd like to thank Prof. Cheuk-Yiu Ng and Prof. Lee-Ping Wang a second time for serving as my dissertation committee members and polishing this dissertation.

I want to thank Dr. Yih Chung Chang (Ian) for his mentorship and assistance. He trained me to operate and maintain the complicated apparatus. We carried out experiments together for almost two years. After that, he has helped me to troubleshoot experimental issues several times. I learned some data processing skills from Ian too. I am also grateful to Dr. Yuntao Xu for his help in my experimental studies. Dr. Yudong Qiu guided me on how to do MRCI calculations using the Molpro program when I started the theoretical work. I'd like to recognize the help that I received from him.

It's a really enjoyable memory to work with a group of talented and intelligent labmates in Crabtree lab. I would like to give special thanks to Sommer Johansen and Zachary Buchanan. In first two years of my graduate school, we worked together to set up the kinetics instrument from scratch. During our collaboration,

I've been inspired and motivated by their problem-solving approaches. I'd also like to acknowledge Kelly Meyer for her enthusiasm in life and confidence, which are infectious. Nan Luo worked with me as an undergraduate student researcher. I'd like to thank Alan Hicklin for teaching me machining skills and all his engineering knowledge. I am grateful to him for trusting me and being a mentor for me. Although I didn't work with the rest of Crabtree lab directly, we shared our knowledge during group meetings over the past years. It was a memorable and special experience to be a Crabtree lab member.

My project also relies on support from the Chemistry department. I'd like to thank Scott Berg from the machine shop, Paul Stucky from the electronic shop, and DeAnn Ronning as a purchaser.

Last but not least, I'd like to thank my parents for their continuous love, support, and encouragement throughout my whole life. Also, I would like to thank all my friends for a cherished time spent together along the way, especially Jose Antonio Flores for his support and companionship during the past two years. Gracias.

CHAPTER 1

Introduction

The overarching motivation for the work presented in this dissertation is to study the photodissociation process of transient diatomic molecules, such as CS and C_2. This topic is particularly interesting in the contexts of astrochemistry, spectroscopy and quantum chemistry. In short, photodissociation of CS and C_2 play important roles in the astrochemistry of photon-dominated regions. Accurate wavelength-dependent photodissociation cross sections are required to build astrochemical and astrophysical models of those environments. However photodissociation is challenging to study both experimentally and theoretically, especially in the vacuum ultraviolet (VUV) range (<200 nm or >6.2 eV) where CS and C_2 have strong transitions. Experimental high-resolution spectroscopy in this region requires producing tunable VUV light with narrow spectral linewidths. From a theoretical perspective, accurate calculations of the electronic energies of highly excited states and the proper treatment of predissociation, which is a dynamic process, are required. The work presented in this dissertation combines experimental studies and theoretical calculations to provide new quantitative information on the photodissociation of CS and C_2 for astrophysical applications. The results of this study provide more accurate photodissociation cross sections for astrochemical models and may serve as examples for further investigations on photodissociation processes.

1.1. Astrochemistry and astrochemical models

Benefiting from the development of telescopes, especially the construction of a powerful new interferometric telescope ALMA (Atacama Large Millimeter/submillimeter Array), more than 250 unique molecules have been detected in space, indicative of a rich, diverse chemistry (McGuire, 2018). The discipline of astrochemistry, an overlap of astronomy and chemistry, developed throughout the mid to late 20th century to answer questions about how those molecules in space, especially in interstellar clouds, are formed, how they interact with other atoms and molecules, what other molecules may exist in space, and the possibility that life can originate from chemistry in space. The observations of reactive species and radicals indicates the interstellar medium is not in thermodynamic equilibrium. Modern astrochemistry uses chemical models

that combine gas-phase, condensed-phase, and photochemical processes to study the physical and chemical evolution of the Universe. The astrochemical models can predict the time evolution and steady-state solution of the chemical composition of a number of atomic and molecular species, both detected and not detected. The inputs of the models include the overall initial composition of the medium and the physical conditions of specific astronomical environments, such as temperature, density, radiation field, and cosmic rays.

Mathematically, an astrochemical model with N atomic and molecular species solves a set of N coupled ordinary differential equations (ODEs), one for the abundance evolution of each species,

$$\frac{dn_i}{dt} = \Sigma_{\text{production}} - \Sigma_{\text{destruction}} \tag{1.1}$$

where n_i is the abundance of species i, while the $\Sigma_{\text{production}}$ and $\Sigma_{\text{destruction}}$ are all chemical and physical processes that produce and destroy this species. In the interstellar medium, the most common reactions are two-body collisions and photon-induced radiative processes. Three-body reactions are normally neglected as they are unlikely owing to the low density of chemical species in those environments. Thus, the above formula can be expanded as

$$\begin{aligned}\frac{dn_i}{dt} =& \Sigma_{a,b} k_{a,b}(T) n_a n_b + \Sigma_{\text{ph}} \Sigma_a k_{a,\text{ph}} n_a \\ & - \Sigma_{a,i} k_{a,i}(T) n_a n_i - \Sigma_{\text{ph}} k_{i,\text{ph}} n_i\end{aligned} \tag{1.2}$$

The first term is the formation of species i from a collision reaction between species a and b with a temperature dependent reaction rate coefficient $k_{a,b}(T)$. The second term describes the formation of species i from all possible photoprocesses of other species $a \neq i$, including photodissociation, photoionization, and photodetachment. The photon-induced reaction rate $k_{a,\text{ph}}$ is obtained by integrating the product of light intensity and the corresponding cross section over the photon wavelength or frequency:

$$k = \int \sigma(\lambda) I(\lambda) d\lambda, \tag{1.3}$$

where the $\sigma(\lambda)$ is the wavelength-dependent photodissociation cross section and $I(\lambda)$ is the wavelength-dependent radiation intensity of the radiation field interested. The third and fourth terms represent the destruction of species i due to collision with species a with the reaction rate $k_{a,i}(T)$ and photoprocesses with rate $k_{i,\text{ph}}$. The set of coupled ODEs can be solved numerically as a function of time to a certain desired

precision. Critically, the models depend on accurate parameters for calculating the rates of reactions (eg. rate coefficients, cross sections, etc.) (Agúndez & Wakelam, 2013).

Thus, many experimental and theoretical efforts have been made to obtain accurate values for these parameters under astrophysically relevant conditions, and a number of publicly available database provide compilations for use in astrochemical models. The KInetic Database for Astrochemistry (KIDA) online database provides a summary of rate coefficients from previous studies (Wakelam et al., 2015). It was established mainly based on the OSU database, which was initially developed in 1980 (Prasad & Huntress, 1980) and then updated by Eric Herbst and collaborators, with many additions from new experimental and/or theoretical studies. The KIDA network, as updated in 2014, contains a total of 7509 reactions for 489 chemical species. The simulation from this network is in good agreement with observations in TMC-1 for the most abundant small molecules. However, the modeled and observed abundances for more complex species show large differences, indicating that either key chemical reactions are missing or poor kinetic data are available for part of the network. Also, unstable radicals, which may play important roles in neutral-neutral reactions, are underrepresented in the database owing to a lack of experimental and theoretical data. The UDFA (UMIST Database for Astrochemistry) is another main chemical reaction database which is similar to KIDA (McElroy et al., 2013). The Leiden Atomic and Molecular Database (LAMDA) collects spectroscopic and collisional data for molecules of astrochemical interest focusing on non-Local Thermodynamic Equilibrium (LTE) conditions (Schöier et al., 2005). The Leiden photodissociation and photoionization database focuses on radiative processes of astrophysically relevant molecules (Heays et al., 2017). PHoto Ionization/Dissociation RATES (PHIDRATES) is another database focusing on photoprocesses important for the solar system (Huebner & Mukherjee, 2015). A more in-depth introduction to astrochemistry is presented by Yamamoto (2017) and Lique (2019). Herbst & van Dishoeck (2009) and Tielens (2013) reviewed the chemical models used in studying complex organic molecules in the interstellar medium (ISM). Smith (2011) provided an thorough discussion about the experimental methods used to obtain kinetic data for gas-phase chemical reactions.

1.2. Photodissociation of small molecules in astrochemical environments

Photodissociation, photolysis, or photodecomposition is a type of chemical reaction which can be represented as

$$AB + h\nu \rightarrow A + B \tag{1.4}$$

where $h\nu$ is the photon, AB is the parent compound, while A and B are the atomic or molecular fragments from the photodissociation. For small molecules, the photodissociation is the combination of two different mechanisms, direct photodissociation and predissociation. When a UV photon absorbed, the molecule in its ground state or a low lying excited state is promoted into a high energy excited state. If the excited state is unbound, direct photodissociation occurs. In this case, the photoabsorption and photodissociation cross section is broad and smooth as a function of wavelength. If the excited state is bound, then the absorption can be resolved into lines corresponding to rotational and vibrational transitions. In this case, the upper state may be coupled with other unbound states through one or more processes. The nonradiative transition from a bound state to a dissociate state is called predissociation. Compared to direct dissociation, the predissociation cross section varies greatly with wavelength.

Photochemistry plays an important role in the formation and dissociation of many molecules in space. In regions where UV radiation is abundant, such as the diffuse ISM, photon-dominated regions (PDRs) and protoplanetary disks (PPDs), photodissociation by ultraviolet (UV) radiation is a key destruction pathway for small molecules (Snow & McCall, 2006; van Dishoeck et al., 2006). In some cases, the generated atoms and/or molecular fragments are in long-lived metastable states. Their extra internal energy may trigger subsequent chemical reactions, which is not considered in most astrochemical models. In addition, the UV flux and physical conditions vary strongly in different environments, and are often heterogeneous within the same object. Thus state-specific molecular data, including photodissociation cross sections and photoproduct branching fractions, are critical inputs to astrochemical models for accurately modeling chemical evolution in UV-rich environments.

As shown in Equation (1.3), the photodissociation rate depends on the wavelength-dependent intensity of the radiation field. A typical radiation field is the standard interstellar radiation field (ISRF) in ISM given

by Draine (1978), which is given by

$$I(\lambda) = 3.2028 \times 10^{13} \cdot \lambda^{-3} - 5.1542 \times 10^{15} \cdot \lambda^{-4} + 2.0546 \times 10^{17} \cdot \lambda^{-5} \text{ photons cm}^{-2} \text{ s}^{-1} \text{ nm}^{-1} \tag{1.5}$$

in the wavelength range 91.2 to 200 nm. Since atomic H is the most abundant species in ISM, any photons with energy larger than its ionization limit 13.6 eV, or wavelength shorter than 91.2 nm, are fully shielded by atomic H. Another important wavelength 121.6 nm, is Lyman-α (or Lyα),corresponding to the Lyman-α atomic H transition from an $n = 2$ orbital to $n = 1$ ground state. In some environments, such as young stars (Schindhelm et al., 2012) and accretion shocks (Herczeg et al., 2004), Lyman-α dominates the radiation field. The accuracy of photodissociation rates of molecules heavily depends on their photodissociation cross sections around the Lyman-α wavelength.

1.3. CS and C_2 in space

Carbon monosulfide (CS) and dicarbon (C_2) are two important C-bearing transient molecules in space. Both molecules have been detected in a number of sources, most often in diffuse clouds and comets (Donati, 1864; Drdla et al., 1989; Heithausen et al., 1998; Lambert & Mallia, 1974; McQuinn et al., 2002; Scappini et al., 2007; Sonnentrucker et al., 2007; Wehres et al., 2010; Wollaston, 1802; Zuckerman et al., 1972). The chemical network for CS and C_2 in diffuse clouds in modern astrochemical models is shown in Figure 1.1 (Neufeld et al., 2015; Yamamoto, 2017). CS is formed following the production of CS^+ through

$$S^+ + CH \longrightarrow CS^+ + H, \tag{1.6}$$

production of HCS^+ through

$$CS^+ + H_2 \longrightarrow HCS^+ + H, \tag{1.7}$$

and electronic dissociative recombination of HCS^+:

$$HCS^+ + e^- \longrightarrow CS + H. \tag{1.8}$$

C_2 is formed following a series of reactions whose rate-limiting step is

$$C^+ + CH \longrightarrow {C_2}^+ + H, \tag{1.9}$$

although C_2^+ has not been detected. In the diffuse ISM, photodissociation is the dominant destruction pathway for CS and is one of the important destruction pathways for C_2, competing with the reactions

$$C_2 + O \longrightarrow CO + C \tag{1.10}$$

and

$$C_2 + N \longrightarrow CN + C. \tag{1.11}$$

As possible photodissociation products, metastable carbon and sulfur in their ^1S and ^1D states have long lifetimes (for example, 3436 s for ^1D of C) and in more dense environments may be involved in other gas phase reactions which are not possible for carbon and sulfur in the ground states. Despite the key role that photodissociation plays in the chemistry of CS and C_2 in space, little-to-no laboratory or theoretical photodissociation data are available. The most recent update to the Leiden photodissociation and photoionization database indicates that the interstellar photodissociation rate for CS is uncertain to a factor of 10, while that for C_2 is uncertain to a factor of 2 (Heays et al., 2017). Moreover, sulfur chemistry in space is not well understood in different interstellar and circumstellar environments, as current astrochemical models are unable to reproduce the distributions of sulfur-bearing species (Le Gal et al., 2019). Thus, the main goal of this dissertation is to study the photodissociation process of CS and C_2 and provide more accurate photodissociation cross sections and rates. More detailed discussions of the current state of knowledge for each species can be found in Chapters 3 and 4.

1.4. Structure of this dissertation

To understand the topics discussed in this dissertation, comprehensive theoretical underpinnings are required. While it is impossible to discuss all the related information exhaustively here, Chapter 2 outlines the information which is most relevant to the work that follows, including basic spectroscopic and quantum-mechanical knowledge. As mentioned above, the two challenges for theoretical calculations are the high accuracy required for the electronic energies and potential energy curves of highly excited states and proper treatment of predissociation as a dynamic process. The former is met by applying the multi-reference calculation methods CASSCF and MRCI+Q, while the latter requires the treatment of nuclear dynamics beyond the Born-Oppenheimer approximation. Those are the focus of this Chapter.

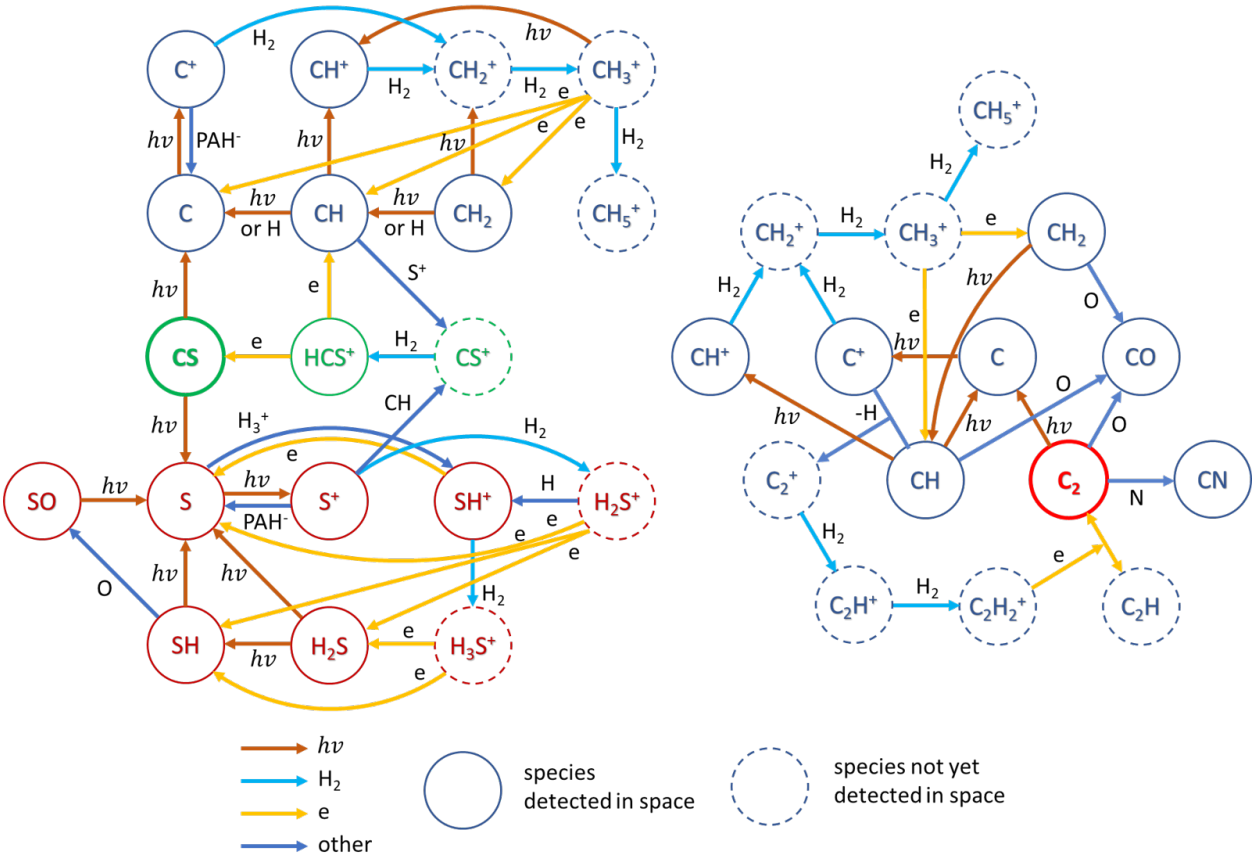

FIGURE 1.1. Chemical network of CS (left) and C_2 (right) in diffuse clouds. Solid outline circles represent species that have been detected in space while the dashed outline circles represent species that have not been detected so far. Some reactions are only shown in one of the two chemical networks.

In Chapters 3 and 4, the detailed theoretical studies on the photodissociation of CS and C_2 are presented. Each presents a brief review of prior experimental and theoretical studies, followed by original work on the calculation of their photodissociation cross sections, focusing on the $C\,^1\Sigma^+ - X\,^1\Sigma^+$ band of CS and the $F\,^1\Pi_u - X\,^1\Sigma_g^+$ band of C_2, using the methods introduced in Chapter 2. In summary, the electronic potential energy curves of their ground and excited states were calculated using the method CASSCF followed by MRCI+Q with the Dunning basis sets aug-cc-pVXZ augmented with additional Rydberg diffuse functions. Inspired by spectroscopic evidence that the excited states $C\,^1\Sigma^+$ of CS and $F\,^1\Pi_u$ of C_2 are Rydberg states, the active spaces used in the CASSCF and MRCI+Q calculations include additional molecular orbitals beyond valence orbitals. Combining the PECs with calculated spin-orbit couplings and non-adiabatic couplings, coupled-channel models are built to solve for the photodissociation cross sections.

The most direct way to obtain the cross sections would be from experimental measurements. However, such experimental work is even more challenging than theoretical calculations. One key difficulty involves the preparation and manipulation of transient molecules. To obtain the desired spectrum, they must be produced *in situ*, in the ground vibronic states, which is more complicated than studying on stable molecules like N_2, O_2, and CO_2. A second difficulty is producing tunable VUV radiation for probing the target molecules CS and C_2, which is accomplished by the four-wave mixing technique. The advantage of this technique is that the laser can be tuned over a wide range with fairly high spectral resolution as $0.45\,\mathrm{cm}^{-1}$. However, the VUV system is technically complex and requires frequent alignment and maintenance work. Unfortunately, due instrumental failures requiring lengthy repairs coupled with COVID pandemic, the experimental work was severely impacted, and consequently experimental cross sections for CS and C_2 are not yet available. The current status of the experimental work to date is presented in Chapters 5 and 6. For the molecule CS, it has been verified that the photodissociation of CS_2 generates CS, albeit in highly excited vibrational states. Relaxation of vibrationally excited CS to the vibrational ground state will be required for improving the sensitivity of the spectroscopy. As the side product of this research, we found that photodissociation of CS_2 can also lead to the C + S_2 channel. For the molecule C_2, we succeeded in generating C_2 from the laser ablation of a graphite rod. Also as the side product of this research, we determined a highly accurate photoionization threshold of C_3, another molecule generated by laser ablation.

In conclusion, the theoretical calculations presented in this dissertation have obtained highly reliable photodissociation data which are useful for astrochemical models. The ongoing experiments will provide new benchmarks for studying the excited electronic structures and predissociation of diatomic molecules.

CHAPTER 2

Spectroscopy and predissociation of diatomic molecules

The history of physical chemistry and spectroscopy are closely connected with each other as interactions with photons reveal the internal structures of atoms and molecules. Unlike the discrete lines found in atomic spectra, molecular spectra contain bands composed of many individual lines. The bands correspond to rotational and vibrational transitions between different electronic states or within the same electronic state and contain information about both electronic and nuclear structure. Organizing and assigning the spectral bands and lines to specific transitions is how scientists discovered the different quantum numbers and parities of states. Meanwhile, theoretical chemists have explored the quantum chemistry of molecules from first principles. Experimental spectra have provided important benchmarks for the development of theoretical methods.

Photodissociation spectroscopy is able to reveal structural information about highly excited electronic states of molecules. It is also the ideal tool to study certain molecular dynamics processes, such as the breaking and formation of chemical bonds and energy transfer between different electronic states on a state-to-state level. Diatomic molecules, which are the simplest molecules, are unique owing to their linear structure, high symmetry and single vibrational mode, and they are the ideal molecules for fundamental photodissociation studies. As such the spectroscopy and photodissociation of diatomic molecules have been the subject of numerous experimental and theoretical investigations. This chapter presents the basic principles behind photodissociation.

It is impossible to provide a comprehensive review of the extensive diatomic spectroscopy literature here. The following works have deeper discussions on this topic and serve as the main references for this chapter. More detailed discussions of diatomic spectroscopy are well presented by Herzberg & Spinks (1950), Lefebvre-Brion & Field (2004), and Bernath (2016). A short summary focusing on photodissociation of diatomic molecules is given by Heays et al. (2010) in his Ph.D. dissertation. The role of radiative processes in astrophysics and astrochemistry is reviewed in Chapter 4 of the book "Gas-Phase Chemistry in Space"

(Lique, 2019). Nakamura (2002) discussed the fundamental mechanism and basic theories of nonadiabatic transitions.

2.1. Simple spectra and notations

The total internal energy E^T of diatomic molecules can be broken into three parts: rotational $F(J)$, vibrational $G(v)$, and electronic T_e energies:

$$E^T = T_e + G(v) + F(J). \tag{2.1}$$

Although a full understanding requires quantum chemistry knowledge, it is still possible to give some basic conclusions without involving too many theoretical details. Indeed, some of the formulas were first obtained empirically in the history of spectroscopy.

Using the rigid rotor model to represent the rotational states, the rotational energy can be described as a power series in rotational quantum number ($J = 0, 1, 2, \cdots$):

$$F(J) = B_v J(J+1) - D_v[J(J+1)]^2 + H_v[J(J+1)]^3 - \cdots, \tag{2.2}$$

where B_v is the rotational constant of the v-th vibrational state, and D_v and H_v are the centrifugal distortion constants for this vibrational state. Empirically, B_v can be written as

$$B_v = B_e - \alpha_e(v + \frac{1}{2}) + \cdots, \tag{2.3}$$

where B_e is the rotational constant at the equilibrium geometry of the electronic state and α_e is a constant term related to the shape of the anharmonic potential. B_e is directly connected to the equilibrium internuclear distance R_e

$$B_e = \frac{\hbar^2}{2I} = \frac{\hbar^2}{2}\frac{1}{\mu R_e^2}. \tag{2.4}$$

The reduced mass μ of a diatomic molecule AB is

$$\mu = \frac{M_A M_B}{M_A + M_B}. \tag{2.5}$$

The vibration of a diatomic molecule can be represented using a harmonic oscillator model. The corresponding vibrational energy is usually written as a function of the vibrational quantum number (v =

$0, 1, 2, \cdots$):

$$G(v) = \omega_e(v + \frac{1}{2}) - \omega_e x_e(v + \frac{1}{2})^2 + \omega_e y_e(v + \frac{1}{2})^3 - \cdots, \tag{2.6}$$

where ω_e is the harmonic vibrational frequency or harmonic vibrational constant, and $\omega_e x_e$ and $\omega_e y_e$ are the second and third order anharmonic vibrational constants, which are related to the shape of the anharmonic potential.

Electronic energies at the equilibrium geometry and at the $v = 0$ state are denoted as T_e and T_0, respectively. There is no general formula to represent the electronic energies of different electronic states of molecules. The exact values of electronic energies are evaluated by experiments or theoretical calculations. In observations of molecular spectra in the UV range, many are found to contain series of Rydberg states similar to those in atoms. Rydberg states can be visualized as an ionic core with one electron in a diffuse Rydberg molecular orbital. Their electronic energies can be described by a modified Rydberg equation:

$$T_0(n) = IP - \frac{R_M}{(n-a)^2}, \tag{2.7}$$

where IP is the ionization potential of the molecule, n is the principal quantum number of the Rydberg state, and a is usually called the quantum defect. R_M is the Rydberg constant for the corresponding ion:

$$R_M = R_\infty \frac{M}{m_e + M}, \quad R_\infty = 109737.318\,\mathrm{cm}^{-1}. \tag{2.8}$$

The above formula is fairly accurate for Rydberg states with high principal quantum numbers n. Lower Rydberg states are often mixed with valence states, and consequently deviate from this formula.

Though less commonly used in the modern literature, rotational and vibrational energy bands have also been represented by the Dunham expansion:

$$D_{v,J} = \sum_{k,l} Y_{k,l}(v + \frac{1}{2})^k [J(J+1)]^l, \tag{2.9}$$

where the coefficients $Y_{k,l}$ are called Dunham parameters. It is straightforward to recognize that the $Y_{00} = T_e$, $Y_{10} = \omega_e$, $Y_{20} = -\omega_e x_e$, $Y_{30} = \omega_e y_e$, $Y_{0,1} = B_e$, $Y_{0,2} = -D_e$, and $Y_{1,1} = -\alpha_e$ in the above equations. Truncation of the terms k, l depends on the desired accuracy and the number of observed vibrational and rotational levels.

2.2. Electronic states of diatomic molecules and angular momentum

Angular momentum plays a central role in atomic and molecular physics. No matter the source, angular momentum behaves mathematically the same in quantum mechanics. For an angular momentum operator $\hat{\mathbf{X}}$, the eigenvalue of $\hat{\mathbf{X}}^2$ is $\hbar^2 x(x+1)$, where x is an integer or half-integer representing the total angular momentum. $\hat{\mathbf{X}}$ has three components $\hat{\mathbf{X}}_x$, $\hat{\mathbf{X}}_y$, and $\hat{\mathbf{X}}_z$, which are the projections of $\hat{\mathbf{X}}$ on x, y, or z axis in space. The eigenvalues of $\hat{\mathbf{X}}_i, (i = x, y, z)$ are $\hbar m_x$, where $m_x = -x, -x+1, \cdots, x-1, x$. $\hat{\mathbf{X}}^2$ commutes with all the three components of $\hat{\mathbf{X}}$:

$$[\hat{\mathbf{X}}^2, \hat{\mathbf{X}}_i] = 0 \quad \text{for} \quad i = x, y, z, \tag{2.10}$$

while the three components do not commute with each other:

$$[\hat{\mathbf{X}}_i, \hat{\mathbf{X}}_j] = i\hbar\varepsilon_{ijk}\hat{\mathbf{X}}_k, \tag{2.11}$$

where ε_{ijk} is the Levi-Civita symbol. So simultaneously eigenstates can only be chosen for $\hat{\mathbf{X}}^2$ and one of the components.

There is no general formula to predict the energies of electronic states and there is no single quantum number which could be used to list them energetically from low to high. Because the total angular momentum $\hat{\mathbf{F}}$ always commutes with the Hamiltonian, it is always possible to label eigenstates with angular momentum quantum numbers. Often, many components of angular momentum also nearly commute with the Hamiltonian, and could therefore be chosen as suitable basis vectors. A convenient choice of angular momentum basis set is one that makes the zero-order pattern of the observed energy levels correspond to the chosen angular momentum operators while treating shifts from the pattern as weak couplings between those operators. In other words, the choice of basis set reflects how to represent the unperturbed Hamiltonian H_0 in the particular chemical system.

The most common notation for an electronic state of a diatomic molecule is $\Lambda - S$ notation:

$${}^{2S+1}\Lambda^{(+/-)}_{\Omega,(g/u)}. \tag{2.12}$$

Here, Λ is the projection of the orbital angular momentum $\hat{\mathbf{L}}$ along the internuclear axis. For $|\Lambda| = 0, 1, 2, \cdots$, the symbols $\Sigma, \Pi, \Delta, \cdots$ are used in diatomic molecular spectroscopy to represent them. The term g/u

indicates the parity of the electronic wavefunction with respect to the operation of inversion, and $+/-$ indicates the parity of the electronic wavefunction with respect to a reflection plane containing the internuclear axis. The $\Lambda^{(+/-)}_{(g/u)}$ corresponds to an irreducible representation of the $C_{\infty v}$ or $D_{\infty h}$ point group and represents the spatial symmetry, while $2S+1$ and Ω involve spin angular momentum. Ω is the projection of the total angular momentum exclusive of nuclear spin $\hat{\mathbf{J}} = \hat{\mathbf{R}} + \hat{\mathbf{L}} + \hat{\mathbf{S}}$ along the internuclear axis. S is the total spin quantum number and $2S+1$ is called multiplicity. The projection of $\hat{\mathbf{S}}$ along the internuclear axis is defined as Σ. The relationships among those terms are shown in Figure 2.1. In the figure, $\hat{\mathbf{R}}$ is nuclear-rotational angular momentum.

In the case of a $^1\Sigma$ state, since $\Lambda = 0$ and $S = 0$, the total angular momentum $\hat{\mathbf{J}}$ is just the nuclear rotational angular momentum $\hat{\mathbf{R}}$. The pattern of energy levels and corresponding transitions between $^1\Sigma^+$ states are simple. For molecules not in $^1\Sigma$ states, angular momenta are always coupled with each other, producing more complicated spectral patterns. Depending on the relative magnitudes of different couplings, some angular momenta are unable to represent those patterns well and other angular momenta more clearly organize the patterns. These rules are summarized as Hund's cases (a) to (e). In Hund's case (a), where $\hat{\mathbf{L}}$ is electrostatically coupled to the internuclear axis, spin-orbit coupling is intermediate, and the rotational coupling is weak, the combination of angular momenta

$$|JS\Omega\Lambda\Sigma\rangle \tag{2.13}$$

is a good basis set. Most states of CS and C_2, the molecules of interest in this dissertation, are well described in Hund's case (a).

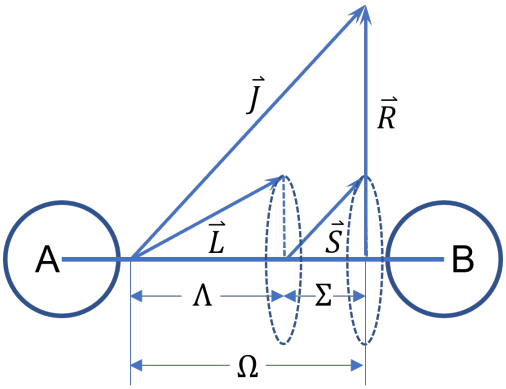

FIGURE 2.1. Angular momenta

To fully represent a molecular state at total energy E, the following basis set can be used:

$$|iEJM\Pi S\Omega\Lambda\Sigma\rangle, \tag{2.14}$$

where M is the quantum number corresponds to $\hat{\mathbf{J}}_z$ with $M = -J, -J+1, \cdots, J-1, J$, Π is the parity + or −, and the index i is used to distinguish possible degenerate states. For a bound state, another vibrational quantum number, v, may replace E in the basis set. Finally, for most of states interest in this dissertation, the following basis set is convenient and sufficient:

$$|ivJM\Pi S\Omega\Lambda\Sigma\rangle. \tag{2.15}$$

Besides the above angular momenta, the total nuclear spin angular momentum $\hat{\mathbf{I}}$ also needs to be considered if it is not zero:

$$\hat{\mathbf{I}} = i_A + i_B, \tag{2.16}$$

where i_A and i_B are the nuclear spins of nuclei A and B. The most abundant isotopes of C and S do not possess spin angular momentum. In C_2, the Pauli exclusion principle causes half of the rotational levels in a given vibronic state to be forbidden. Aside from this, nuclear spin will not be considered further in this dissertation.

2.3. The Born-Oppenheimer approximation

The Schrödinger equation governs quantum chemistry and is the starting point for description of diatomic molecules. The time-independent Schrödinger equation is in the form of

$$\hat{\mathbf{H}}\psi^T = E^T\psi^T, \tag{2.17}$$

where ψ^T is the (possibly degenerate) wavefunction corresponding to the energy level(s) E^T. For the purpose of this work, H is the nonrelativistic Hamiltonian and can be written in atomic units as

$$\hat{\mathbf{H}} = -\frac{1}{2}\left(\frac{\nabla_A^2}{m_A} + \frac{\nabla_B^2}{m_B} + \sum_{i=1}^{n}\nabla_i^2\right) + \sum_{i=1}^{n}\left(\sum_{j=i+1}^{n}\frac{1}{r_{ij}} - \frac{Z_A}{r_{Ai}} - \frac{Z_B}{r_{Bi}}\right) + \frac{Z_A Z_B}{R_{AB}} \tag{2.18}$$

for a diatomic molecule AB with masses m_x and nuclear charges Z_x ($x = A, B$). r_{Ai} and r_{Bi} are the distances between electron i and nuclei A and B. R_{AB} (hereafter R) is the internuclear distance between the nuclei. r_{ij} is the distance between two electrons i and j. n is the total number of electrons. In Equation (2.18), the first term corresponds to the kinetic energies of nuclei A, B and electrons, the second term describes the electron-electron ($e-e$) and electron-nuclei ($e-N$) Coulomb interactions, and the third term represents the nuclear ($N-N$) Coulomb repulsion. It is possible to convert the above equation from a laboratory-fixed axis system into a molecule-fixed axis system by defining the origin as the molecular center of mass (COM), and using R and the spherical polar angles θ and ϕ to specify the molecular orientation in space. The derivation is not straightforward and discussed by Bunker (1968). In this axis system, the Hamiltonian can be broken into several parts, nuclear kinetic energy $\hat{\mathbf{T}}^N$, electronic kinetic energy $\hat{\mathbf{T}}^e$, and electrostatic potential energy $\hat{\mathbf{V}}$:

$$\hat{\mathbf{H}} = \hat{\mathbf{T}}^e(r) + \hat{\mathbf{T}}^N(R,\theta,\phi) + \hat{\mathbf{V}}(r,R), \tag{2.19}$$

where

$$\hat{\mathbf{T}}^e(r) = -\frac{1}{2}\sum_{i=1}^{n} \nabla_i^2 \tag{2.20}$$

$$\hat{\mathbf{T}}^N(R,\theta,\phi) = -\frac{1}{2\mu R^2}\left[\frac{1}{\sin\theta}\frac{\partial}{\partial\theta}(\sin\theta\frac{\partial}{\partial\theta}) + \frac{1}{\sin^2\theta}\frac{\partial^2}{\partial\phi^2} + \frac{\partial}{\partial R}(R^2\frac{\partial}{\partial R})\right] \tag{2.21}$$

$$\hat{\mathbf{V}}(r,R) = e^2\sum_{i=1}^{n}\left(\sum_{j=i+1}^{n}\frac{1}{r_{ij}} - \frac{Z_A}{r_{Ai}} - \frac{Z_B}{r_{Bi}}\right) + e^2\frac{Z_A Z_B}{R} \tag{2.22}$$

The wavefunction of the Hamiltonian in the molecule-fixed axis system is a function of (r, R, θ, ϕ). $\hat{\mathbf{T}}^N$ can then be approximately divided into vibrational and rotational terms:

$$\hat{\mathbf{T}}^N(R,\theta,\phi) = \hat{\mathbf{T}}^N(R) + \hat{\mathbf{H}}^{ROT}(R,\theta,\phi). \tag{2.23}$$

At this point, it is still impossible to rigorously solve the three terms in Equation (2.19) independently. However, based on the fact the nuclei are much heavier and move much more slowly than electrons, it is possible to treat the wavefunctions of nuclei and electrons separately. This assumption is the well-known Born-Oppenheimer (BO) approximation. As a result of adopting the BO approximation, the wavefunction

can be written as

$$\psi(r, R, \theta, \phi) = \phi(r; R)\chi(R, \theta, \phi). \tag{2.24}$$

The parametric dependence of the wavefunction $\phi(r; R)$ indicates ϕ is a function of r for a single internuclear distance R, because based on the BO approximation,

$$\frac{\partial}{\partial R}\phi(r; R) \approx 0 \quad \text{and} \quad \frac{\partial^2}{\partial R^2}\phi(r; R) \approx 0. \tag{2.25}$$

The electronic wavefunction and energy can be obtained by solving the clamped nuclei electronic Schrödinger equation:

$$[\hat{\mathbf{T}}^e(R) + \hat{\mathbf{V}}(r, R)]\phi(r; R) = E^{el}\phi(r; R) \tag{2.26}$$

or

$$\hat{\mathbf{H}}^{el}\phi(r; R) = E^{el}\phi(r; R). \tag{2.27}$$

The $E^{el}(R)$ derived as a function of R is the potential energy curve. Then the nuclear Schrödinger equation

$$[\hat{\mathbf{T}}^N R, \theta, \phi + E^{el}(R)]\chi(R, \theta, \phi) = E^T \chi(R, \theta, \phi) \tag{2.28}$$

can be solved to obtain the nuclear wavefunction and total energy E^T. Since the operator $\hat{\mathbf{T}}^N$ can be approximately separated into vibrational and rotational terms as in Equation (2.23), the total energy is the sum of electronic, rotational, and vibrational energies:

$$E^T = E^{el}(R) + E^{rot}(R) + E^{vib}(R). \tag{2.29}$$

In spectroscopy, the above equation is also written as Equation (2.1).

The BO approximation is one of the most fundamental approximations in quantum chemistry and widely used in many theoretical calculations. However, for cases in which the nuclei move faster than the electrons can respond nearly instantaneously, the BO approximation breaks down. Those situations are referred as non-adiabatic processes. The entire field of photochemistry is filled with non-adiabatic processes because avoided crossings (and conical intersections in polyatomic molecules) are heavily involved in interactions

among excited electronic states. However, even in those instances, the BO approximation is usually a good starting point for more refined models.

2.4. Electronic energy calculation in an adiabatic basis

The main challenge for the predissociation studies in this dissertation is that they involve both the ground electronic state and highly-excited states which are coupled to other bound or nonbound electronic states. For astrochemical purposes, predissociation is important for small molecules at photon energies from the UV up to their ionization thresholds or 13.6 eV, whichever is smaller. In this energy range, many molecular orbitals (MOs), valence and virtual, are energetically accessible, giving rise to a large number of electronic states, both valence and Rydberg, with various spin multiplicities and complicated couplings and perturbations among them. The predissociation process is mediated by interactions among these many states, requiring that they be calculated accurately.

In quantum chemistry, variational methods are used to find the wavefunction solutions of Equation (2.27), by optimizing parameters in a trial wavefunction to achieve the lowest possible energy. Then transition dipole moments and couplings can be calculated directly from the wavefunctions of different states. As the starting point of most variational methods, the Hartree-Fock (HF) method, or self-consistent field (SCF) method, calculates one single Slater determinant $|\phi_{HF}\rangle$, which is an antisymmetrized product of one-electron MOs (each represented by a linear combination of some basis functions), for each state as an approximate solution to the Schrödinger equation. Several post-HF methods use the HF solution as a reference. For instance, in configuration interaction (CI) methods, the electronic wavefunction for the state a, $|\Psi_a\rangle$, is expressed as a linear combination of electronic configurations or configuration state functions (CSFs):

$$|\Psi_a\rangle = \sum_\mu C_\mu |\phi_\mu\rangle \tag{2.30}$$

with the coefficients C_μ optimized by minimizing the electronic energy for the state a:

$$E_a = \min_C \frac{\langle \Psi_a | \hat{\mathbf{H}} | \Psi_a \rangle}{\langle \Psi_a | \Psi_a \rangle}. \tag{2.31}$$

If the actual wavefunction is dominated by a single configuration, usually the HF state, then it is possible to construct all other configurations as single $|S\rangle$, double $|D\rangle$, triple $|T\rangle$, quadruple $|Q\rangle$, $\cdots$ excitations of the

reference HF configuration. The wavefunction then can be written as

$$|\Psi_a\rangle = C_0|\phi_{HF}\rangle + C_i^a|S_i^a\rangle + C_{ij}^{ab}|D_{ij}^{ab}\rangle + C_{ijk}^{abc}|T_{ijk}^{abc}\rangle + \cdots . \tag{2.32}$$

If the excitations exhaust all possible configurations, the method is called Full CI (FCI). The calculation of FCI is very expensive since the number of configurations roughly increases as order $N!$ where N is the number of electrons of the molecule. It is reasonable to assume that the lower-order excitations contribute much more than higher-order ones. Often the above equation is truncated at single and double excitations, yielding the method called configuration interaction with single and double excitations (CISD or SDCI). Alternatively, the coupled cluster (CC) method uses an exponential excitation operator $\hat{T}$ to generate the ground electronic state:

$$|\Psi_0\rangle = e^{\hat{\mathbf{T}}}|\phi_0\rangle, \tag{2.33}$$

where the exponential operator is defined by Taylor expansion:

$$e^{\hat{\mathbf{T}}} = 1 + \hat{\mathbf{T}} + \frac{\hat{\mathbf{T}}^2}{2!} + \frac{\hat{\mathbf{T}}^3}{3!} = \sum_{K=0}^{\infty} \frac{\hat{\mathbf{T}}^K}{K!} \tag{2.34}$$

The cluster operator $\hat{\mathbf{T}}$ is sum of the operator of all single excitations $\hat{\mathbf{T}}_1$, all double excitations $\hat{\mathbf{T}}_2$, and so on:

$$\begin{aligned} \hat{\mathbf{T}} &= \hat{\mathbf{T}}_1 + \hat{\mathbf{T}}_2 + \hat{\mathbf{T}}_3 + \cdots , \\ \hat{\mathbf{T}}_1|\phi_0\rangle &= \sum_{i}^{\text{occ}} \sum_{a}^{\text{virt}} t_i^a |S_i^a\rangle; \\ \hat{\mathbf{T}}_2|\phi_0\rangle &= \sum_{i<j}^{\text{occ}} \sum_{a<b}^{\text{virt}} t_{ij}^{ab} |D_{ij}^{ab}\rangle; \cdots . \end{aligned} \tag{2.35}$$

The method CCSD(T), coupled cluster singles double and perturbative triple, is currently the most accurate yet computationally tractable *ab initio* electronic structure method for most small molecules. However, this method only works for the ground electronic state. Alternatively, the equation of motion coupled cluster (EOM-CC) method was developed to calculate excited states. To study photodissociation, a quantum chemistry method needs to be size-extensive and size-consistent, such that the energy of a diatomic molecule system AB correctly approaches the sum of atomic energies A and B as $R \to \infty$. The FCI method and

CC method to any order are both size-consistent and size-extensive, while truncated CI, such as CISD, is neither size-consistent nor size-extensive. The Davidson correction is a low-cost method to improve the size-consistency and size-extensivity of the CISD method (Langhoff & Davidson, 1974). The correlation energy contribution from quadruple excitations is estimated as:

$$\Delta E_Q = (1 - a_0^2)(E_{CISD} - E_{HF}), \tag{2.36}$$

where a_0 is the coefficient of the HF wavefunction in the CISD expansion, and E_{CISD} and E_{HF} are the energies of the CISD and HF calculations. The CISD energy with the Davidson correction (CISD+Q) can be calculated as

$$E_{CISD+Q} = E_{CISD} + \Delta E_Q. \tag{2.37}$$

Both CI and CC methods introduced above are single reference methods, and as such the state of interest must be well described by one configuration. This is often the case for ground states and low-lying excited states of small molecules. However, even for ground states of certain molecules, like C_2, and for highly excited states, the results from single reference methods can be qualitatively wrong.

To overcome the shortcomings of the single reference CI method, the multireference methods are required. Several multireference coupled cluster (MRCC) methods are in development, but they are not widely used. Instead, the standard method of choice for these problems is the multireference configuration interaction (MRCI) method. Instead of a single configuration, MRCI uses a reference space which contains a set of all configurations that may be important for the desired electronic states. Then the MRCI wavefunction is generated by including all the configurations in this reference space and all excitations from them. If the excitations are truncated by single and double excitations, then the method is called MRCISD or MRSDCI. It is possible to choose the reference space manually by picking several important configurations, which was done historically owing to limited computing capabilities. However, the multi-configurational self-consistent field (MCSCF) method is the preferred way to systematically generate the reference space and molecular orbitals for MRCISD calculations. In the MCSCF method, electronic states are also described as linear combinations of configurations like in a CI method, while the energy of a single state or the average energy of multiple states is minimized by optimizing both the molecular orbitals and the configuration interaction coefficients. If the average energy of multiple states is minimized, the method is called state-averaged

MCSCF (SA-MCSCF), which is useful in spectroscopy because both the ground and excited states are able to be calculated accurately at the same time. If the configurations considered in the MCSCF method are generated as a FCI in a set of orbitals, in other words, all possible configurations constructed from a number of electrons in a number of molecular orbitals, the method is called complete active space SCF (CASSCF). For example, the molecule CS has 8 valence molecular orbitals and 10 valence electrons. So a valence CASSCF calculation of CS includes all possible configurations involving 10 electrons distributed in these 8 molecular orbitals, which can be represented as (8,10) or ($8o$,$10e$). If some restrictions are applied to the active space, such as by only allowing configurations with a maximum number of holes in one orbital subspace, and a maximum number of electrons in another orbital subspace, with no limits in the remaining orbital space, the method is called restricted active space SCF (RASSCF). RASSCF generates a larger active space while reducing the number of configurations selected to keep the calculation affordable. Although there is no gold standard on how to choose the active space for MCSCF methods, it is necessary to include at least the dominant configurations of the states of interest for the calculation. While the MCSCF method alone can be used to calculate excited states by itself, it does not treat dynamic electron correlation, and is therefore often used to optimize molecular orbitals and generate reference states for the MRCI and multi-reference perturbation theories like complete active space perturbation theory (CASPT2), which is not discussed here. The follow-up methods account for the dynamic correlation. The Davidson correction can also be applied to MRCISD, leading to MRCISD+Q.

In these calculations, Dunning's correlation-consistent basis sets basis sets cc-pVXZ (X=D,T,Q,5,6) are often used (Dunning, 1989). To study the excited states and especially Rydberg states, the basis sets are often augmented with diffuse functions to describe higher n molecular orbitals, giving to the basis sets aug-cc-pVXZ (X=D,T,Q,5,6) (Kendall et al., 1992; Woon & Dunning, 1993, 1995).

In summary, multi-configurational methods must be used to treat the ground state and highly exited states simultaneously since both of them are important for predissociation of diatomic molecules. MCSCF followed by MRCISD+Q is the standard method to give the most accurate wavefunctions and energies for highly excited states. This method has been used to study structures of many diatomic molecules successfully.

Alternatively, potential energy curves can be obtained from experimental data. The Rydberg-Klein-Rees (RKR) procedure uses the $G(v)$ (Equation (2.6)) and $B(v)$ (Equation (2.3)) data of a diatomic molecule to derive the potential curve. The RKR procedure is based on the semiclassical Bohr-Sommerfeld quantization

condition

$$\int_a^b k(R)\,dR = (v + \frac{1}{2})\pi, \tag{2.38}$$

$$k(R) = \frac{p(R)}{\hbar} = \frac{\sqrt{2\mu}}{\hbar}\sqrt{E - V(R)}, \tag{2.39}$$

where $p(R)$ is the classical momentum corresponding to the kinetic energy $E - V(R)$. The two turning points a and b are the internuclear distances at which the total energy E is equal to potential energy $V(R)$, or in other words, $E - V(R) = 0$. The above equation makes it possible to determine the vibrational energy levels from the potential energy curve $V(R)$ or vice versa. Several programs have been developed independently in last half-century to study diatomic molecular structures. The RKR method has demonstrated great success in reproducing the energy curve of many diatomic molecules to a very good accuracy. This method works for excited states as well. One limitation of the RKR method is that it does not provide information about the electronic wavefunction $\phi(r; R)$. Also while frequency shifts and broadening of rotational lines indicate the existence of couplings and perturbations, the RKR method may not obtain potential energy curves of all states that may be involved in dynamic processes.

2.5. Terms neglected in the Born-Oppenheimer approximation and other perturbations

Ideally, the exact solution $|\psi_i^T\rangle$ of the Schrödinger equation (2.17) must satisfy the following two conditions:

$$(i) \quad \langle\psi_i^T|\hat{\mathbf{H}}|\psi_i^T\rangle = E_i^T, \tag{2.40}$$

$$(ii) \quad \langle\psi_i^T|\hat{\mathbf{H}}|\psi_j^T\rangle = 0.$$

In the BO approximation, the electronic Hamiltonian $\hat{\mathbf{H}}^{el}$ and nuclear kinetic energy operator $\hat{\mathbf{T}}^N$ are separated, finally giving the wavefunction solution in Equation 2.24. These wavefunctions under the BO approximation do not fulfill the second condition above, leaving some off-diagonal matrix elements. Some chemical systems are well described in the framework of BO approximation since either the off-diagonal matrix elements do not play an important role in these problems or they are small enough to be ignored. For other chemical systems, when more than one electronic state is involved in the dynamics, the off-diagonal matrix elements must be considered. Those terms can be treated as perturbations between different states.

The first type of perturbation is nonadiabatic coupling. Unfortunately, it is impossible to simultaneously diagonalize $\hat{\mathbf{H}}^{el}$ and $\hat{\mathbf{T}}^{N}$. Depending on the problem, a set of wavefunctions which is diagonal in one of them can be used as a 0th order basis set. Then, the other term can be introduced as a perturbation. In the MCSCF and MRCI methods, the obtained electronic state wavefunctions and the total wavefunctions are diagonal in $\hat{\mathbf{H}}^{el}$, but not $\hat{\mathbf{T}}^{N}$:

$$\langle \psi_1^{ad} | \hat{\mathbf{H}}^{el} | \psi_2^{ad} \rangle = 0, \tag{2.41}$$
$$\langle \psi_1^{ad} | \hat{\mathbf{T}}^{N} | \psi_2^{ad} \rangle \neq 0.$$

In this case, the electronic states are called adiabatic.

In the BO approximation, the total adiabatic wavefunction can be represented as:

$$|\psi^{ad}\rangle = |\phi^{el}\rangle |\chi^{v}\rangle. \tag{2.42}$$

It can be proved that the nuclear kinetic energy matrix element between $|\psi_i^{ad}\rangle$ and $|\psi_j^{ad}\rangle$ is

$$\begin{aligned} \langle \phi_i^{el} | \langle \chi_i^{v} | \hat{\mathbf{T}}^{N} | \phi_j^{el} \rangle | \chi_j^{v} \rangle = & -\frac{1}{\mu} \langle \chi_i^{v} \langle \phi_i^{el} | \frac{\partial}{\partial R} | \phi_j^{el} \rangle_r | \frac{d}{d\,R} \chi_j^{v} \rangle_R \\ & -\frac{1}{2\mu} \langle \chi_i^{v} \langle \phi_i^{el} | \frac{\partial^2}{\partial R^2} + \frac{2}{R} \frac{\partial}{\partial R} | \phi_j^{el} \rangle_r | \chi_j^{v} \rangle_R. \end{aligned} \tag{2.43}$$

The first term is called the non-adiabatic coupling term (NACT) and the matrix element within it,

$$\tau = \langle \psi_i^{ad} | \bigtriangledown | \psi_j^{ad} \rangle = \langle \psi_i^{ad} | \frac{\partial}{\partial R} | \psi_j^{ad} \rangle, \tag{2.44}$$

is defined as the non-adiabatic coupling matrix element (NACME). The second term involving the second derivative is usually much smaller compared to the first term and can be ignored in most cases. The NACME can therefore be calculated directly from the adiabatic electronic wavefunctions from MCSCF and MRCI calculations.

Alternatively, a diabatic (or nonadiabatic) basis can be chosen to be near-diagonal in nuclear kinetic energy:

$$\langle \psi_1^{d} | \hat{\mathbf{H}}^{el} | \psi_2^{d} \rangle = H_{12}^{e}(R) \neq 0, \tag{2.45}$$
$$\langle \psi_1^{d} | \hat{\mathbf{T}}^{N} | \psi_2^{d} \rangle = 0 \text{ or } \approx 0.$$

The perturbation between the diabatic states can be considered an electrostatic interaction. In principle, the two models should give same results, such as energy levels of states, after the appropriate perturbation is dealt with correctly.

When two electronic states with the same symmetry and angular momentum approach to equal energy at the same internuclear distance, the BO approximation fails. In the adiabatic model, because the electronic Hamiltonian is precisely diagonalized, the two calculated potential energy curves split and take on a hyperbolic shape with an energy difference of $2H^e_{12}(R)$ at the point R_c where the two curves would otherwise cross. This is called an avoided crossing. Around the avoided crossing, the two states exchange wavefunctions and the NACME becomes large with a maximum value at R_c. In the diabatic model, the two curves cross. The electrostatic coupling between the two diabatic states is normally smooth and small near the crossing. The region around R_c in the adiabatic and diabatic basis sets is shown in Fig 2.2. A similar phenomenon, called a conical intersection, occurs within the $3N-6$-dimensional hypersurfaces of polyatomic molecules.

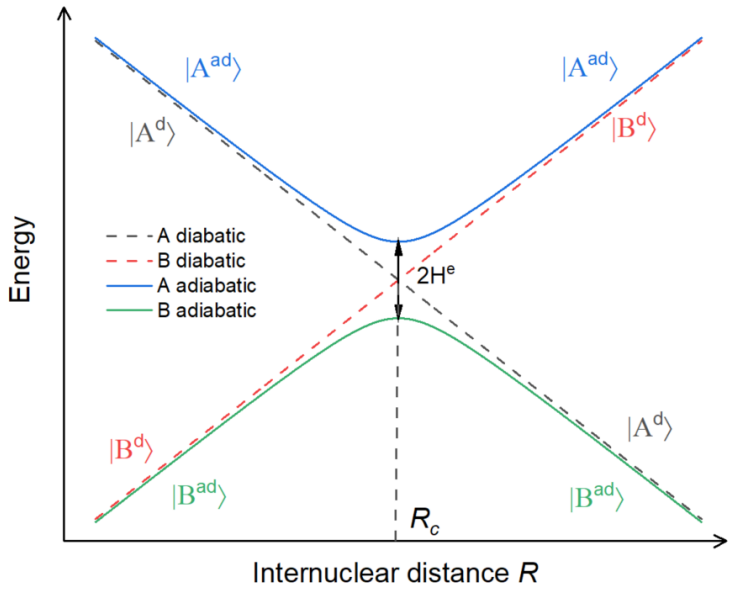

FIGURE 2.2. Diabatic and adiabatic potential energy curves around an avoided crossing

Although the two models are equivalent to each other of fully treating the perturbations, the diabatic model is more straightforward to use in dynamic processes because the coupling between diabatic states is smooth and small while the coupling between adiabatic states is abrupt and large. However, the diabatic states cannot be obtained directly from quantum electronic structure calculations. Mathematically, it is

possible to obtain diabatic states from adiabatic states of a diatomic molecule using the curl condition. For a two-state system with adiabatic potential curves $V_1^{ad}(R)$ and $V_2^{ad}(R)$ and the NACME between them $\tau(R)$ as a function of internuclear distance R, the mixing angle $\gamma(R)$ can be calculated as the integral of the NACME from distance R to infinite internuclear distance:

$$\gamma(R) = \int_R^\infty \tau(s)\, ds. \tag{2.46}$$

Equation (2.46 assumes that there is no coupling between the two states when the two atoms are fully separated, which is valid normally. Then the adiabatic-to-diabatic transformation (ADT) matrix $A(R)$ can be written as:

$$A(R) = \begin{pmatrix} \cos\gamma(R) & \sin\gamma(R) \\ -\sin\gamma(R) & \cos\gamma(R). \end{pmatrix} \tag{2.47}$$

Applying the matrix $A(R)$ as a unitary transformation of the adiabatic states gives diabatic potential curves

$$V_1^d(R) = V_1^{ad}(R)\cos^2\gamma(R) + V_2^{ad}(R)\sin^2\gamma(R), \tag{2.48}$$

$$V_2^d(R) = V_1^{ad}(R)\sin^2\gamma(R) + V_2^{ad}(R)\cos^2\gamma(R), \tag{2.49}$$

with the coupling term between them

$$V_{12}^d(R) = (V_2^{ad}(R) - V_1^{ad}(R))\sin\gamma(R)\cos\gamma(R) \tag{2.50}$$

As a simple example, Schmidt et al. (2015) used this method to successfully build a diabatic model of the $X\,^1\Sigma^+$ and $2\,^1\Sigma^+$ states of LiI. Detailed mathematical examples of ADT for more complicated systems, such as polyatomic molecules and multistate systems, are discussed in Baer (2006). Often, in these more complicated cases, an exact diabatization is either impossible or impractical. For example, for polyatomic molecules, it is not possible to simultaneously eliminate all derivative couplings in nuclear configuration space. For the highly excited states of diatomic molecules, the diabatic couplings among those excited states are much more complicated than the above two-state system because there are many avoided crossings in that energy range. In those cases where ADT matrix is not straightforward, several quasi-diabatization methods have been used in previous studies. It is possible to diabatize the adiabatic states by assuming certain properties, such as electric dipole moment and/or transition dipole moments, vary smoothly with the

internuclear distance and are diagonal in the diabatic representation. For example, Werner & Meyer (1981) obtained a diabatic description of the two lowest $^1\Sigma^+$ states of LiF corresponding to the energy transfer process $\mathrm{Li} + \mathrm{F} \longrightarrow \mathrm{Li}^+ + \mathrm{F}^-$ by diabatizing the dipole moments of these two ionic and neutral states.

Equation (2.19) does not include terms related to electron spin angular momentum. There are several other perturbations related to electronic spin, including the spin-orbit interaction $\hat{\mathbf{H}}^{SO}$, spin-rotation interaction $\hat{\mathbf{H}}^{SR}$, and spin-spin interaction $\hat{\mathbf{H}}^{SS}$, which also add to the diagonal and off-diagonal elements of the Hamiltonian matrix. The spin-orbit interaction is important in the predissociation of many diatomic molecules and can be expressed in SI units as the fundamental Pauli-Breit operator

$$\hat{\mathbf{H}}^{SO} = \frac{\alpha^2}{2} \sum_i \left\{ \frac{Z_A}{r_{iA}^3} \hat{\mathbf{l}}_{iA} \cdot \hat{\mathbf{s}}_i + \frac{Z_B}{r_{iB}^3} \hat{\mathbf{l}}_{iB} \cdot \hat{\mathbf{s}}_i \right\} - \frac{\alpha^2}{2} \sum_{i \neq j} \frac{1}{r_{ij}^3} (\hat{\mathbf{r}}_{ij} \times \hat{\mathbf{p}}_i)(\hat{\mathbf{s}}_i + 2\hat{\mathbf{s}}_j), \tag{2.51}$$

where α is the fine-structure $\alpha = e^2/\hbar c = 1/137.036$, $\hat{\mathbf{l}}_{iA}$ and $\hat{\mathbf{l}}_{iB}$ are the angular-momentum operators of the i-th electron relative to nuclei A and B:

$$\hat{\mathbf{l}}_{iA} = \frac{1}{\hbar}(\hat{\mathbf{r}}_{iA} \times \hat{\mathbf{p}}_i), \quad \hat{\mathbf{l}}_B = \frac{1}{\hbar}(\hat{\mathbf{r}}_{iB} \times \hat{\mathbf{p}}_i), \tag{2.52}$$

and $\hat{\mathbf{r}}_{ij}$ is the relative position vector of electrons i and j. The first part in Equation (2.51) corresponds to the spin-orbit coupling of each electron in the field of two nuclei with charges Z_A and Z_B, and the second part is the interaction of one electron with the orbital motion of another electron.

Veseth (1970) simplified the Equation (2.51) to obtain

$$\hat{\mathbf{H}}^{SO} = \sum_{i,j} \xi(i,j) \hat{\mathbf{l}}_i \cdot \hat{\mathbf{s}}_j, \tag{2.53}$$

where the symbol $\xi(i,j)$ is used so that the result is independent of the choice of the origin for the angular momenta, and includes the r-dependent terms. The definition of $\xi(i,j)$ is not important for this section and can be referred to (Veseth, 1970). The $\hat{\mathbf{l}}_i \cdot \hat{\mathbf{s}}_j$ can be expanded to

$$\hat{\mathbf{l}}_i \cdot \hat{\mathbf{s}}_j = \hat{\mathbf{l}}_{iz} \cdot \hat{\mathbf{s}}_{jz} + \frac{1}{2}(\hat{\mathbf{l}}_i^+ \mathbf{s}_j^+ + \hat{\mathbf{l}}_i^- \hat{\mathbf{s}}_j^-). \tag{2.54}$$

The first term is diagonal in the $|vS\Omega\Lambda\Sigma\rangle$ basis and lifted the Σ and therefore Ω degeneracy:

$$\langle vS\Omega\Lambda\Sigma|\hat{\mathbf{H}}^{SO}|vS\Omega\Lambda\Sigma\rangle = A\Lambda\Sigma, \tag{2.55}$$

where A is the spin-orbit splitting parameter. The second term is off-diagonal and introduces perturbations between states with different electronic configurations and Λ. These type of spin-orbit interaction may play an important role in predissociation. The selection rules for spin-orbit coupling are summarized as

$$\Delta J = \Delta\Omega = 0; \quad \Delta S = 0, \pm 1; \quad \Sigma^+ \leftrightarrow \Sigma^-; \quad g \nleftrightarrow u; \tag{2.56}$$

$$\Delta\Lambda = \Delta\Sigma = 0 \text{ or } \Delta\Lambda = -\Delta\Sigma = \pm 1$$

Other perturbations related to angular momentum operators, such as L-uncoupling, are important for calculating the energy levels but are less important for predissociation compared with diabatic coupling and spin-orbit coupling, and hence are not discussed here.

2.6. Photodissociation and predissociation

When a diatomic molecule absorbs a photon, it is promoted into an excited state. In general, the intensity of a bound-bound transition depends on the transition dipole moment between the two electronic states, the Franck-Condon factors between the vibrational states, and the Hönl-London factors of the rotational angular momenta. For homonuclear diatomic molecules, the nuclear spin also affects the degeneracy ratio of the intensity distribution. Historically, different physical parameters have been used to describe the transition intensities, including Einstein coefficients A_{21} and B_{12}, cross sections σ_0, and oscillator strength f values. The relationships among these terms is reviewed in Hilborn (1982).

When the energy of the excited state is above the dissociation threshold D_e, it may lead to photodissociation as shown in Figure 2.3. If the excited state is nonbound, the transition ends in a continuum of unbound vibrational states, leading to direct photodissociation. The absorption cross section in SI units from an initial bound state $|\psi_{v''J''}\rangle$ to a final continuum state $|\psi_{EJ'}\rangle$ (normalized by $1/\sqrt{E}$ to account for the density of states) is

$$\sigma_{v''J''}(E) = \frac{\pi\tilde{\nu}}{3\hbar\varepsilon_0} \sum_{J'} \frac{S_{J'J''\Omega'\Omega''}}{2J''+1} |\langle\psi_{EJ'}(R)|R_e(R)|\psi_{v''J''}(R)\rangle|^2, \tag{2.57}$$

where ε_0 is the vacuum permittivity, $\tilde{\nu}$ is the photon wavenumber, $S_{J'J''\Omega'\Omega''}$ is the Hönl-London factor, and $R_e(R)$ is the electric transition dipole moment between the two states. Direct photodissociation is much faster than spontaneous emission, thus all of the absorptions give rise to photodissociation. The photoabsorption

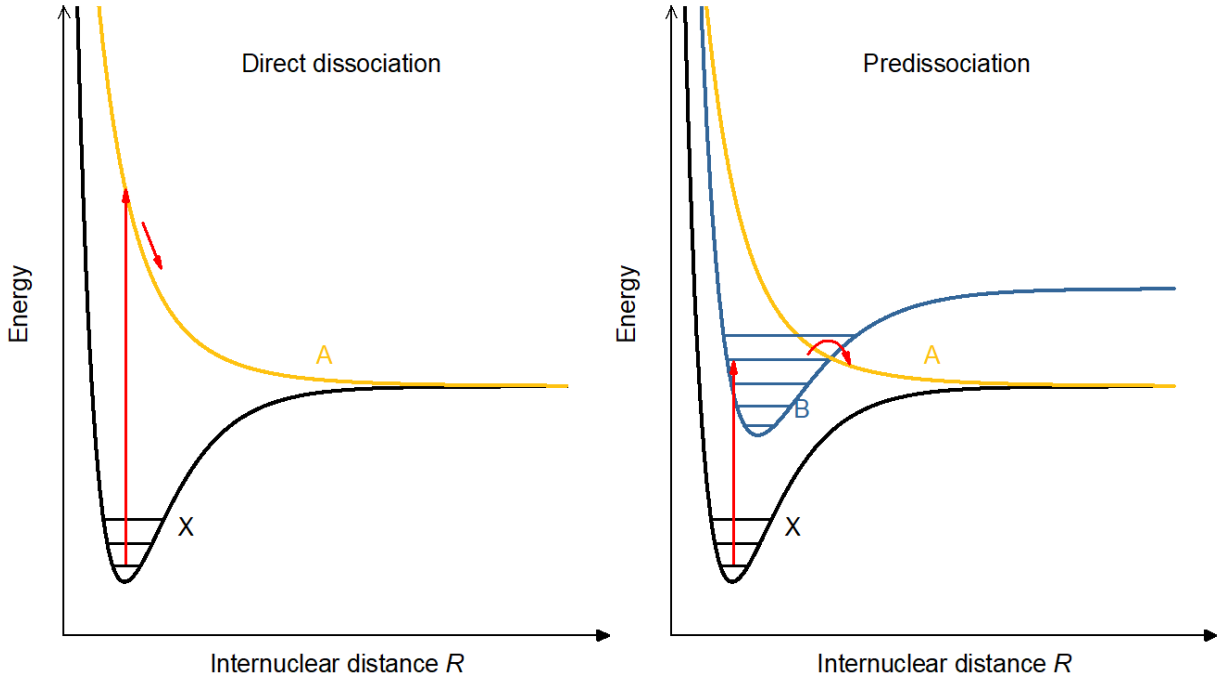

FIGURE 2.3. Schematic of direct dissociation and predissociation.

and photodissociation cross section arising from the direct process has a peak close to the vertical excitation energy according to Franck-Condon principle, and decreases slowly with wavelength gradually.

If the excited state is bound, then it may couple into a nonbound state, leading to a nonradiative dissociation process called predissociation. The photoabsorption cross sections of predissociative transitions can be resolved into lines corresponding to rovibronic structures of excited bound states. The rate of a single step of predissociation from an initial bound state $|i\rangle$ to a continuum state $|f\rangle$ (again normalized by $1/\sqrt{E}$) can be calculated by Fermi's golden rule,

$$k_{i\to f} = \frac{2\pi}{\hbar}|\langle f|\hat{\mathbf{H}}'|i\rangle|^2, \tag{2.58}$$

where $k_{i\to f}$ is the transition probability per unit of time from $|i\rangle$ to $|f\rangle$, $\hat{\mathbf{H}}'$ is the operator coupling $|i\rangle$ and $|f\rangle$. Predissociation competes with spontaneous emission to different lower bound states. The total lifetime τ of an excited bound state is

$$\frac{1}{\tau} = \frac{1}{\tau_d} + \sum_i^n \frac{1}{\tau_i}, \tag{2.59}$$

where τ_d is the lifetime of predissociation, and τ_i is the lifetime of emission to the i-th lower state. The linewidth γ of the transition is linked to the total lifetime as

$$\tau = \frac{\hbar}{\gamma} = \frac{5.3 \times 10^{-12}}{\gamma}, \tag{2.60}$$

if τ is in s and γ is in cm^{-1}. The dissociation efficiency η can be defined as the fraction of molecules in excited state that decay via predissociation

$$\eta = \frac{\tau}{\tau_d}. \tag{2.61}$$

In 2020, Xue et al. (2020) used this Fermi's Golden Rule approach as implemented in the program BCONT (Le Roy, 1989) to successfully model linewidths of the SOC-induced predissociative transitions in the $B\,^3\Sigma_u^-$ state of S_2. For many diatomic molecules, the predissociation lifetime is of the order of picoseconds to nanoseconds, while the emission lifetime is normally of the order of nanoseconds to tens of nanoseconds. Thus, the dissociation efficiency can be assumed as unity in many cases. For many diatomic molecules in the VUV range, the couplings are complicated, potentially involving several states that dissociate to different atomic limits, and therefore predissociation may give rise to multiple different pairs of atomic product states.

To study a complicated predissociation system, knowledge of accessible excited states and the states coupled to them are needed. Predissociation itself is a dynamic problem, and time-dependent wavepacket propagation methods are therefore expected to give a good description of it. A detailed review about time-dependent methods can be found in Schinke (1995). From the autocorrelation function obtained by solving the time-dependent Schödinger equation, the absorption cross sections can be calculated.

Alternatively, time-independent methods are able to give the same results. The linewidth calculated in time-independent methods reflects the dynamic nature of predissociation. The Coupled Schrödinger equation (CSE) method treats the interaction between the radial wavefunctions of coupled electronic states (Mies, 1980). Using the Born-Oppenheimer wavefunctions as basis states, the new coupled wavefunctions can be represented as a linear combination of N_T diabatic or adiabatic electronic and nuclear wavefunctions:

$$\psi_i(r, R, \theta, \phi) = \sum_{j=1}^{N_T} \frac{1}{R} \chi_{ij}(R) \phi_j(r; R) \Theta_j(\theta, \phi). \tag{2.62}$$

In this representation, the $\chi_{ij}(R)$ are R-dependent expansion coefficients of the electronic-rotational basis states $\phi(r;R)\Theta(\theta,\phi)$, which are called coupled channels. The goal is to solve for the coefficients $\chi_{ij}(R)$, which describe the contribution of each electronic-rotational state (which may be bound or unbound) at a given energy.

The coupled Schrödinger equations are in the form

$$-\frac{\hbar^2}{2\mu}\frac{d^2}{dR^2}\chi_{ik}(R)+\sum_{j=1}^{N_T}\chi_{ij}(R)V_{jk}(R)=E\chi_{ik}(R). \tag{2.63}$$

where the interaction matrix $V(R)$ is given by elements

$$V_{jk}(R)=V_{kj}(R)=\begin{cases}E_j^{el}(R)+\frac{\hbar^2R_k(R_k+1)}{2\mu R^2} & j=k\\ \langle\phi_j(r;R)\Theta_j(\theta,\phi)|\hat{\mathbf{H}}^{el}+\hat{\mathbf{H}}^{ROT}|\phi_k(r;R)\Theta_k(\theta,\phi)\rangle & j\neq k,\end{cases} \tag{2.64}$$

where R_k is the rotational quantum number of channel k. The diagonal elements correspond to the electronic potential energy with rotational energy, while the off-diagonal elements are the electrostatic perturbations and/or spin-orbit couplings between diabatic states. The Equation 2.63 can be rewritten in matrix form as

$$\frac{d^2}{dR^2}\boldsymbol{\chi}(R)=-\frac{2\mu}{\hbar^2}\boldsymbol{\chi}(R)[E\mathbf{I}-\mathbf{V}(R)]. \tag{2.65}$$

This set of coupled equation can be solved using the renormalized Numerov method (Johnson, 1978; Torop et al., 1987). The set of expansion coefficients $\chi_{ij}(R)$ are thereby obtained to build the coupled numerical wavefunctions. When at least one channel is open (i.e. the energy is above the lowest dissociation limit), the total absorption cross section from the lower state j can be calculated by summing over all N_O open channels

$$\sigma_j(v)=\sum_{i=1}^{N_O}\sigma_{ij}(v), \tag{2.66}$$

where

$$\sigma_{ij}(v)=\frac{\pi\tilde{\nu}}{3\hbar\epsilon_0}\left|\sum_k^{N_T}\left(\int\chi_{ik}^{\dagger}(R)R_{kj}^e(R)\chi_j(R)\,dR\cdot S^{1/2}_{J_kJ_j\Omega_k\Omega_j}\right)\right|^2. \tag{2.67}$$

R_{kj}^e is the electric transition dipole moments between the lower state j and the upper state i, $\tilde{\nu}$ is the photon wavenumber, and $S_{J_kJ_j\Omega_k\Omega_j}$ is the corresponding Hönl-London factor. If the dissociation efficiency η is assumed to be 1, then the obtained photoabsorption cross section is the photodissociation cross section. The

photodissociation cross sections calculated with CSE methods for different open channels can be used to calculate the atomic limit branching ratios.

When an interaction between two dissociative states occurs along a channel, the semiclassical Landau-Zener model can alternatively be used to provide a simpler interpretation of the branching ratio interns of a transition probability between the states (Zener, 1932). For a two state system with the Hamiltonian

$$H = \begin{pmatrix} E_1 & H_{12} \\ H_{12} & E_2 \end{pmatrix}, \tag{2.68}$$

the semi-classical transition probability from the first diabatic state with energy E_1 to the second diabatic state with energy E_2 can be calculated as

$$P = e^{-2\pi\Gamma}, \tag{2.69}$$

where

$$\Gamma = \frac{1}{\hbar} \frac{H_{12}^2}{|\frac{d}{dt}(E_1 - E_2)|} = \frac{1}{\hbar} \frac{H_{12}^2}{v|F_1 - F_2|}. \tag{2.70}$$

Here, H_{12} is the diabatic electronic coupling strength, which is assumed to be constant over the crossing region, v is the relative velocity of the particle at the crossing point, and F_1 and F_2 are the slopes of the two diabatic potentials through the crossing region. The Landau-Zener model requires that both F_1 and F_2 are negative, which happens in some predissociation channels with couplings after the initial predissociation. In 1990, Friedman et al. (1990) successfully described the branching ratios arising from predissociation of low-lying vibrational levels of the $C\,^3\Pi_g$ Rydberg state of O_2 using a Landau-Zener model.

In summary, the CSE method is capable of treating a complicated coupling system with multiple upper states. This dissertation applies the CSE method to calculate photodissociation cross sections for diatomic molecules using the Python package Pydiatomic (Gibson, 2016).

CHAPTER 3

Ab initio Study of Ground-State CS Photodissociation Via Highly Excited Electronic States

This chapter is based on the peer-reviewed journal article: Zhongxing Xu, Nan Luo, S. R. Federman, William M. Jackson, Cheuk-Yiu Ng, Lee-Ping Wang, and Kyle N. Crabtree, "Ab Initio Study of Ground-state CS Photodissociation via Highly Excited Electronic States", The Astrophysical Journal, 882, 86, (2019).

Abstract

Photodissociation by ultraviolet radiation is the key destruction pathway for CS in photon-dominated regions, such as diffuse clouds. However, the large uncertainties of photodissociation cross sections and rates of CS, resulting from a lack of both laboratory experiments and theoretical calculations, limit the accuracy of calculated abundances of S-bearing molecules by modern astrochemical models. Here we show a detailed *ab initio* study of CS photodissociation. Accurate potential energy curves of CS electronic states were obtained by choosing an active space CAS(8,10) in MRCI+Q/aug-cc-pV(5+d)Z calculation with additional diffuse functions, with a focus on the B and $C\,^1\Sigma^+$ states. Cross sections for both direct photodissociation and predissociation from the vibronic ground state were calculated by applying the coupled-channel method. We found that the $C - X$ $(0 - 0)$ transition has extremely strong absorption due to a large transition dipole moment in the Franck-Condon region and the upper state is resonant with several triplet states via spin-orbit couplings, resulting in predissociation to the main atomic products C (^3P) and S (^1D). Our new calculations show the photodissociation rate under the standard interstellar radiation field is 2.9×10^{-9} s^{-1}, with a 57% contribution from $C - X$ $(0 - 0)$ transition. This value is larger than that adopted by the Leiden photodissociation and photoionization database by a factor of 3.0. Our accurate *ab initio* calculations will allow more secure determination of S-bearing molecules in astrochemical models.

3.1. Introduction

Sulfur is an abundant element in space, e.g., the relative abundance of S to H is $1.3{\times}10^{-5}$ in the solar system (Asplund et al., 2009), and the abundances of S-bearing molecules are sensitive to the physical conditions of their environments. In the interstellar medium (ISM), S-bearing molecules are commonly

detected and used as tracers of physical properties (Semenov et al., 2018). In star forming regions, it has been suggested that abundances of H_2S, SO and SO_2 could act as a chemical clock on the time scale of 10^4 years due to both thermal heating and shock interactions (van der Tak et al., 2003; Wakelam et al., 2011). In protoplanetary disks, the abundances of S-bearing species may correlate with the C/O ratio, surface diffusivity, turbulent mixing, X-ray luminosity, ultraviolet (UV) intensity and grain growth (Semenov et al., 2018).

However, the abundances of S-bearing species are poorly reproduced by modern astrochemical models (Lucas & Liszt, 2002), possibly because of the large uncertainties in kinetic data, missing reaction pathways, and unaccounted reservoirs of sulfur (Druard & Wakelam, 2012; Loison et al., 2012; Vidal et al., 2017). CS was the first sulfur-bearing molecule observed in interstellar space, initially detected by its 3–2 rotational emission line at 146.969 GHz in several dense sources (Penzias et al., 1971). It has since been found in a wide set of diffuse and dense interstellar clouds (Drdla et al., 1989; Heithausen et al., 1998; McQuinn et al., 2002; Scappini et al., 2007; Zuckerman et al., 1972), as well as comets (Canaves et al., 2007; Jackson et al., 1982). Additionally, CS is the key species in the sulfur chemistry of protoplanetary disks. Observations of the CS column density are used to determine upper limits for other S-bearing molecules since CS is the only detected sulfur species in many disks, such as DM Tau (Semenov et al., 2018).

In photon-dominated or photodissociation regions (PDRs), UV photons play a critical role in the gas phase chemistry and act as the most important source of energy. In a general sense, PDRs include peripheries of molecular clouds, diffuse clouds, translucent clouds, the surfaces of protoplanetary disks, and cometary and exoplanetary atmospheres. For small molecules like CS, photodissociation is the key destruction pathway in those environments. Accurate chemical modeling requires the wavelength-dependent photoabsorption/photodissociation cross sections at energies above the dissociation limit.

While the ground $X\,^1\Sigma^+$ and several low-lying electronic states ($a\,^3\Pi$, $a'\,^3\Sigma^+$, $d\,^3\Delta$, $e\,^3\Sigma^-$, $A\,^1\Pi$ and $A'\,^1\Sigma^+$) of CS have been extensively studied by both experiments and *ab initio* calculations (Shi et al., 2013), very few studies have been done on highly excited states in vacuum UV (VUV) region where CS may undergo photodissociation. The pioneering study on highly excited states of CS was by Crawford & Shurcliff (1934), who assigned a strong band system around 251 nm to CS in the emission spectrum of a low-pressure discharge of CS_2. Later Donovan et al. (1970) recorded the first VUV spectrum of CS via time-resolved flash photolysis of CS_2 coupled with a high-resolution spectrograph. A strong band observed at 154.1 nm

was assigned as $B\,^1\Sigma^+ - X\,^1\Sigma^+$ by analogy with the valence isoelectronic species CO, which suggests the B state of CS has a Rydberg nature like the corresponding state of CO. Two more strong bands at 140.2 and 139.9 nm were assigned as the $C\,^1\Sigma^+ - X\,^1\Sigma^+$ $(0-0)$ and $(1-1)$ transitions, also by analogy with CO.

A subsequent high-resolution VUV absorption study of CS by Stark et al. (1987) confirmed the $C - X$ band assignment and also found additional vibrational components of the $B - X$ transition. Their rotational contour analysis of the $B - X$ $(1-0)$ band found that the spectroscopic constants of B state are close to those of the CS^+ ground state, strongly supporting the proposed Rydberg nature of the B state. A rough measurement showed that the linewidth of the $(1-0)$ band is on the order of $1\,cm^{-1}$, which is clearly broadened by predissociation. All other bands were too diffuse to show rotational structures. Both the $C - X$ $(0-0)$ and $(1-1)$ bands were diffuse and intense, indicating the Franck-Condon factors of this transition must notably favor the $(0-0)$ transition. The experimental assignments were supported by an early SCF-CI calculation (Bruna et al., 1975), which found that the B and C Rydberg states agreed with experimental energies within 0.1 eV. The spectroscopic evidence suggests that the $B - X$ and $C - X$ bands should play important roles in CS photodissociation in space owing to their strong intensities and their broadening by predissociation. However, at present the best estimates of the CS photodissociation cross sections in the Leiden database (Heays et al., 2017) were made by combining the measured $B - X$ transition wavelength and vertical excitation energies of higher valence and Rydberg states, and are estimated to be uncertain to a factor of 10.

To improve the accuracy of photodissociation data for astronomical models, further experiments and high-level quantum chemical calculations are needed. Most recently, Pattillo et al. (2018) performed the first high-level *ab initio* calculations targeting states involved in CS photodissociation. They concluded that the dominant contribution to CS photodissociation from the ground electronic state comes from direct excitation of several dissociative states, including $A'\,^1\Sigma^+$ and several $^1\Pi$ states, while predissociation via the B state is unimportant. However, their results show significant discrepancies with the experimental VUV spectroscopy of the $^1\Sigma^+$ states: specifically, the energy of the B state is about $7000\,cm^{-1}$ higher than the experimental value and the shape of its potential energy curve indicates a much lower vibrational constant compared with experiments, and the C state is missing entirely. Thus, the conclusion that predissociation in highly excited states is unimportant should be re-examined more carefully.

Here, we present a high-level *ab initio* study of CS photodissociation, including for the first time a detailed investigation of its predissociation via the $B\,^1\Sigma^+$ and $C\,^1\Sigma^+$ states. We found that under the Draine radiation field (Draine, 1978), inclusion of the $C - X$ and $B - X$ transitions increases the CS photodissociation rate by nearly an order of magnitude compared with the results of Pattillo et al. (2018), and yields an overall rate that is higher by a factor of 3 compared with the Leiden database (Heays et al., 2017). The details of our theoretical methods are introduced in Section 3.2. The computed potential energy curves, transition dipole moments, photodissociation cross sections, and photodissociation rates are discussed in Section 3.3, as well as the comparison between our calculations and experiments. Finally, a summary of the work and its future directions are given in Section 3.4.

3.2. Theory and calculations

3.2.1. Ab initio calculation.

Our calculations use the state-averaged complete active space self-consistent field (SA-CASSCF) approach (Knowles & Werner, 1985; Werner & Knowles, 1985), followed by internally contracted multireference configuration interaction with single and double excitations and the Davidson correction (MRCI+Q) (Knowles & Werner, 1988, 1992; Werner & Knowles, 1988), a widely used method for calculating excited electronic states, especially for diatomic molecules. We used the the quantum chemical package MOLPRO 2015.1 (H.-J. Werner & P. J. Knowles, 2015; Werner et al., 2012) to calculate the adiabatic potential energy curves (PECs) and transition dipole moments (TDMs) of CS.

To determine the PECs accurately, up to a total of 105 single point calculations with internuclear separation between 0.78 to 7.93 Å were carried out, with step sizes ranging from 0.0026 to 0.26 Å. The smaller step sizes were used near the equilibrium geometry of the ground state and in the vicinity of several important avoided crossings between states with the same symmetry to ensure good accuracy of calculated properties. We used Dunning's augmented correlation consistent polarized valence quintuple-zeta Gaussian basis set with tight *d* orbitals for sulfur [aug-cc-pV(5+d)Z or AV(5+d)z](Dunning et al., 2001; Kendall et al., 1992). The tight *d* orbitals have been shown to be essential for calculating accurate properties of S-bearing species (Trabelsi et al., 2018). Several additional diffuse Gaussian functions corresponding to Rydberg atomic orbitals (AOs) of C and S were added to the basis sets to more accurately represent the Rydberg character of the *B* and *C* states. Their exponents, derived from Schaefer (1977), are given in Table 3.1.

TABLE 3.1. Exponents of diffuse Gaussian functions added to the aug-cc-pV(5+d)Z basis set

C					S		
3*s*	3*p*	3*d*	4*s*	4*p*	3*d*	4*s*	4*p*
0.01725	0.01575	0.02850	0.01045	0.00931	0.02850	0.01725	0.02949
		0.01125	0.00413	0.00368	0.01125		0.01500

MOLPRO is unable to take advantage of the full symmetry of non-Abelian groups (in this case, $C_{\infty v}$), so the calculation is performed in the largest Abelian subgroup (C_{2v}). The reducing map of irreducible representations from $C_{\infty v}$ to C_{2v} is $\Sigma^+ \rightarrow A_1$, $\Sigma^- \rightarrow A_2$ $\Pi \rightarrow (B_1, B_2)$, and $\Delta \rightarrow (A_1, A_2)$. We adopt MOLPRO's order of irreducible representations for C_{2v} to indicate the number of molecular orbitals (MOs) of each symmetry in the following discussion, (a_1, b_1, b_2, a_2).

The dominant electron configuration of CS in its ground ($X\,^1\Sigma^+$) state at its equilibrium geometry is $1\sigma^2 2\sigma^2 3\sigma^2 4\sigma^2 5\sigma^2 6\sigma^2 7\sigma^2 1\pi^4 2\pi^4$. To construct the active space for our SA-CASSCF/MRCI+Q calculation, 17 MOs (11,3,3,0) were involved in total. The 7 MOs (5,1,1,0) with lowest energies are kept closed (doubly-occupied) in the reference space, while the remaining 8 electrons are distributed in the other 10 MOs, forming an active space CAS(8,10) (6,2,2,0). A more detailed discussion on our choice of active space is given in Section 3.3.1.1. The MOs included in our calculation described above are shown near the equilibrium geometry of the ground state in Figure 3.1.

The ground states of atomic carbon and sulfur are both ^3P, followed by an excited state ^1D. The lowest four dissociation limits of CS therefore correlate to C ($^3P_{0,1,2}$) + S ($^3P_{0,1,2}$), C ($^3P_{0,1,2}$) + S (^1D), C (^1D) + S ($^3P_{0,1,2}$), and C (^1D) + S (^1D). These combinations give rise to 82 electronic states in C_{2v} symmetry, which are 10 $^1A_1$, 8 $^1B_1$, 8 $^1B_2$, 8 $^1A_2$, 9 $^3A_1$, 10 $^3B_1$, 10 $^3B_2$, 10 $^3A_2$, 3 $^5A_1$, 2 $^5B_1$, 2 $^5B_2$, and 2 $^5A_2$ states. We carried out the averaging process among the 82 lowest-energy states of these C_{2v} symmetries in the SA-CASSCF calculations regardless of which symmetries they correspond to in $C_{\infty v}$; this changes with internuclear distance.

The orbitals optimized by SA-CASSCF are used in the MRCI+Q calculations. The CI treatment was carried out by employing a reference space of 2053 ($^1A_1$), 1843 ($^3A_1$) 1672 ($^1B_1$ and $^3B_1$), 1368 ($^1A_2$ and $^3A_2$), 891 ($^5A_1$), 1000 ($^5B_1$), and 1144 ($^5A_2$) configurations, from which all single and double excitations were generated. As a demonstration of the calculation size, the total number of uncontracted configurations was 502 853 808 while the total number of contracted configurations was 17 569 850 in $^1A_1$ symmetry for

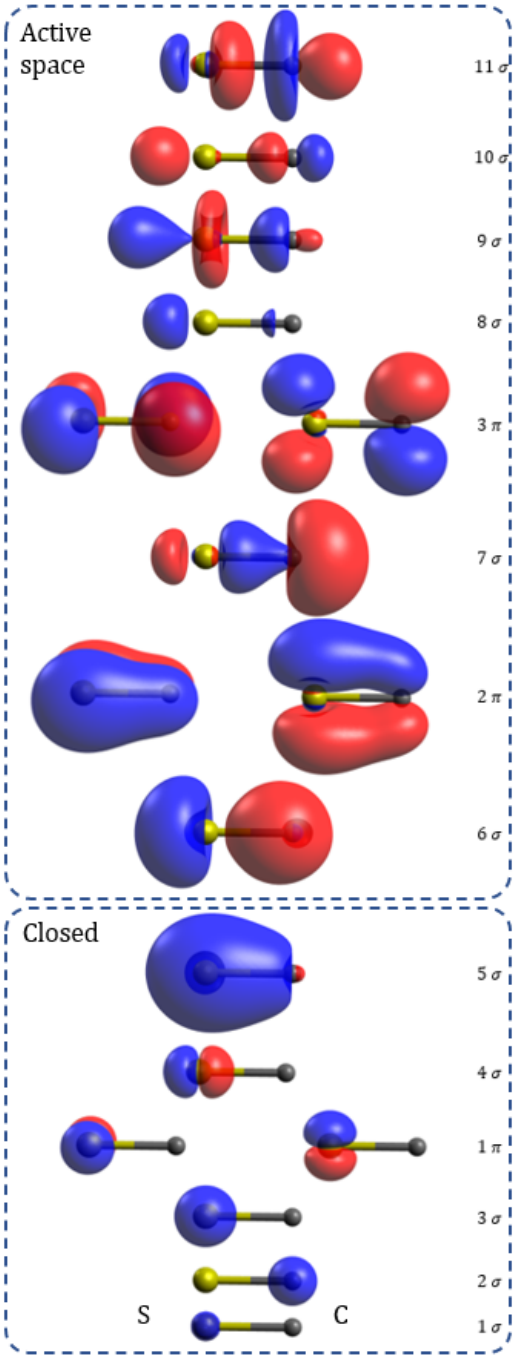

FIGURE 3.1. Molecular orbitals (MOs) of CS calculated by SA-CASSCF at 1.54 Å, plotted with isovalue 0.08, except 0.02 is used for the 1 σ MO. Contributions from h type orbitals are excluded from this image owing to limitations of the visualization software. In C_{2v}, σ orbitals correspond to a_1 and π orbitals to the pair (b_1, b_2). The MOs are listed according to increasing energy, though not to scale. The orbital shapes depend strongly on internuclear distance.

the MRCI+Q calculation at 1.54 Å. The exact number of configurations varies with internuclear distance, spatial symmetry, and spin multiplicity. The Davidson correction with relaxed references are added to the MRCI energies. TDMs are obtained at the level of MRCI.

For several bound states with obvious potential wells, we calculated the spectroscopic constants from the PECs for comparison with previous calculations and experimental data. First, we obtained the rovibrational energy levels by solving the one-dimensional Schrödinger equation numerically using the DUO program (Yurchenko et al., 2016). Then the spectroscopic constants, including T_e, ω_e, $\omega_e x_e$, B_e, and α_e were determined by fitting the energy levels of the first ten vibrational states.

3.2.2. Photodissociation cross sections.

Photodissociation may occur through one of two main pathways. Absorption into an unbound excited electronic state results in direct dissociation, and is characterized by a broad, weak cross section. Indirect photodissociation on the other hand begins by absorption into a bound excited state, followed by predissociation: non-radiative coupling into a nearby unbound state. Cross sections for indirect photodissociation show resolved or partially-resolved rovibrational transitions associated with the upper electronic state that are lifetime broadened. When the predissociation timescale is fast compared with other relaxation mechanisms (e.g., spontaneous emission), nearly every absorption event leads to dissociation.

The coupled-channel Schrödinger equation (CSE) technique is employed here to study the predissociation mechanisms of CS $^1\Sigma^+$ states. When solving the Schrödinger equation, there are two ways to describe the coupled system of nuclei and electrons. The electronic states calculated by the *ab initio* methods above are in the adiabatic representation, where the electronic Hamiltonian is diagonalized precisely and the couplings between states arise from a nuclear kinetic energy operator. An alternative method uses the diabatic representation, where the nuclear kinetic energy coupling terms are minimized while introducing new couplings that are treated as interactions between different electronic states. The diabatic states approximately follow the same electronic character as a function of internuclear distance, while the adiabatic states' electronic character varies. In principle, these two representations are equivalent after introducing the appropriate coupling terms. For convenience, the diabatic representation is used in this study because the couplings in adiabatic states vary strongly with internuclear distance, which creates difficulties in modeling the predissociation process.

In the CSE method, the complete coupled-wavefunction $\psi_i(\mathbf{r}, R)$ is expressed as a linear combination of a set of N_T diabatic (or adiabatic) electronic rotational states $\phi_j(\mathbf{r}; R)$, which are also called coupled channels

$$\psi_i(\mathbf{r}, R) = \sum_{j=1}^{N_T} \frac{1}{R} \chi_{ij}(R) \phi_j(\mathbf{r}; R) \tag{3.1}$$

where R is the internuclear distance, and $\chi_{ij}(R)$ represent R-dependent expansion coefficients between states $\phi_j(\mathbf{r}; R)$. For a given energy E, the Schrödinger equation for the radial wavefunctions can be written as

$$\frac{\partial^2}{\partial R^2} \chi(R) = -\frac{2\mu}{\hbar^2} \chi(R)[E\mathbf{I} - \mathbf{V}(R)] \tag{3.2}$$

where μ is the reduced mass of the molecule, $\mathbf{I}$ is the identity matrix, and $\mathbf{V}(R)$ is the interaction matrix, which is composed of potential energy curves as diagonal elements and coupling terms (such as non-adiabatic coupling and spin-orbit coupling) as off-diagonal elements.

The spin-orbit couplings and non-adiabatic couplings are calculated by MOLPRO. The spin-orbit couplings for MRCI wavefunctions are calculated by using the full Breit-Pauli operator between internal configurations while contributions of external configurations are calculated by a mean-field one-electron Fock operator. For adiabatic states, the non-adiabatic coupling matrix elements (NACMEs) are computed by finite differences of the MRCI wavefunctions. Details about building the interaction matrix, including obtaining diabatic representations, will be discussed further in Section 3.3.2. Equation (3.2) is solved numerically to give the coupled wavefunctions for mixed upper states.

Assuming alternate decay pathways such as spontaneous emission or collisional relaxation are slow, the total photodissociation cross section from an initial state with J'' is obtained by summing over all open channels γ and all allowed J' (Heays et al., 2010)

$$\sigma_g(\tilde{\nu}) = \sum_{J'} \sum_{\gamma} \left[\frac{\pi \tilde{\nu}}{3\hbar\varepsilon_0} \frac{g}{2J''+1} \sum_k (|\langle \chi_{\gamma k} | M | \chi_g \rangle|^2 S_{J''}^{\Delta J}) \right] \tag{3.3}$$

where $\tilde{\nu}$ is the photon energy in wavenumbers, M is the R-dependent electric-dipole transition moment between the unmixed lower (ground) state with radial wavefunction χ_g and each upper state k with mixed wavefunction $\chi_{\gamma k}$ coupled to open channel γ . The Hönl-London factors $S_{J''}^{\Delta J}$ (Hansson & Watson, 2005; Watson, 2008) which indicate the relationship between the total intensity of a vibronic band and the rotational

quantum numbers can be expressed for these types of transitions as:

$$
\begin{aligned}
{}^1\Sigma^+ - {}^1\Sigma^+ : \quad & S^P_{J''} = J'' \\
& S^R_{J''} = J'' + 1
\end{aligned}
\tag{3.4}
$$

$$
\begin{aligned}
{}^1\Pi - {}^1\Sigma^+ : \quad & S^P_{J''} = (J'' - 1)/2 \\
& S^Q_{J''} = (2J'' + 1)/2 \\
& S^R_{J''} = (J'' + 2)/2
\end{aligned}
\tag{3.5}
$$

for $P(\Delta J = -1)$, $Q(\Delta J = 0)$, and $R(\Delta J = +1)$ branches. In our case, the degeneracy factor g is 1 for a ${}^1\Sigma^+ - {}^1\Sigma^+$ transition and 2 for a ${}^1\Pi - {}^1\Sigma^+$ transition.

For a particular transition, the linewidth can be used to estimate the predissociation timescale τ_{pd} and compared with the spontaneous emission and collision timescales (τ_{se} and τ_{coll}). If $\tau_{pd} << \tau_{se}$ and τ_{coll}, then the calculated cross sections are good estimates of the photodissociation cross section. Otherwise, a time-dependent method should be applied or a tunneling probability η should be included for correction. As shown below, in the case of CS, the predissociation efficiency is essentially 1.

Direct photodissociation is simply a special case of the CSE model in which only one unmixed upper state can be excited from the ground state. Because the upper state is unbound and certain to dissociate, the calculated result is an exact photodissociation cross section. Thus, the CSE approach simultaneously calculates the direct photodissociation cross sections in addition to those that proceed via predissociation. In this study, photodissociation cross sections are calculated with PyDiatomic (Gibson, 2016), which solves the time-independent coupled-channel Schrödinger equation using the Johnson renormalized Numerov method (Johnson, 1978).

Using the CSE method, a rotationless ($J' - J'' = 0 - 0$) transition is calculated for the ground X state with $v'' = 0$. We also calculated the photodissociation cross sections for transitions from the ground state with $v'' = 0, 1, 2$ and different J''. Assuming local thermodynamic equilibrium (LTE), the total photodissociation cross sections at given temperature T are calculated by

$$
\sigma(\lambda, T) = \frac{1}{Q} \sum_i \sigma_i(\lambda) g_i e^{-E_i/k_b T}
\tag{3.6}
$$

where Q is the partition function, E_i is the energy of all achievable ground rovibrational states with rotational degeneracy $g_i = 2J'' + 1$, and k_B is Boltzmann's constant.

3.2.3. Photodissociation rates in astrophysical environments.

The photodissociation rate of a molecule in an UV radiation field is

$$k = \int \sigma(\lambda) I(\lambda) d\lambda \tag{3.7}$$

where $\sigma(\lambda)$ is the photodissociation cross section and $I(\lambda)$ is the radiation intensity. We compute the photodissociation rate of CS from its ground (X) state with $(v'', J'') = (0, 0)$ in the standard interstellar radiation field (ISRF) given by (Draine, 1978). The LTE photodissociation rates for different temperatures are also calculated.

3.3. Results and discussion

The layout of this section is as follows. The PECs and TDMs obtained from *ab initio* calculations are shown in Section 3.3.1, including a highlight on the main feature of our calculations. Then, the details about building the coupled-channel model is discussed in Section 3.3.2. Finally, the dissociation cross sections and rates are presented in Section 3.3.3.

3.3.1. Ab initio calculation.

3.3.1.1. *Optimization of MRCI calculation.*

The accuracy of the calculated photodissociation cross sections relies on the PECs and TDMs obtained from the SA-CASSCF/MRCI+Q calculation. The quality of an MRCI+Q calculation is sensitive to the choice of active space and basis set, both of which require careful consideration. Previous theoretical studies of CS excited states (Pattillo et al., 2018; Shi et al., 2013) used the aug-cc-pV6Z (AV6Z) basis set with the active space CAS(10,8) where the number of active orbitals for each irreducible representation is given as (4,2,2,0). The fact that the properties of the B state calculated by Pattillo et al. (2018) disagree with experiments (Donovan et al., 1970; Stark et al., 1987) suggests this active space is not suitable for accurately calculating highly excited states. One reasonable explanation for the discrepancy is that some dominant configurations of the B state are not included in the reference space because some significantly occupied MOs in those configurations are outside of the active space.

Although there is no golden rule to determine the ideal active space, including more virtual orbitals is generally necessary to improve the quality of the calculation, especially for Rydberg states. Both previous spectroscopic experiments and comparison between CO and CS indicate the B and C states have Rydberg nature, involving high-energy σ type orbitals. Motivated by these experimental observations, we systematically included more a_1 (i.e., σ) virtual orbitals into the active space, and found that at CAS(10,11) (7,2,2,0) the SA-CASSCF/MRCI+Q calculation was stable over the whole internuclear distance range. Smaller active spaces resulted in a stability problem around 2.0 Å.

As the internuclear distance increases, the dominant electron configuration changes in the adiabatic representation. For the ground $X\,^1\Sigma^+$ state, this occurs twice, at 2.1 and 2.8 Å, which can roughly be interpreted as the points at which the C=S double bond breaks stepwise. While the change in configuration itself is straightforward to treat, the changes in the shapes of the MOs themselves causes significant stability problems when the active space is too small. With our active space, we were able to achieve continuous and smooth PECs up to at least the $C\,^1\Sigma^+$ state. Addition of one more σ orbital resulted in a dramatic increase in the single-point calculation time, rendering it impractical for the complete study.

Calculations with smaller basis sets showed that the $5\,a_1$ MO is doubly occupied in the most important configurations for all states we are able to calculate. Therefore to save calculation time, we put the $5\,a_1$ MO into the closed-shell space, resulting in our final active space of CAS(8,10) (6,2,2,0).

Because of our large active space, we could not use the aug-cc-pV6Z basis set as in previous studies. Instead, we used the aug-cc-pV(5+d)Z basis set supplemented with additional diffuse orbitals located on both carbon and sulfur atoms. The total number of AOs in our basis amounts to 299 (112,72,72,43). Keeping the 6 lowest MOs (4,1,1,0) as core MOs, in the MRCI+Q calculation for $^1\Sigma^+$ states at 1.54 Å, from the reference space consisting of 2053 configurations, 1.76×10^7 contracted and 5.03×10^8 uncontracted configurations are generated. In comparison, in the aug-cc-pV6Z basis set there are 382 (134,93,93,62) AOs. To compute the same number of states using the active space CAS(10,8) (4,2,2,0) and the aug-cc-pV6Z basis set, only a total of 1.11×10^7 contracted and 7.00×10^7 uncontracted configurations are produced from the reference space with 240 configurations. Thus, our large reference space is appropriate for calculating both valence and Rydberg states of CS, and justifies using a slightly smaller, tailored basis set.

As a final point, our choice of active space was focused primarily on accurate calculations of $^1\Sigma^+$ states. It is possible that including more π MOs into the active space, such as using CAS(8,12) (6,3,3,0),

would improve the quality of calculation especially for high-lying Π states. However, the large number of configurations we included in the MRCI+Q calculation still promises good accuracy even for non $^1\Sigma^+$ states. Moreover, the spectroscopic constants calculated for low-lying excited states from our PECs match well with experiments where data are available, which enhances our confidence.

3.3.1.2. *PECs and TDMs.*

Employing the approaches described in Sec 3.2.1, we have calculated the PECs of 49 states in total, including 7 $^1\Sigma^+$, 3 $^1\Sigma^-$, 7 $^1\Pi$, 4 $^1\Delta$, 4 $^3\Sigma^+$, 5 $^3\Sigma^-$, 8 $^3\Pi$, 5 $^3\Delta$, 2 $^5\Sigma^+$, 1 $^5\Sigma^-$, 2 $^5\Pi$, and 1 $^5\Delta$. Among all those states, the adiabatic PECs of several $^1\Sigma^+$, $^1\Pi$, $^3\Pi$, and $^3\Sigma^-$ states are shown in Figure 4.3 because they are directly related to the following dissociation study, while all data are available in a machine-readable format in the Appendix with PECs of other states.

The potential energy scale used here is referenced to a zero defined by the potential minimum of the ground state $X\,^1\Sigma^+$. State names are kept consistent for states already tabulated in the NIST database (Huber & Herzberg, 1979). For the ground state and several low-lying excited states, calculated spectroscopic constants are listed in Table 3.2, along with data from previous theoretical calculations and experiments where available. The dissociation energies D_e are estimated to be the calculated MRCI+Q energies at $R = 7.9$ Å. The error induced by long range interactions is estimated to be less than 0.0010 eV based on the formula and quadrupole-quadrupole coefficients given by Pattillo et al. (2018).

Of the 10 singlet electronic states calculated with A_1 symmetry, 6 correspond to $^1\Sigma^+$ at $R = 2.1$ Å: X, A', B, C, 5 and $6\,^1\Sigma^+$. At $R > 2.2$ Å, the $6\,^1\Sigma^+$ is no longer among the first 10 A_1 states in C_{2v}. Since the remaining part of its potential is still helpful to construct diabatic states, we include $6\,^1\Sigma^+$ in Figure 4.3.

The X state is deeply bound with an equilibrium internuclear distance of 1.540 Å and an estimated dissociation energy 7.47 eV. The calculated spectroscopic constants, especially the vibrational constant ω_e, are in excellent agreement with experimental data (Table 3.2). Next is the A' state, which is weakly bound with a much longer equilibrium bond distance, reflecting the fact that its main configuration has one electron excited from a bonding valence MO to an antibonding MO. The B state has two potential wells. The first, at 1.53 Å, lies near an avoided crossing with the A' state, while the second is at 2.06 Å. The C state has its potential minimum at 1.54 Å, which is nearly identical to that of the X state. The shape of the C state about 0.35 eV higher than its equilibrium point is affected by avoided crossings with the B and $5\,^1\Sigma^+$ states. Following a maximum at 1.95 Å, a second weak potential well appears. For both the B and C

TABLE 3.2. Spectroscopic constants for low-lying states of CS

State	Method	R_e ()	T_e (cm^{-1})	ω_e (cm^{-1})	$\omega_e x_e$ (cm^{-1})	B_e (cm^{-1})	$10^3\,\alpha_e$ (cm^{-1})	D_e [a] eV
$X\,^1\Sigma^+$	Calc [b]	1.540	0	1284.1	8.2	0.814	6.0	7.47
	Expt [c]	1.535	0	1285.1	6.5	0.820	5.9	7.43
	Calc [d]	1.533	0	1286.8	4.9	0.822	6.0	7.46
$a\,^3\Pi$	Calc [b]	1.577	27 735.5	1129.9	7.8	0.777	6.9	4.05
	Expt [e]	1.568	27 661.0	1135.1	7.7	0.785	7.2	4.00
	Calc [d]	1.569	27 721.7	1133.6	7.1	0.786	7.7	4.05
$a'\,^3\Sigma^+$	Calc [b]	1.737	31 411.7	832.1	5.9	0.640	5.5	3.59
	Expt [f]	1.725	31 331.4	830.7	5.0	0.649	6.0	3.55
	Calc [d]	1.720	31 310.2	829.4	12.9	0.652	9.1	3.59
$d\,^3\Delta$	Calc [b]	1.753	35 585.8	787.0	3.4	0.629	5.6	3.07
	Expt [f]	1.742	35 675.0	795.6	4.9	0.637	6.1	3.01
	Calc [d]	1.741	35 863.5	795.9	5.3	0.635	7.5	3.04
$e\,^3\Sigma^-$	Calc [b]	1.767	38 470.4	749.8	3.5	0.619	6.2	2.71
	Expt [g]	1.766	38 683.0	752	4.7	0.619	4.0	2.64
	Calc [d]	1.762	38 810.6	751.4	4.5	0.622	6.6	2.67
$A\,^1\Pi$	Calc [b]	1.575	38 779.4	1052.4	9.2	0.780	8.9	2.67
	Expt [g]	1.574	38 904.4	1073.4	10.1	0.780	6.3	2.61
	Calc [d]	1.565	38 943.2	1075.0	9.2	0.784	7.4	2.65
$1\,^1\Sigma^-$	Calc [b]	1.771	38 622.9	744.6	4.8	0.616	6.5	2.69
	Calc [d]	1.767	39 398.3	746.7	6.1	0.618	6.4	2.65
$1\,^1\Delta$	Calc [b]	1.778	39 626.9	718.0	3.9	0.611	6.8	2.59
	Calc [d]	1.777	40 197.7	723.2	5.7	0.612	6.6	2.54
$A'\,^1\Sigma^+$	Calc [b]	1.945	55 960.2	464.9	3.2	0.511	11.0	0.55
	Expt [h]	1.944	56 505	462.4	7.5	0.511	10.9	0.43
	Calc [d]	1.958	57 115.3	459.4	1.7	0.496	2.5	0.41
$X\,^2\Sigma^+$	Calc [b]	1.500	0	1369.8	9.1	0.859	6.3	11.34[i]
(CS^+)	Expt [j]	1.492	0	1376.6	7.8	0.867	6.5	11.32[k]

a. Experimental D_e of $X\,^1\Sigma^+$ is determined by adding energy of $v = 0$ to $D_0^0 = 7.355$ eV (Coppens & Drowart, 1995). Experimental D_e of other states are estimated by D_e ($X\,^1\Sigma^+$) and their T_e.
b. this work.
c. (Huber & Herzberg, 1979; Kewley et al., 1963; Lovas & Krupenie, 1974; Mockler & Bird, 1955).
d. (Shi et al., 2013).
e. (Cossart & Bergeman, 1976; Huber & Herzberg, 1979; Taylor et al., 1972; Tewarson & Palmer, 1968).
f. (Barrow et al., 1960; Cossart & Bergeman, 1976; Field & Bergeman, 1971; Huber & Herzberg, 1979).
g. (Barrow et al., 1960; Huber & Herzberg, 1979).
h. (Bell et al., 1972).
i. Calculated ionization energy of CS ground X state.
j. (Gauyacq & Horani, 1978).
k. Experimental ionization energy of CS ground X state (Coppens & Drowart, 1995).

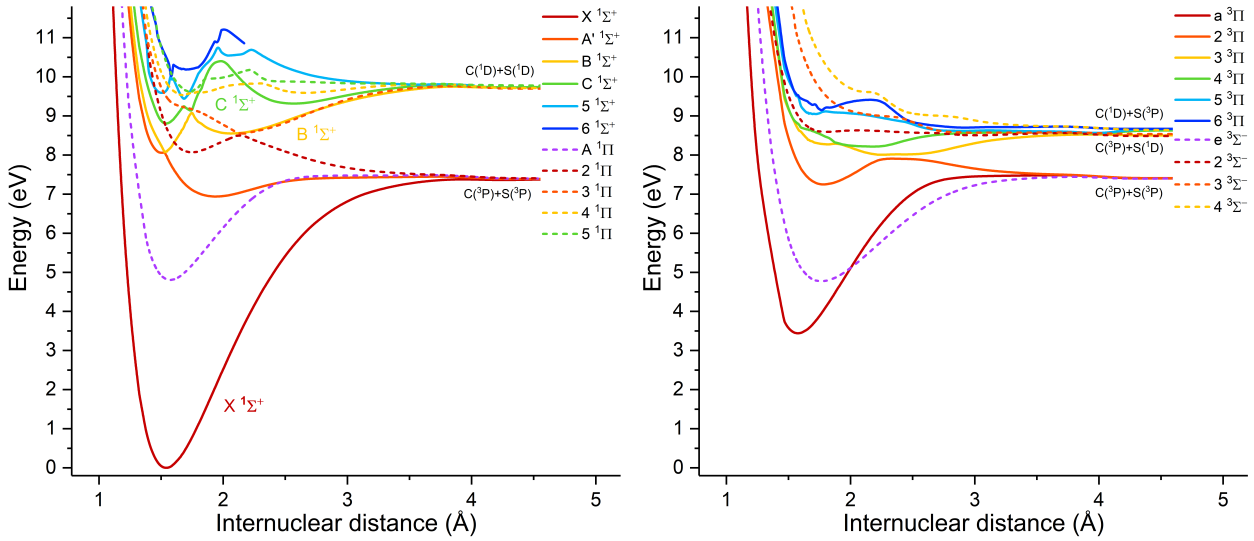

FIGURE 3.2. Adiabatic potential energy curves for CS $^1\Sigma^+$, $^1\Pi$ (left), $^3\Pi$, and $^3\Sigma^-$ (right) electronic states

states, the potential well near 1.50 Å corresponds to a Rydberg configuration, while the second well toward larger distances corresponds to a valence-bound electron configuration. A more detailed discussion of the spectroscopic properties of the *B* and *C* states can be found in section 3.3.3. The 5 and 6 $^1\Sigma^+$ states have complicated potential curves, possibly arising from avoided crossings with still higher states.

The five $^1\Pi$ states are shown in Figure 4.3. The $A\,^1\Pi$ state has a calculated equilibrium internuclear distance of 1.575 Å with potential minimum of 38779.4 cm^{-1}, which is only 125 cm^{-1} lower than the experimental value. The calculated harmonic vibrational constant is 21 cm^{-1} smaller than the experimental value of 1073.4 cm^{-1}. No experimental data are available to compare with the higher-lying $^1\Pi$ states. Our calculations indicate that the 2 and 3 $^1\Pi$ states have a prominent avoided crossing around 2.1 Å. Finally, the 4 and 5 $^1\Pi$ states lie close in energy and have unusual shapes, indicating significant Rydberg-valence mixing. The $E\,^1\Pi$ state identified in the spectrum of Donovan et al. (1970) may be composed of a combination of the 2, 3, 4, and 5 adiabatic states in a diabatic representation. However, as discussed in more detail later, construction of such a complex diabatic state is complicated and we did not pursue this further.

The $1\,^1\Sigma^-$ state has a potential minimum of 38622.9 cm^{-1} at R = 1.771 Å. while the $1\,^1\Delta$ state has a calculated equilibrium internuclear distance of 1.778 Å with a potential minimum of 39626.9 cm^{-1}. They are almost degenerate, indicating that they share similar configurations. Because direct excitation from the ground state is forbidden, no experimental data are available for comparison. Our T_e values are about 800 and

600 cm^{-1} lower respectively than those fitted by Shi et al. (2013) for the $^1\Sigma^-$ and $^1\Delta$ states, and our calculated R_e values are in good agreement with theirs. The 2 $^1\Sigma^-$ and 2, 3, and 4 $^1\Delta$ states are either unbound or very weakly bound, converging to the C (^1D) + S (^1D) atomic limit.

The remaining electronic states of CS that correlate to one of the 4 lowest-energy atomic limits are triplet and quintet states. Quintet states are not involved in the photodissociation of ground-state CS and will not be discussed further. Triplet states, however, may play an important role in the predissociation of $^1\Sigma^+$ states via the spin-orbit interaction as suggested by Donovan et al. (1970) even though direct excitation is forbidden from the ground state. The main features of the triplet state PECs from our calculations are briefly summarized here.

The $a'\,^3\Sigma^+$ state has an equilibrium distance of 1.737 Å with a potential minimum 31411.7 cm^{-1}, which is only about 80 cm^{-1} larger than the experimental value. The 2 and 3 $^3\Sigma^+$ states have an avoided crossing at 1.98 Å, and the local maximum at 1.77 Å of the 3 $^3\Sigma^+$ state represents a Rydberg-valence mixing.

Next, the $e\,^3\Sigma^-$ state has a potential minimum of 38470.4 cm^{-1} at R = 1.767 Å, and its calculated spectroscopic constants agree well with experimental data. Higher-energy $^3\Sigma^-$ states are unbound and converge to either the C (^3P) + S (^1D) or C (^1D) + S (^3P) atomic limits.

The $a\,^3\Pi$ state has the potential minimum of 27735.5 cm^{-1} at R = 1.577 Å, and its calculated vibrational constant is 1129.9 cm−1, only 5.2 cm^{-1} smaller than experimental value. An avoided crossing between the 2 and 3 $^3\Pi$ states spans R = 2.25 to 2.50 Å and another one between the 3 and 4 $^3\Pi$ states lies at R = 1.94 Å. The PECs of higher $^3\Pi$ states are close to each other, with complicated potential structures.

Finally, the $d\,^3\Delta$ state has an equilibrium bond length of 1.753 Å with potential energy minimum of 35585.8 cm^{-1}. The fitted spectroscopic constants are in good agreement with those obtained by experiments. Higher $^3\Delta$ states are either unbound or have shallow potential wells.

Among all these states, only those of $^1\Sigma^+$ and $^1\Pi$ symmetry are directly accessible from the ground X state by radiative transitions, according to the selection rules for heteronuclear diatomic molecules in Hund's case (a) and (b)

$$\Delta\Lambda = 0, \pm 1; \quad \Delta S = 0; \quad + \nleftrightarrow - \tag{3.8}$$

Thus, they are expected to play the most important role in the photodissociation of CS in astronomical environments. Transition dipole moments from the ground X state to excited $^1\Sigma^+$ and $^1\Pi$ states are shown

in Figure 4.6. We find that the C and $5\,\Sigma^+$ states have much larger transition dipole moments compared with all other states. Most importantly, the transition dipole moment of the C state is 1.5 a.u. at 1.54 Å, which is the equilibrium internuclear distance for both the X and $C\,^1\Sigma^+$ states. This indicates that the $C - X$ $(0 - 0)$ transition should be extremely strong, which agrees with the experimental VUV absorption spectra of Donovan et al. (1970) and Stark et al. (1987). Among $^1\Pi$ states, $3\,^1\Pi$ has the largest transition dipole moment, which is about 0.7 a.u..

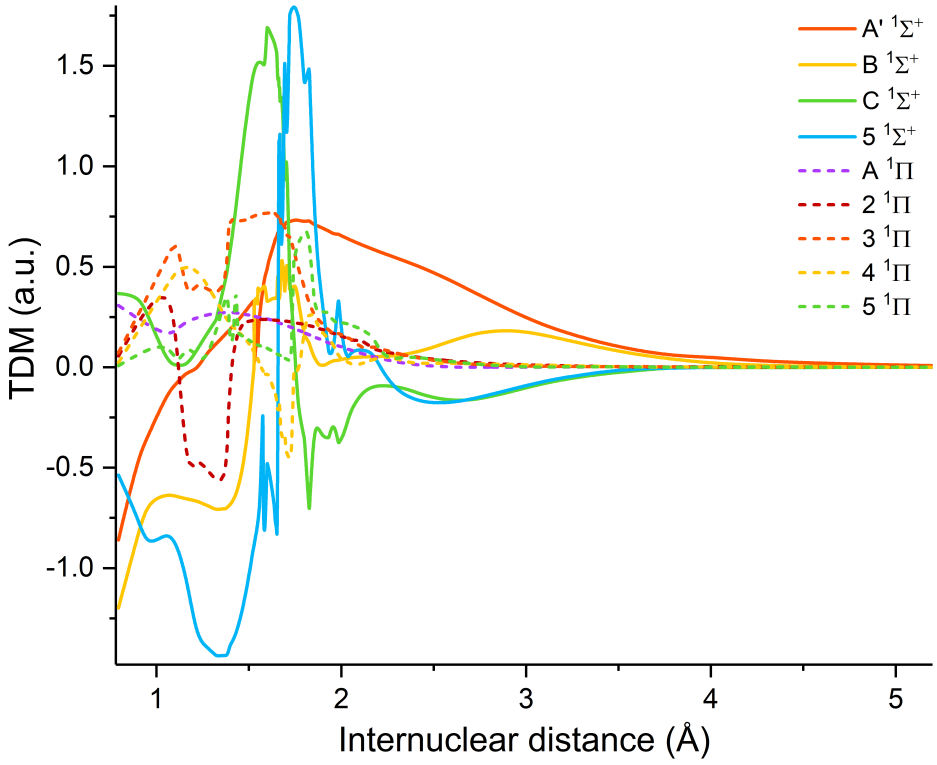

FIGURE 3.3. Transition dipole moments between the ground electronic state of CS and each excited state

To verify our transition dipole moment calculations, we determined f-values for the $A - X$ system for comparison with available experimental and theoretical results (e.g., Carlson et al., 1979; Li et al., 2013; Mahon et al., 1997; Ornellas, 1998). The suite of oscillator strengths is in excellent agreement. A selection of representative values appears in Table 3.3.

In their tentative detection of the CS $C - X$ band in diffuse molecular gas, Destree et al. (2009) required estimates of the oscillator strength to derive the column density. To do this, they adopted an f-value of 0.14 for the $C - X$ $(0 - 0)$ band based on that for the isovalent molecule CO (Federman et al., 2001). However, our

TABLE 3.3. Calculated f-values for the $A - X$ system

Band	$f_{v'v''}$ ($\times 10^2$)			Band	$f_{v'v''}$ ($\times 10^2$)		
($v' - v''$)	This work	Expt [a]	Theory [b]	($v' - v''$)	This work	Expt [a]	Theory [b]
(0 - 0)	1.19	0.96	1.16	(3 - 0)	0.00	···	0.00
(0 - 1)	0.17	0.12	0.16	(3 - 1)	0.08	0.06	0.10
(0 - 2)	0.02	0.01	0.02	(3 - 2)	0.55	0.44	0.56
(0 - 3)	0.00	···	0.00	(3 - 3)	0.17	0.15	0.11
(0 - 4)	0.00	···	0.00	(3 - 4)	0.29	0.24	0.26
(0 - 5)	0.00	···	0.00	(3 - 5)	0.12	···	0.11
(1 - 0)	0.27	0.20	0.28	(4 - 0)	0.00	···	0.00
(1 - 1)	0.74	0.63	0.69	(4 - 1)	0.01	···	0.01
(1 - 2)	0.27	0.20	0.26	(4 - 2)	0.15	0.12	0.19
(1 - 3)	0.05	0.03	0.04	(4 - 3)	0.56	0.45	0.53
(1 - 4)	0.00	···	0.00	(4 - 4)	0.03	0.03	0.01
(1 - 5)	0.00	···	0.00	(4 - 5)	0.23	···	0.19
(2 - 0)	0.02	0.02	0.03	(5 - 0)	0.00	···	0.00
(2 - 1)	0.45	0.35	0.47	(5 - 1)	0.00	···	0.00
(2 - 2)	0.40	0.35	0.34	(5 - 2)	0.02	0.02	0.03
(2 - 3)	0.30	0.24	0.29	(5 - 3)	0.25	0.20	0.29
(2 - 4)	0.08	0.06	0.08	(5 - 4)	0.48	0.39	0.41
(2 - 5)	0.01	···	0.01	(5 - 5)	0.00	···	0.01

a. Derived from lifetime measurements of R-branch band heads with an inherent ~10% uncertainty in general (Carlson et al., 1979).
b. Calculated by CASSCF/MRCI (Ornellas, 1998).

calculations yield a significantly larger f-value of 0.45 owing to the large transition dipole moment for CS. With the larger CS f-value derived here, the column density inferred from the astronomical observations is substantially reduced; consequently, the expected amount of absorption of the $A - X$ $(0 - 0)$ transition at 257.7 nm ($f = 0.096$) is also much less, and well below the upper limit available from the astronomical measurements.

3.3.2. Coupled-channel model.

Several of the high-energy PECs feature avoided crossings, and in particular the B and C states are likely to share resonant levels with unbound states and therefore may decay by predissociation. Because the typical timescale for predissociation is much faster than spontaneous emission for small diatomic molecules,

it is normally reasonable to treat their dissociation efficiency, η_d, as unity in a collision-free environment. All photoabsorption is therefore expected to lead to dissociation (Heays et al., 2017). Experimental line broadening observed in the $B - X$ and $C - X$ bands supports the fast predissociation of CS (Donovan et al., 1970; Stark et al., 1987). In this study, we use the CSE method to investigate the predissociation of CS in detail.

The CSE approach has been described by van Dishoeck et al. (1984) and Heays et al. (2010). It has been previously used to study predissociation of other diatomic molecules, including N_2 (Heays et al., 2015), O_2 (Gibson & Lewis, 1996; Lewis et al., 2001), and S_2 (Lewis et al., 2018), yielding good agreement between computed and experimental cross sections. In those studies, diabatic PECs are typically constructed from experimentally measured rovibrational energy levels using, for instance, the Rydberg-Klein-Rees (RKR) method. Then, the coupling terms and transition dipole moments are fitted iteratively by comparing the calculated cross sections, resonance positions, and widths with measured values. However, for many of the important predissociative states of CS, the available spectroscopic data for CS are insufficient to allow such methods. We aim to obtain the photodissociation cross sections from pure *ab initio* calculations.

Building the coupled-channel model consists of constructing the interaction matrix $V(R)$, whose diagonal elements are diabatic PECs and off-diagonal elements represent couplings between states. The wavefunctions of the coupled states are obtained from the interaction matrix and are used to derive the cross sections. It is impractical to include all states into the model because of the high density of states with energies above 8 eV. Motivated by the strong absorption bands observed by Donovan et al. (1970) and Stark et al. (1987), our model focuses primarily on treating predissociation originating in the B and C states.

We constructed diabatic PECs of the A', B, C, and $3'\,^1\Sigma^+$ states from the adiabatic ones (Lefebvre-Brion & Field, 2004). Although it is theoretically possible to diabatize the PECs by applying the adiabatic-to-diabatic transformation matrix, which can be calculated from the non-adiabatic coupling matrix elements (NACME) (Baer, 2006), we did not use this method for three main reasons. First, calculation of the matrix at each internuclear distance requires an integral of the NACME from infinite separation. Small errors in each NACME may accumulate during the integration and yield artificial PECs. Second, solving the matrix is difficult for a system larger than two states, and the procedure is even more complicated in this case because the crossings between B, C, and $5\,^1\Sigma^+$ states are close. Moreover, the NACMEs are calculated only at the MRCI level, corresponding to MRCI energies shown in Figure 4.9. The MRCI+Q energies, which include

the Davidson correction, are more accurate and smoother. Instead, we diabatize the states by exchanging the adiabatic MRCI+Q energies on both sides of the crossing ranges and connecting the PEC segments linearly. For B and C states beyond our data region, we extend their PECs according to the shape of MRCI+Q PEC of CS^+ calculated with the same basis set and active space.

Initial values for the R-independent diabatic coupling matrix elements, H^e, are estimated to be half the energy gaps at the crossing points shown in Figure 4.3 (Lefebvre-Brion & Field, 2004). For example, the diabatic coupling between the B and $3'$ states corresponds to the coupling between the B and C states in the adiabatic representation. The B and $3'$ diabatic potentials cross at 1.74 Å, with an MRCI+Q energy difference of 566 cm^{-1} between B and C diabatic states, yielding an estimate for $H^e(B, 3')$ of 283 cm^{-1}.

We explored another method to estimate the diabatic coupling matrix elements without numerical integration (Lefebvre-Brion & Field, 2004). Normally it can be assumed that the energy differences between two diabatic potentials, $E_1^d(R)$ and $E_2^d(R)$, vary linearly with internuclear distance R in the crossing region

$$E_1^d(R) - E_2^d(R) = a(R - R_c) \tag{3.9}$$

where R_c is the crossing point of these two potentials and a is the linear coefficient. Then the shape of the NACME forms a Lorentzian peak near R_c with a full width at half maximum (FWHM) of $4H^e/a$:

$$\left\langle \psi_1^{ad} \left| \frac{\partial}{\partial R} \right| \psi_2^{ad} \right\rangle_R = \frac{H^e/a}{4(H^e/a)^2 + (R - R_c)^2} \tag{3.10}$$

Thus, H^e can be estimated by:

$$H^e = \frac{a \times \mathrm{FWHM}}{4} \tag{3.11}$$

The NACMEs between adiabatic states calculated by MOLPRO do not include the Davidson correction (+Q); their values and the corresponding MRCI energies are shown in Figure 4.9. A higher and narrower NACME peak between adiabatic states means weaker coupling between the diabatic states. For the same example mentioned above, a is calculated to be 11.4 eV/Å and the FWHM is 0.036 Å, which results in H^e = 827 cm^{-1}. This number disagrees with the above value of 283 cm^{-1}. Instead, it matches with the half energy gap 788 cm^{-1} at the crossing point at 1.75 Å in the MRCI PEC, shown in Figure 4.9. This latter approach fails because the Davidson correction contributes significantly to the energies of the excited states, especially near the avoided crossings in the MRCI calculation.

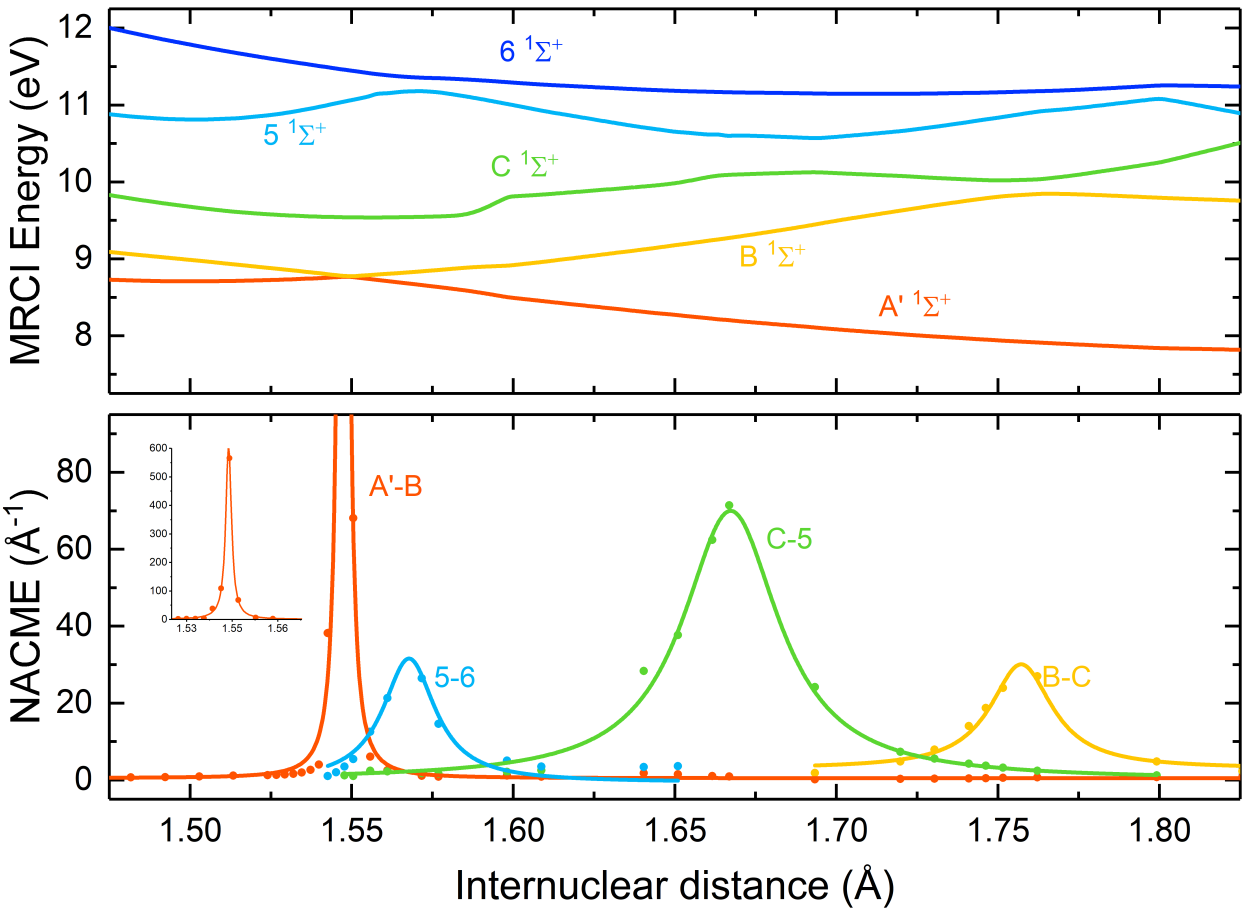

FIGURE 3.4. Adiabatic MRCI/aug-cc-5V(5+d)Z PECs for excited $^1\Sigma^+$ states (without the Davidson correction), along with their calculated NACMEs.

Diabatic PECs can be readily transformed back to adiabatic PECs by diagonalizing the diabatic interaction matrix $V(R)$. Adiabatic PECs derived from our diabatic model in this manner should therefore agree with the calculated MRCI+Q energies. To improve our estimates of the diabatic state couplings, we manually refine their values to minimize the differences between the adiabatic energies derived from diagonalizing $V(R)$ and the *ab initio* energies. The result is shown in Figure 3.5. The perfect overlap between MRCI+Q data and adiabatic PECs validates our diabatization process.

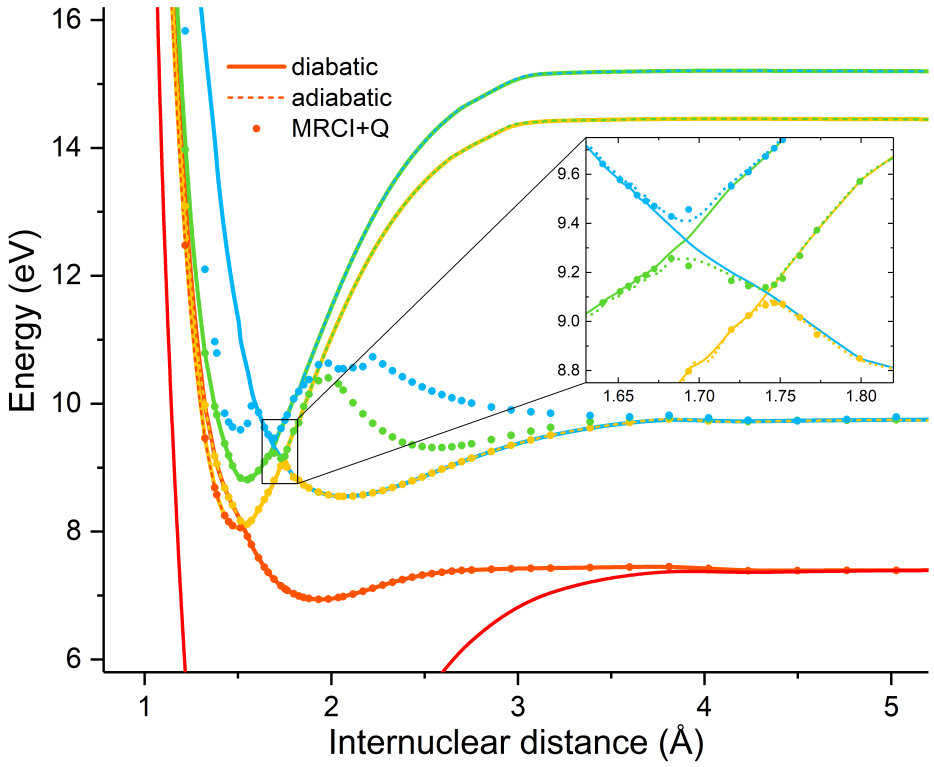

FIGURE 3.5. $^1\Sigma^+$ states of CS: MRCI+Q *ab initio* energies, constructed diabatic PECs, and their corresponding adiabatic PECs obtained by diagonalizing the diabatic interaction matrix $V(R)$.

We also include states of $^3\Sigma^-$ and $^3\Pi$ symmetry in the coupled-channel model because they have non-vanishing spin-orbit coupling (SOC) terms with $^1\Sigma^+$ states according to the selection rules:

(3.12a) $$\Delta J = \Delta\Omega = 0; \quad \Delta S = 0, \pm 1; \quad \Sigma^+ \leftrightarrow \Sigma^-$$

(3.12b) $$\Delta\Lambda = \Delta\Sigma = 0 \text{ or } \Delta\Lambda = -\Delta\Sigma = \pm 1$$

In addition, obvious avoided crossings exist between the adiabatic 2, 3, and 4 $^3\Pi$ states, as shown in Figure 4.3, and these must be included in the model. Diabatic PECs of 2, 3, and 4 $^3\Pi$ states are constructed using the same method described above. PECs of the higher-energy 5 and 6 $^3\Pi$ states are not smooth around 1.6 Å, indicating strong coupling between them that is difficult to incorporate into the diabatic model. However, because both states are dissociative, interactions between them do not affect the overall photodissociation cross section (though they may have a small effect on the atomic product fractions), so we ignore them in our

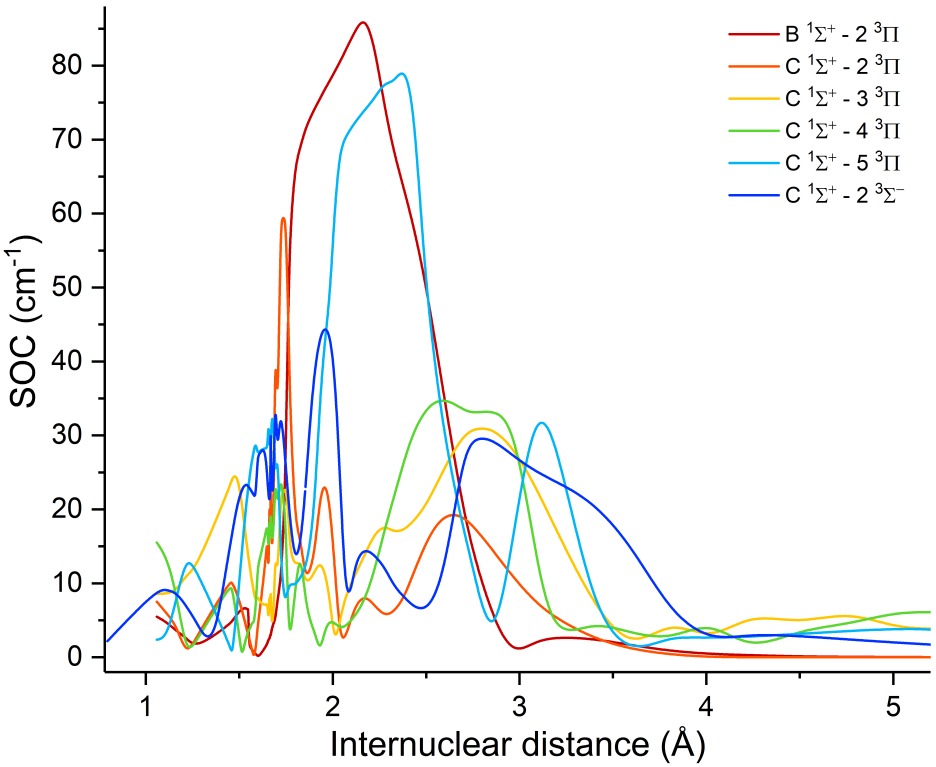

FIGURE 3.6. Several important spin-orbit couplings between $^1\Sigma^+$ and $^3\Pi$ states

model. No clear crossings occur between the 2, 3 and 4 $^3\Sigma^-$ states, so they are also treated as independent diabatic states in our coupled-channel model.

Finally, we must include the SOCs among these diabatic states. Several important SOCs between the adiabatic states are shown in Figure 4.11, while all others are given in the Appendix. Because of the complicated adiabatic-to-diabatic transformation of $^1\Sigma^+$ states, it is almost impossible to build R-dependent spin-orbit coupling curves for diabatic states. For this reason we assume that the spin-orbit interaction can be treated as R-independent, and use the values of the SOC matrix elements at the curve crossing points in the CSE model. This is generally a reasonable approximation when two states interact via a curve crossing. For instance, Lewis et al. (2018) used this approach to fit an R-independent value for the $\left\langle 1\,^5\Pi_{u0}\right| \mathbf{H}^{\mathrm{SO}} \left|B\,^3\Sigma^-_{u0}\right\rangle$ matrix element for S_2 to experimental data, obtaining a value within 10% of the *ab initio* value calculated at the crossing point. Since the crossings between $^3\Pi$ and $^3\Sigma^-$ are at longer internuclear distances and also above the dissociation limits, the couplings between them are unlikely to change the predissociation behavior of $^1\Sigma^+$ states. We therefore do not consider the spin-orbit couplings between $^3\Pi$ and $^3\Sigma^-$ states

in our model. The SOCs are calculated in MOLPRO at the MRCI level, as described in Section 3.2.1. To convert $\langle {}^1A_1|H_{\rm SO}|{}^3B_1\rangle$ in the C_{2v} representation to $\langle {}^1\Sigma^+|H_{\rm SO}|{}^3\Pi\rangle$ in the $C_{\infty v}$ representation, a factor of $\sqrt{2}$ is applied.

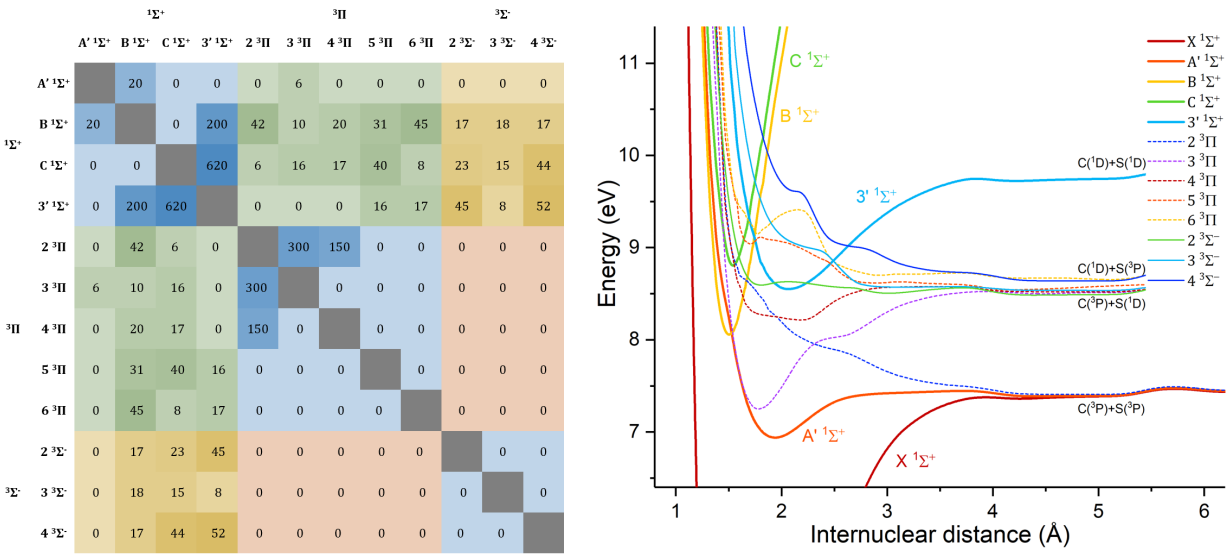

FIGURE 3.7. Coupled-channel model built for $^1\Sigma$ diabatic states. Left: interaction matrix $V(R)$ off-diagonal elements. Right: PECs of included diabatic states.

The final potentials and coupling matrix for predissociation of the $^1\Sigma^+$ states are shown in Figure 3.7. The diagonal elements are R-dependent potentials, while the non-diagonal elements represent the R-independent coupling terms.

In addition, when calculating photodissociation cross sections for $^1\Pi$ states, we followed a similar procedure to construct a coupled channel model for the 2 and 3 $^1\Pi$ states because they have an obvious crossing at 2.15 Å. Only direct photodissociation is calculated for the A, 4, and 5 $^1\Pi$ states.

3.3.3. Photodissociation cross sections and rates.

From the coupled-channel model of the $^1\Sigma^+$ states, we calculated the rotationless photodissociation cross sections from the $v'' = 0$ and $v'' = 1$ vibrational levels of the ground X electronic state, without taking Hönl-London factor into consideration. They are shown in Figure 3.8. The spectroscopic line assignments are listed in Table 3.4. Predissociation lifetimes τ_{pd} are calculated from the width γ of the peaks (Kirby &

Van Dishoeck, 1989)

$$\tau_{pd} = \frac{\hbar}{\gamma} = \frac{5.3 \times 10^{-12}}{\gamma} \tag{3.13}$$

if τ_{pd} is in s and γ is in cm^{-1}. Spontaneous emission lifetimes τ_{se} are derived from the inverse of the Einstein A coefficients calculated based on the integrated cross sections (σ_0) of those peaks. Those values are also included in Table 3.4 for comparison. From the calculation, we were also able to determine the dominant predissociation pathways for each transition, which are listed in Table 3.5.

A comparison between the rotationless vibronic transition frequencies derived from our coupled channel model and the experimental frequencies of Donovan et al. (1970) and Stark et al. (1987) provides strong support for the accuracy of our approach. Our calculated $B - X$ transition frequencies are all slightly greater than the corresponding experimental values by $\sim 150\,\mathrm{cm}^{-1}$, while those of the $C - X$ band are $\sim 200\,\mathrm{cm}^{-1}$ smaller than experimental values. Considering the complexity of this calculation, and the fact that it is purely *ab initio* with no empirical refinement, the agreement is quite satisfactory.

Linewidths of the calculated $B - X$ and $C - X$ cross sections confirm their predissociative nature, especially for the origin band transitions. All the transitions listed in Table 3.4 can be treated as pure photodissociation lines in the low density conditions of the ISM because predissociation lifetimes τ_{pd} are much smaller than the spontaneous emission lifetimes τ_{se}. In the experimental VUV spectrum of the $B - X$ transition (Stark et al., 1987), only the $(1 - 0)$ band showed resolvable rotational structure. This matches our calculation, in which the $1 - 0$ transition has the narrowest linewidth among the three transitions arising from $v'' = 0$. The $C - X$ $(0 - 0)$ transition has the largest cross section among all transitions from $v'' = 0$ considered here by at least a factor of 30 owing to its large transition dipole moment and Franck-Condon factor. Its linewidth of $0.66\,\mathrm{cm}^{-1}$ corresponds to $\tau_{\mathrm{pd}} = 8.0\,\mathrm{ps}$, which is over 80 times faster than τ_{se} (0.66 ns).

The CSE method is also able to give the atomic product channels for each transition. For all $B - X$ transitions, the dominant decay pathway is nonadiabatic coupling to the $A'\,^1\Sigma^+$ state, leading to the ground-state C(^3P) + S(^3P) atomic products. A small percentage ($\sim 15\%$) couples to the $2\,^3\Pi$ state via the spin-orbit interaction, but this also leads to the same atomic limit. The ground vibrational level of the C state is calculated to primarily predissociate via the 2, 3, 4 and $5\,^3\Pi$ states by spin-orbit couplings. Among these, the $2\,^3\Pi$ is a minor channel corresponding to the C (^3P) + S (^3P) atomic limit, while all others (representing 89% of the total coupling) give rise to C (^3P) + S (^1D) products.

The photodissociation cross sections from $^1\Pi - X$ transitions are shown in Figure 3.8.

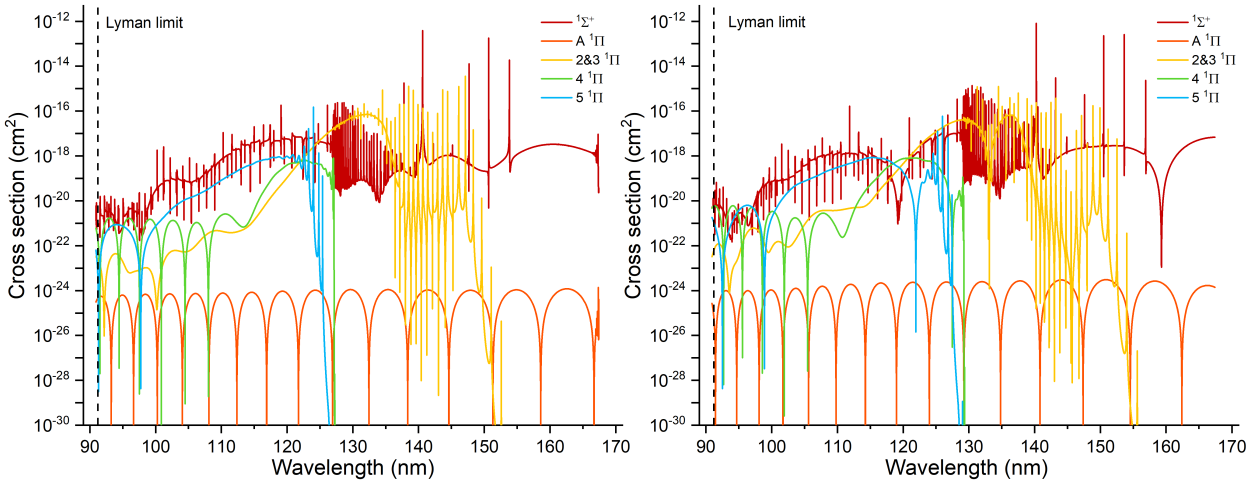

FIGURE 3.8. Rotationless photodissociation cross sections of $^1\Sigma^+$ and $^1\Pi$ states, $v'' = 0$ (left) and $v'' = 1$ (right).

TABLE 3.4. Properties of the $B - X$ and $C - X$ transitions of CS

Band		ν_{expt} [a] (cm^{-1})	ν_{expt} [b] (cm^{-1})	ν (cm^{-1})	γ (cm^{-1})	σ_0 ($\text{cm}^2\text{cm}^{-1}$)	τ_{pd} (ns)	A (s^{-1})	τ_{se} (ns)
$B - X$	(0-0)	64869[c]	64893[c]	65011.7	0.50	1.5×10^{-14}	1.1×10^{-2}	4.8×10^{7}	2.1×10^{1}
	(1-0)	66225[c]	66225[c]	66363.7	0.02	5.4×10^{-15}	2.6×10^{-1}	1.8×10^{7}	5.6×10^{1}
	(2-0)	67560[c]	···	67718.6	0.02	4.3×10^{-16}	2.6×10^{-1}	1.5×10^{6}	6.7×10^{2}
	(1-1)	64934[d]	···	65087.2	0.02	7.8×10^{-15}	2.6×10^{-1}	2.5×10^{7}	4.0×10^{1}
$C - X$	(0-0)	71388[e]	71327[e]	71117.7	0.66	4.0×10^{-13}	8.0×10^{-3}	1.5×10^{9}	6.6×10^{-1}
	(1-0)	···	···	72571.5	0.28	8.0×10^{-16}	1.9×10^{-2}	3.2×10^{6}	3.2×10^{2}
	(1-1)	···	71480[e]	71295.0	0.28	3.7×10^{-13}	1.9×10^{-2}	1.4×10^{9}	7.1×10^{-1}

a. (Stark et al., 1987).
b. (Donovan et al., 1970).
c. Band origin.
d. Band head position (band origin was not reported).
e. Center wavenumber of observed band.

Rovibronic transitions are then calculated with applying appropriate selection rules and Hönl-London factors. Local thermodynamic equilibrium (LTE) cross sections are obtained using the method described in Section 3.2.2. The LTE cross sections at temperature 500 K are shown in Figure 3.9. The rotational constant of the $B(v = 1)$ state is calculated to be $0.846\,\text{cm}^{-1}$ from the spectrum of the $B - X$ $(1 - 0)$ transition shown

TABLE 3.5. Dominant predissociation pathways and product branching fractions for the $B - X$ and $C - X$ transitions of CS.

Transition	Band	Channel	Percent	Atomic products
	(0-0)	$A'\,^1\Sigma^+$	85.5	C(^3P)+S(^3P)
		$2\,^3\Pi$	14.5	C(^3P)+S(^3P)
$B - X$	(1-0)	$A'\,^1\Sigma^+$	96.0	C(^3P)+S(^3P)
		$2\,^3\Pi$	4.0	C(^3P)+S(^3P)
	(2-0)	$A'\,^1\Sigma^+$	95.1	C(^3P)+S(^3P)
		$2\,^3\Pi$	4.9	C(^3P)+S(^3P)
	(0-0)	$4\,^3\Pi$	48.1	C(^3P)+S(^1D)
		$5\,^3\Pi$	30.9	C(^3P)+S(^1D)
		$2\,^3\Pi$	11.0	C(^3P)+S(^3P)
		$3\,^3\Pi$	10.0	C(^3P)+S(^1D)
$C - X$	(1-0)	$5\,^3\Pi$	35.5	C(^3P)+S(^1D)
		$4\,^3\Pi$	30.2	C(^3P)+S(^1D)
		$2\,^3\Sigma^-$	15.1	C(^3P)+S(^1D)
		$2\,^3\Pi$	11.0	C(^3P)+S(^3P)
		$3\,^3\Pi$	7.7	C(^3P)+S(^1D)

in the Appendix, which is almost same as $0.852\,\mathrm{cm}^{-1}$ obtained from the measured spectrum (Stark et al., 1987).

By combining the calculated cross sections and the ISRF (Draine, 1978), the total photodissociation rate of CS at different temperatures are shown in Table 3.6, compared with the results obtained by Pattillo et al. (2018) and the standard values in the Leiden photodissociation database (Heays et al., 2017). The dominant transition responsible for the photodissociation of CS in space is the $C - X$ $(0 - 0)$ band, comprising about 57% of the total photodissociation in the rotationless case. Dissociation through $^1\Pi$ states contribute about 32% to the overall rate. Our calculated rate is a factor of 7.7 larger than that calculated by Pattillo et al. (2018) and a factor of about 3.0 larger than the value adopted by Heays et al. (2017).

At higher energies, Donovan et al. (1970) identified three bands at 122.93, 121.10, and 121.91 nm, which were in turn tentatively assigned as the $G\,^1\Pi - X$ (0-0) and (1-0) transitions as well as a forbidden transition. Because these transitions occur near Ly-α, they may provide important contributions to the total CS photodissociation rate in regions where Ly-α is dominant. Our calculations do not show bands that match those reported in the 122 nm region. The calculated $^1\Sigma^+$ states show a smooth cross section due to direct

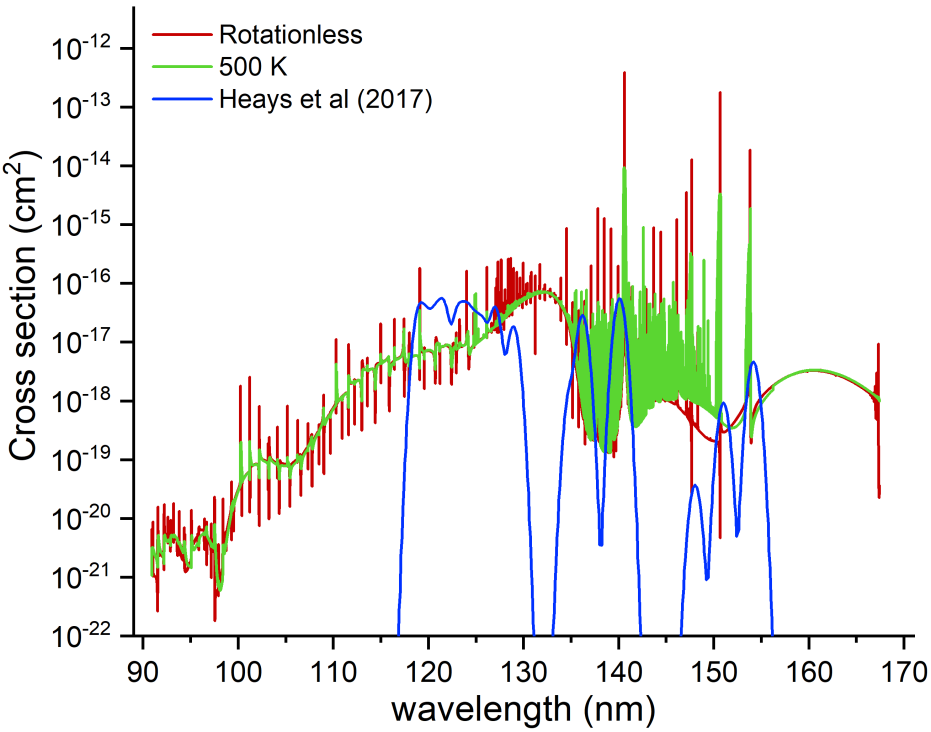

FIGURE 3.9. Photodissociation cross sections calculated at LTE temperature 500 K, compared with data adopted in Heays et al. (2017).

TABLE 3.6. CS photodissociation rates (s^{-1}) under the standard ISRF (Draine, 1978).

Source		Rotationless	20 K	100 K	500 K	Pattillo et al. (2018)	Heays et al. (2017)
$B-X$	(0-0)	7.03×10^{-11}	7.11×10^{-11}	7.10×10^{-11}	6.82×10^{-11}	...	...
	(1-0)	4.50×10^{-12}	4.41×10^{-11}	3.43×10^{-11}	2.61×10^{-11}	...	...
	(2-0)	8.71×10^{-13}	3.95×10^{-12}	4.15×10^{-12}	3.01×10^{-12}	...	...
$C-X$	(0-0)	1.64×10^{-9}	1.64×10^{-9}	1.64×10^{-9}	1.64×10^{-9}	...	...
	(1-0)	3.24×10^{-12}	3.24×10^{-12}	3.29×10^{-12}	3.58×10^{-12}	...	...
Remaining $^1\Sigma^+-X$		2.33×10^{-10}	1.95×10^{-10}	2.18×10^{-10}	2.39×10^{-11}	...	...
All $^1\Sigma^+-X$		1.96×10^{-9}	1.96×10^{-9}	1.97×10^{-9}	1.98×10^{-9}	1.94×10^{-10}	...
$A\,^1\Pi-X$		6.57×10^{-17}	6.57×10^{-17}	6.61×10^{-17}	6.88×10^{-17}	1.50×10^{-21}	...
2 and $3\,^1\Pi-X$		8.84×10^{-10}	8.84×10^{-10}	8.85×10^{-10}	9.07×10^{-10}	1.35×10^{-10}	...
$4\,^1\Pi-X$		7.14×10^{-12}	7.14×10^{-12}	7.11×10^{-12}	6.96×10^{-12}	4.05×10^{-11}	...
$5\,^1\Pi-X$		1.54×10^{-11}	1.55×10^{-11}	1.58×10^{-11}	1.62×10^{-11}	...	...
All $^1\Pi-X$		9.07×10^{-10}	9.06×10^{-10}	9.08×10^{-10}	9.30×10^{-10}	1.76×10^{-10}	...
Total		2.86×10^{-9}	2.87×10^{-9}	2.88×10^{-9}	2.91×10^{-9}	3.70×10^{-10}	9.49×10^{-10}

photodissociation in this region, and while the 4 and 5 $^1\Pi$ states show large direct cross sections around 121.6 nm, they are still about one order of magnitude lower than the values given in the Leiden database. The lack of discrete bands around 122 nm is likely due to the limited number of states in the MRCI calculation and perhaps also due to the limited number of π orbitals included in the active space. While we were able to calculate electronic energies in this range for both $^1\Sigma$ and $^1\Pi$ states, the potential energy curves were not smooth and continuous. Therefore only direct photodissociation from lower excited states was calculated in the 122 nm energy range. Consequently, our cross sections are expected to be highly uncertain in the Ly-α region. In addition, it should be noted that the cross sections in the Leiden photodissociation database (Heays et al., 2017) are also highly uncertain in this same region, so additional work is needed to address the potential importance of CS photodissociation by Ly-α.

3.4. Conclusion

Here we have presented a detailed *ab initio* theoretical study of CS photodissociation from its ground electronic state using potential energy curves calculated with the MRCI+Q method with a custom basis set derived from aug-cc-pV(5+d)Z with additional diffuse functions. To improve the quality of the calculation for high-lying excited states, especially for the $B\,^1\Sigma^+$ and $C\,^1\Sigma^+$ states that have known strong predissociative bands from previous experiments, an expanded active space including more Rydberg MOs was used. Our calculation yields spectroscopic constants for the ground X and several low-lying excited electronic states in excellent agreement with experimental data.

Photodissociation cross sections were calculated using coupled-channel models for excited states from the *ab initio* calculation, considering both non-adiabatic and spin-orbit couplings. By combining these cross sections with the ISRF, CS photodissociation rates were derived at a variety of LTE temperatures along with the dominant atomic product channels. In space, the dominant photodissociation process for CS occurs through the $C - X$ transition followed by spin-orbit coupling to several $^3\Pi$ and $^3\Sigma^-$ states, yielding C atoms in the ground ^3P state and S atoms in the metastable ^1D state. Compared with other estimates of CS photodissociation, we obtain a rate that is a factor of 2.4 larger than that adopted by the Leiden database (Heays et al., 2017). Our rates are about a factor of 6 greater than those estimated in the recent calculation of Pattillo et al. (2018), arising from the fact that their choice of active space provided an inadequate treatment of Rydberg $^1\Sigma^+$ states that have strong transitions from the ground electronic state.

Finally, we would like to give an overall estimate of the accuracy of our results. The foundation of our photodissociation cross sections and rates is the PECs and TDMs obtained from the *ab initio* MRCI+Q calculation, which is highly reliable judged by all available spectroscopic data. Transition linewidths derived from the CSE calculation show that the $B - X$ and $C - X$ transitions can be considered completely dissociative in low-density environments where collisional relaxation is unavailable. Uncertainties in the magnitudes of the couplings between states may shift the calculated transition frequencies and linewidths somewhat; however, these factors should have a minimal effect on the total calculated cross sections, which are mainly determined by the TDMs and Franck-Condon factors. Previous studies of diatomic molecules have shown that cross sections derived from high-level *ab initio* calculations such as those employed here are generally accurate to within 20%. We have confidence that the cross sections calculated for the $B - X$ and $C - X$ bands have similar accuracy.

We found that the $C - X$ $(0 - 0)$ transition is responsible for 57% of the overall photodissociation of CS under the standard ISRF. This is not unexpected when compared with photodissociation of CO, as CS has a lower dissociation energy and a substantially higher density of electronic states allowing for ample opportunities for predissociation. While our transition frequencies differ from experimental values by about $200\,\mathrm{cm}^{-1}$, as long as the radiation field is smooth in the vicinity of 140 nm, our computed rates should be reliable. The atomic product branching fractions are more uncertain, as their values are sensitive to the exact methods used in the diabatization procedure. Future high-resolution spectroscopic measurements of the $B - X$ and $C - X$ bands, along with atomic branching ratios, would provide a good test for judging the ultimate accuracy of these calculations. They would also lead to improvements in the derived cross sections and rates because the experimentally-measured energy levels can be used to improve the diabatization and refine the *ab initio* PECs.

Nevertheless, our calculations still have some limitations. First, while we proved that several low-lying vibrational states of the B and C electronic states are totally predissociative, the same may not be true for higher vibrational states. Second, we are less confident in the accuracy of our electronic states at energies above the C state. In our model, the dominant contribution to the cross section below ~130 nm is direct photodissociation via the $^1\Sigma^+$ states. The direct photodissociation cross section in this region for the states included in our calculation should be reliable to ~20%, limited primarily by the accuracy of the TDMs. However, several higher $^1\Sigma^+$ and $^1\Pi$ states with energies below the Lyman limit exist and should also

contribute somewhat to the total photodissociation, though their transition dipole moments with the ground vibronic state are likely much smaller than the $C - X$ $(0 - 0)$ band. These states will likely make a significant contribution to the total cross section via direct photodissociation, and so our calculated cross section in this region should be taken as a lower limit. Although any predissociation from higher-energy states would make only a small contribution to the total photodissociation rate in a smooth radiation field (much less than 10%), previous experiments (Donovan et al., 1970) have indicated the presence of such a state near 121.6 nm. Because our *ab initio* data and CSE calculations do not cover this energy range adequately, we do not attempt to calculate the CS photodissociation rate by Lyman-α radiation, and this is an area in need of future investigation.

3.5. Appendix: Additional data and figures

To verify convergence, we calculated the potential energy at several points for a series of basis sets, including aug-cc-pVQZ, aug-cc-pV5Z, aug-cc-pV6Z, aug-cc-pV(Q+d)Z with Rydberg diffuse functions, and finally aug-cc-pV(5+d)Z with Rydberg diffuse functions, which was used for the final calculations in the present study. The exponents of the additional Rydberg diffuse functions are shown in Table 1. The potential energy curves of the X, A', B, C, and A states are shown in Fig 10 after subtracting the energy of the X state at $R = 1.542$ Å. Inclusion of additional Rydberg diffuse functions lowers the energy of the B state significantly. A maximum error of 0.08 eV can be estimated for the B state from the difference between calculations with aug-cc-pV6Z and aug-cc-pV(5+d)Z with Rydberg diffuse functions. The A', C, and A states are well converged.

The potential energy curves of all calculated states obtained from the SA-CASSCF/MRCI+Q calculations described in Section 3.2.1 are given in Table 3.7. Blank entries in the table indicate that the calculation did not converge at a particular value of R or that the state fell outside the range of those calculated for a particular symmetry. Among these 49 electronic states, the PECs of 21 states have already been shown in Figure 4.3, while the PECs of an additional 24 states are shown in Figure 3.11. The data for the remaining 4 states, $7\,^1\Sigma^+$, $3\,^1\Sigma^-$, $7\,^1\Pi$, and $4\,^3\Sigma^+$, are not shown, but the data are available in Table 3.7.

The absolute values of the transition dipole moments between $^1\Sigma^+$ and $^1\Pi$ states and the ground $X\,^1\Sigma^+$ state are shown in Table 3.8. Like Table 3.7, blank entries indicate convergence failure or that the particular

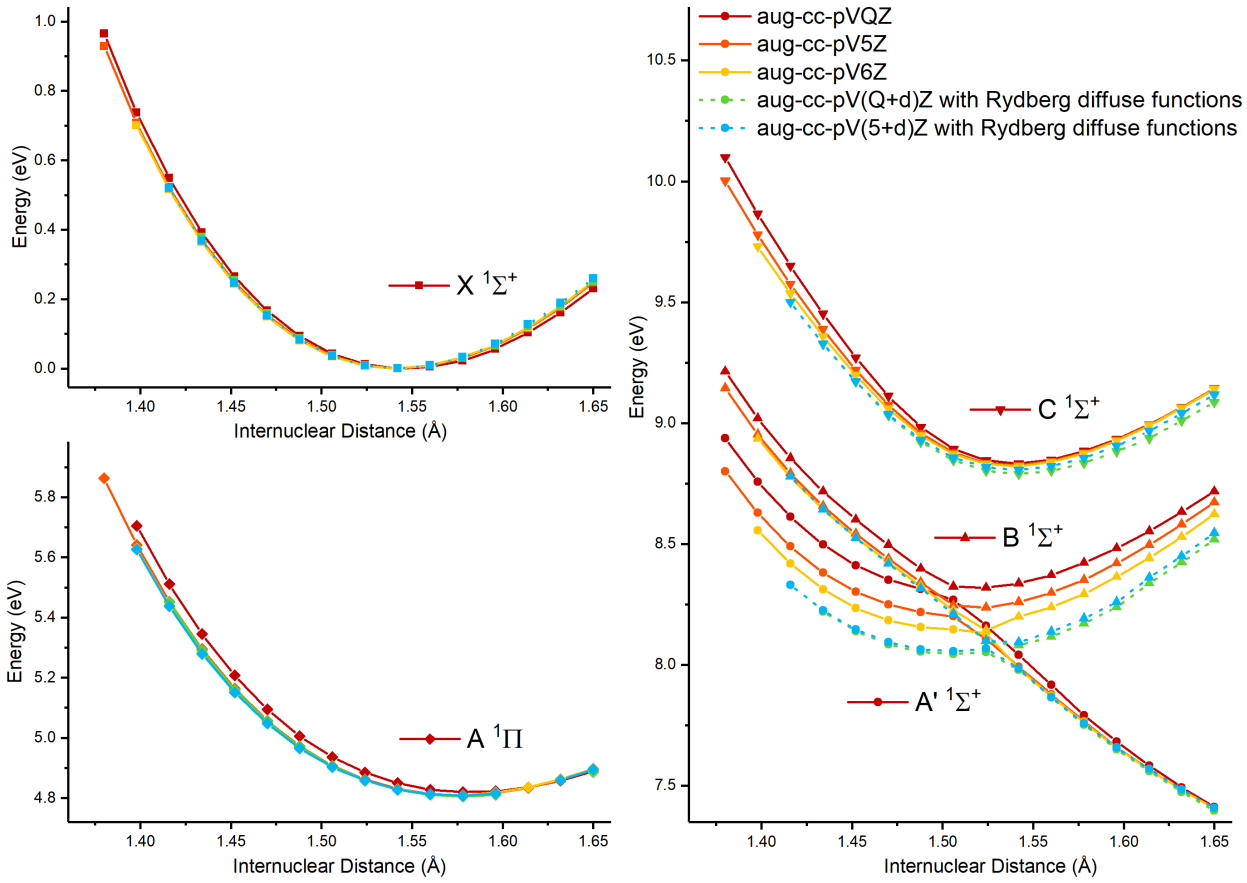

FIGURE 3.10. Potential energy curves of several states calculated with a series of basis sets

TABLE 3.7. MRCI+Q/aug-cc-pV(5+d)Z PECs for all electronic states of CS

R (Å)	$1\,^1\Sigma^+$	$2\,^1\Sigma^+$	$3\,^1\Sigma^+$	$4\,^1\Sigma^+$	$5\,^1\Sigma^+$	$6\,^1\Sigma^+$	$7\,^1\Sigma^+$	$1\,^1\Sigma^-$	⋯	$1\,^5\Delta$
0.7938	74.87140	78.93278	79.66499	80.30997	80.72843	80.83307	86.83185	⋯	⋯	⋯
0.8996	43.05554	48.49688	49.24178	50.00352	50.40615	53.09136	55.71249	⋯	⋯	59.76372
0.9261	⋯	⋯	⋯	⋯	⋯	⋯	⋯	⋯	⋯	53.68723
0.9525	31.91984	37.79983	38.51802	39.24516	39.51339	42.98093	44.81884	⋯	⋯	48.29292
⋮	⋮	⋮	⋮	⋮	⋮	⋮	⋮	⋮	⋮	⋮
7.6731	7.47457	7.48510	9.83764	9.85174	9.88433	⋯	⋯	7.48108	⋯	7.48958
7.9377	7.47481	7.48548	9.83861	9.85228	9.88486	⋯	⋯	7.48135	⋯	7.48967

a. PECs are in eV.
b. This table is available in its entirety in machine-readable format.

state was not calculated at the indicated R value. Additionally, the spin-orbit couplings between the $^1\Sigma^+$, $^3\Sigma^-$ and $^3\Pi$ states not already shown in Figure 4.11 are presented in Figure 3.12.

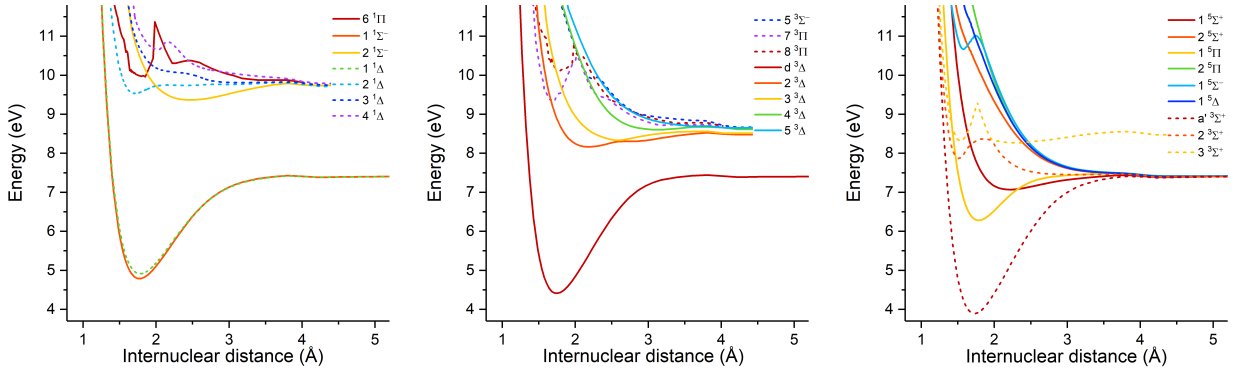

FIGURE 3.11. Potential energy curves of remaining electronic states of CS

TABLE 3.8. TDMs between $^1\Sigma^+$ and $^1\Pi$ states and the ground electronic state $X\,^1\Sigma^+$

R (Å)	$2\,^1\Sigma^+$	$3\,^1\Sigma^+$	$4\,^1\Sigma^+$	$5\,^1\Sigma^+$	$6\,^1\Sigma^+$	$7\,^1\Sigma^+$	$1\,^1\Sigma^-$	⋯	$7\,^1\Pi$
0.7938	0.86039	1.19859	0.36731	0.53697	0.08515	0.19403	0.30781	⋯	0.12908
0.8996	0.44859	0.83099	0.35651	0.75145	0.06795	0.42810	⋯	⋯	⋯
0.9525	0.34744	0.66844	0.26586	0.90374	0.08933	0.47362	⋯	⋯	⋯
1.0584	0.12811	0.63043	0.01976	0.81387	0.07418	0.52310	0.14462	⋯	0.40322
⋮	⋮	⋮	⋮	⋮	⋮	⋮	⋮	⋮	⋮
7.6731	0.00005	0.00000	0.00000	0.00000	⋯	⋯	0.00039	⋯	⋯
7.9377	0.00003	0.00000	0.00000	0.00000	⋯	⋯	0.00034	⋯	⋯

a. TDMs are in atomic units.
b. This table is available in its entirety in machine-readable format.

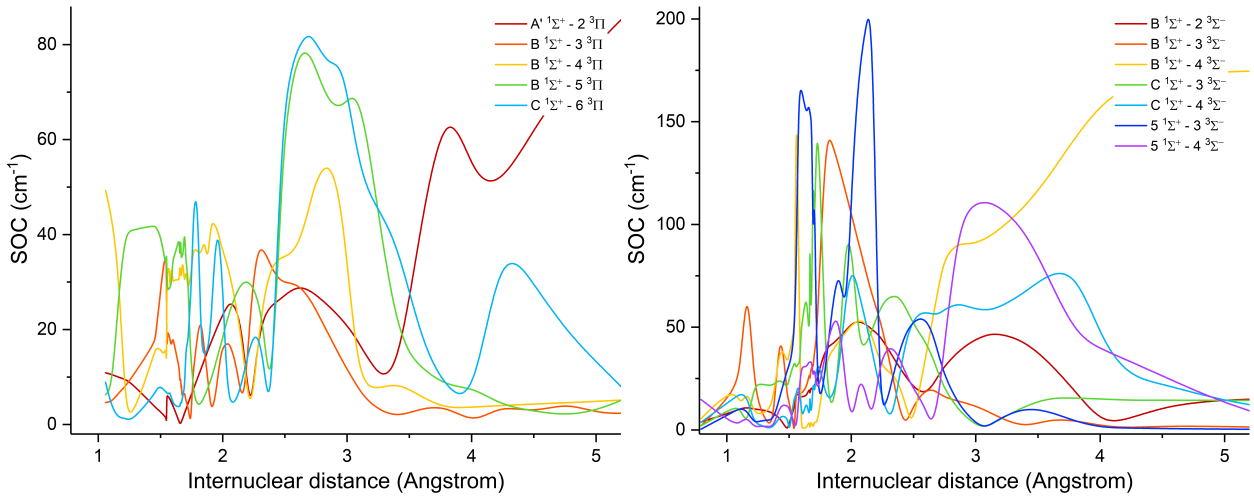

FIGURE 3.12. Several spin-orbit couplings between electronic states of CS

When calculating photodissociation cross sections for $^1\Pi$ states, we built a coupled-channel model to treat the $2\,^1\Pi$ and $3\,^1\Pi$ states. The interaction matrix is shown in Figure 3.13. We ignore any couplings involving $4\,^1\Pi$ and $5\,^1\Pi$ states as their interactions are subtle and non-obvious. This may introduce errors into cross section calculations in the energy range near these states.

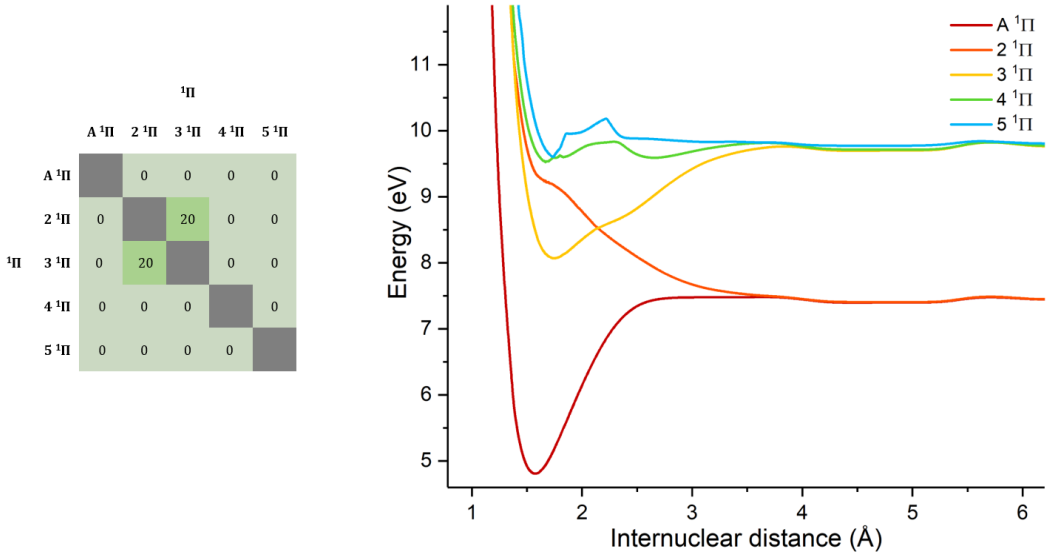

FIGURE 3.13. Coupled-channel model for the $^1\Pi$ diabatic states. Left: interaction matrix $V(R)$ off-diagonal elements, in cm^{-1}. Right: PECs of included diabatic states.

The TDMs were diabatized along with the PECs by exchanging the values on both sides of the crossing points, and are shown in Figure 3.14. Because diabatic PECs of the B and C states at longer internuclear distances were built by shifting PECs of the CS^+ X state, we manually reduce the TDMs of these two diabatic states to 0 in this region. As before, we ignored any couplings involving the $4\,^1\Pi$ and $5\,^1\Pi$ states. The wavefunction of the X ($v = 0, J = 0$) state is also plotted to indicate the Franck-Condon region. The diabatic PECs and corresponding TDMs used in the coupled-channel cross sections calculation are available in Table 3.9.

The rotationless cross sections of photodissociation from $X\,^1\Sigma^+$ $v'' = 0, 1$ are given in Tables 3.10 and 3.11. The calculation was performed with $1\,\mathrm{cm}^{-1}$ resolution between 59732 and $110000\,\mathrm{cm}^{-1}$, with additional points using smaller steps around several $B - X$ and $C - X$ transitions to better resolve the lineshapes near bound-bound transitions. Local thermodynamic equilibrium cross sections at various temperatures are

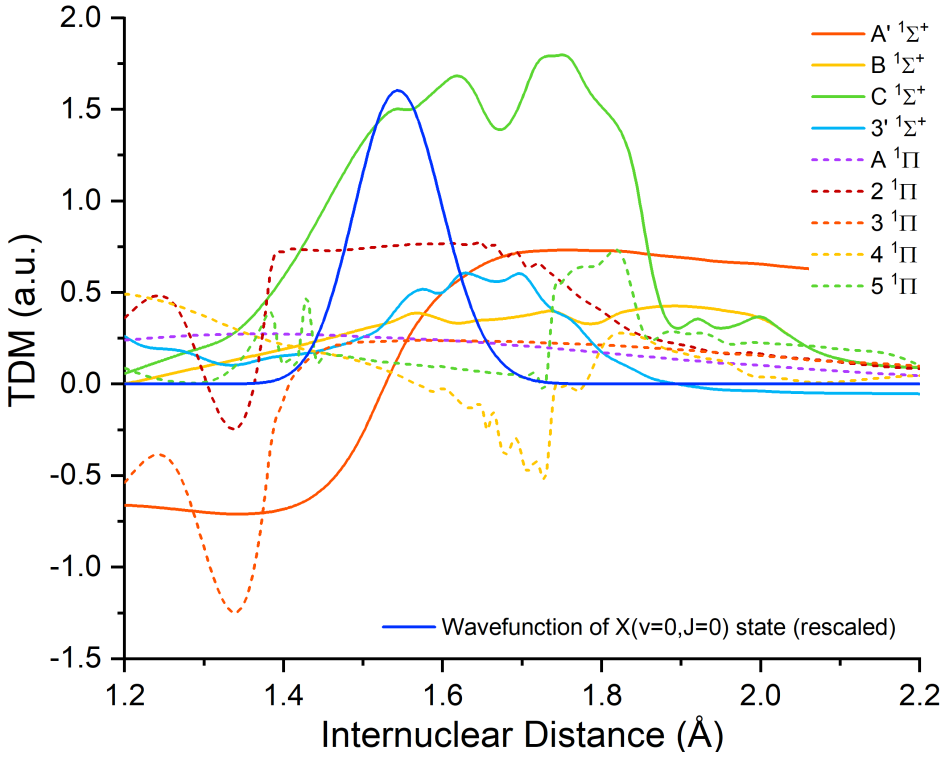

FIGURE 3.14. TDMs for diabatic states from the ground X state

TABLE 3.9. PECs and TDMs of diabatic model built for CS

R (Å)	pec-$X\,^1\Sigma^+$	pec-$A'\,^1\Sigma^+$	pec-$B\,^1\Sigma^+$	pec-$C\,^1\Sigma^+$	pec-$3'\,^1\Sigma^+$	pec-$2\,^3\Pi$	pec-$3\,^3\Pi$	$\cdots$	tdm-$5\,^1\Pi$
1.050	17.7367	24.8385	24.1887	25.8028	30.7668	30.6747	27.3703	$\cdots$	0.197
1.052	17.5116	24.6238	23.9754	25.5914	30.5403	30.4289	27.1524	$\cdots$	0.185
1.054	17.2886	24.4113	23.7642	25.3820	30.3157	30.1857	26.9367	$\cdots$	0.174
1.056	17.0677	24.2009	23.5552	25.1745	30.0930	29.9450	26.7230	$\cdots$	0.162
$\vdots$	$\vdots$	$\vdots$	$\vdots$	$\vdots$	$\vdots$	$\vdots$	$\vdots$	$\vdots$	$\vdots$
7.796	7.4748	7.4854	14.4318	15.1823	9.8381	7.4935	8.5675	$\cdots$	0.000
7.798	7.4748	7.4854	14.4318	15.1823	9.8381	7.4935	8.5675	$\cdots$	0.000

a. PECs are in eV.
b. TDMs are in atomic units.
c. This table is available in its entirety in machine-readable format.

shown in Table 3.12. These values were calculated using Equation 3.6 by summing over the photodissociation cross sections for the following rotational and vibrational levels the CS ground X state: $J'' = 0-53$ of $v'' = 0$, $J'' = 0-51$ of $v'' = 1$, and $J'' = 0-43$ of $v'' = 2$. These lower states were chosen so that

cross sections at temperatures up to 500 K can be derived accurately. Owing to the increased line density at elevated temperatures, the grid size for each temperature was adapted based on the peak positions. The final wavenumber grid is a collection of all the wavenumbers used. Cubic spline interpolation was used to generate estimated values at other small-step wavenumbers not explicitly calculated.

TABLE 3.10. Rotationless photodissociation cross sections from the $X\,^1\Sigma^+$ $v'' = 0$ level of CS

$\tilde{\nu}$ (cm^{-1})	All $^1\Sigma^+$	$1\,^1\Pi$	2 and $3\,^1\Pi$	$4\,^1\Pi$	$5\,^1\Pi$	Total
59732.000	3.51e-20	3.10e-25	1.79e-96	0.00e+00	0.00e+00	3.51e-20
59733.000	3.66e-20	4.12e-25	9.93e-97	0.00e+00	0.00e+00	3.66e-20
59734.000	3.28e-20	7.76e-26	7.44e-97	0.00e+00	0.00e+00	3.28e-20
59735.000	2.96e-20	3.20e-26	6.55e-97	0.00e+00	0.00e+00	2.96e-20
⋮	⋮	⋮	⋮	⋮	⋮	⋮
109998.000	1.75e-21	3.09e-25	3.21e-23	6.15e-22	6.38e-23	2.46e-21
109999.000	1.40e-21	3.08e-25	3.21e-23	6.16e-22	6.40e-23	2.11e-21

a. Cross sections are in cm^2.
b. This table is available in its entirety in machine-readable format.

TABLE 3.11. Rotationless photodissociation cross sections from the $X\,^1\Sigma^+$ $v'' = 1$ level of CS

$\tilde{\nu}$ (cm^{-1})	All $^1\Sigma^+$	$1\,^1\Pi$	2 and $3\,^1\Pi$	$4\,^1\Pi$	$5\,^1\Pi$	Total
59732.000	6.83e-18	1.40e-24	2.19e-71	0.00e+00	0.00e+00	6.83e-18
59733.000	6.83e-18	1.40e-24	2.25e-71	0.00e+00	0.00e+00	6.83e-18
59734.000	6.83e-18	1.40e-24	2.30e-71	0.00e+00	0.00e+00	6.83e-18
59735.000	6.83e-18	1.40e-24	2.36e-71	0.00e+00	0.00e+00	6.83e-18
⋮	⋮	⋮	⋮	⋮	⋮	⋮
109998.000	5.19e-21	2.72e-25	3.18e-23	4.67e-21	1.82e-21	1.17e-20
109999.000	5.19e-21	2.73e-25	3.18e-23	4.66e-21	1.82e-21	1.17e-20

a. Cross sections are in cm^2.
b. This table is available in its entirety in machine-readable format.

TABLE 3.12. LTE photodissociation cross sections for ground-state CS

$\tilde{\nu}$ (cm^{-1})	20 K	50 K	100 K	500 K
59732.000	1.17e-19	4.34e-19	6.71e-19	9.99e-19
59733.000	1.42e-19	4.95e-19	7.24e-19	1.02e-18
59734.000	1.78e-19	5.88e-19	8.10e-19	1.04e-18
59735.000	1.91e-19	6.18e-19	8.36e-19	1.05e-18
⋮	⋮	⋮	⋮	⋮
109998.000	2.28e-21	1.76e-21	1.40e-21	9.78e-22
109999.000	1.55e-21	1.13e-21	8.74e-22	5.53e-22

a. Cross sections are in cm^2.
b. This table is available in its entirety in machine-readable format.

CHAPTER 4

Theoretical study of excited Rydberg states of C_2

This chapter is based on the peer-reviewed journal article: Zhongxing Xu, S. R. Federman, William M. Jackson, Cheuk-Yiu Ng, Lee-Ping Wang, and Kyle N. Crabtree, "Theoretical study of excited Rydberg states of C_2", Journal of Physical Chemistry A, In preparation.

4.1. Introduction

C_2 is an important small molecule that is widely found in hydrocarbon combustion (Wollaston, 1802), comets (Donati, 1864), and astronomical environments (Lambert & Mallia, 1974; Sonnentrucker et al., 2007; Wehres et al., 2010). As a homonuclear diatomic molecule with no dipole-allowed rotational or vibrational transitions, observation of C_2 is accomplished via transitions among its electronic states. To date, 20 electronic states have been studied by spectroscopy, with a number of low-lying excited states being newly found in recent years (Kokkin et al., 2006; Krechkivska et al., 2015, 2017; McKemmish et al., 2020; Welsh et al., 2017). In the pasting 15 years, Schmidt and his colleagues have explored several new electronic states and vibrational states of C_2 both experimentally and theoretically (Schmidt, 2021). An overview of the electronic states of C_2 and its observed spectroscopic bands is shown in Figure 4.1.

Owing to its fundamental nature, C_2 has been the subject of a number of theoretical investigations. It is well known that the $X\,^1\Sigma_g^+$ ground state of C_2 has a multi-reference nature due to the quasi-degeneracy of the $2\,\sigma_u^*$, $1\,\pi_u$, and $3\,\sigma_g$ frontier molecular orbitals (MOs). This has even led to debate about whether the chemical bond in C_2 is better described as a double-π bond, as conventional MO theory predicts, or a quadruple bond on the basis of valence bond theory arguments (Shaik et al., 2017, 2012). The near-degeneracy of the frontier MOs is also responsible for the presence of an additional 7 low-lying excited electronic states with energies below 3 eV. In particular the first triplet $a\,^3\Pi_u$ state lies only 0.089 eV above the ground state, and allowed transitions among the low-lying triplet states (e.g., the Ballik-Ramsay $b\,^3\Sigma_g^- - a\,^3\Pi_u$ band, the Swan $d\,^3\Pi_g - a\,^3\Pi_u$ band, and the Duck $d\,^3\Pi_g - c\,^3\Sigma_u^+$ band), are readily observable

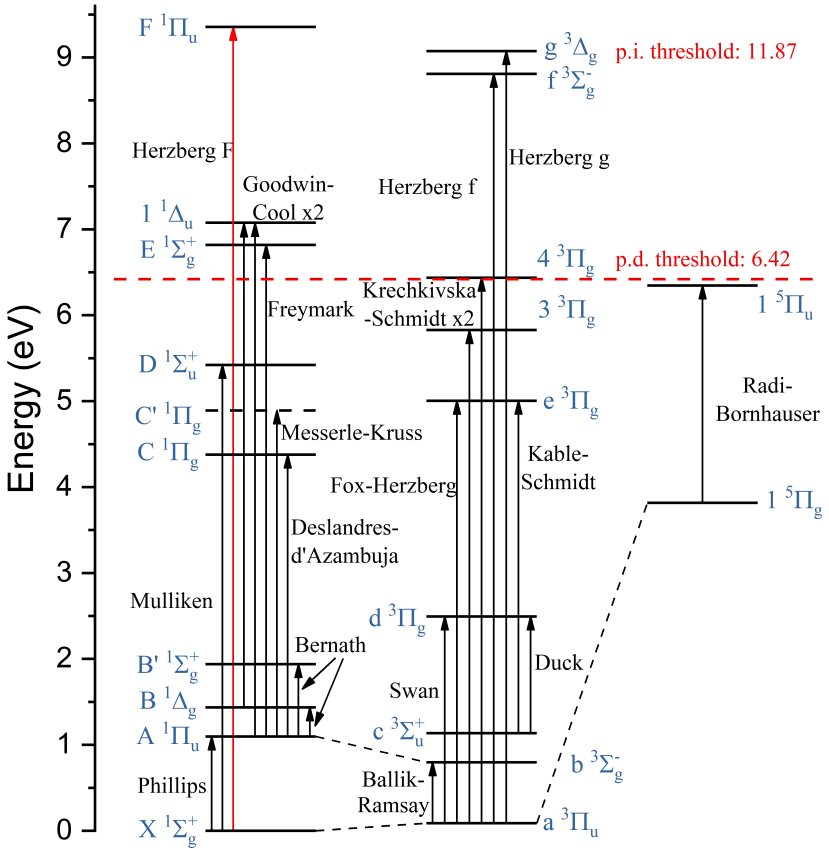

FIGURE 4.1. Electronic states and bands of C_2.

in the visible and near-infrared through absorption or fluorescence (Amiot et al., 1979; Joester et al., 2007; Phillips, 1948). The singlet manifold contains 3 low-lying excited states, and though the only allowed transition from the ground state is the near-infrared Phillips $A\,^1\Pi_u - X\,^1\Sigma_g^+$ band (Ballik & Ramsay, 1963), the $B\,^1\Delta_g$ and $B'\,^1\Sigma_g^+$ states have been observed via the Bernath bands arising from the $A\,^1\Pi_u$ state (Douay et al., 1988). Given the considerable quantity of experimental data available for comparison, these states have been well-characterized by theoretical calculations (Kokkin et al., 2007; Schmidt & Bacskay, 2007; Shi et al., 2011). A recent example is a detailed MRCI+Q/aug-cc-pCV5Z study of the the formation rate of C_2 in collisions of two carbon atoms, which involves all of these low-lying C_2 states (Babb et al., 2019).

There are two singlet states, three triplet states, and two quintet states below or around the photodissociation limit, which is 6.42 eV. The Mulliken $D\,^1\Sigma_u^+ - X\,^1\Sigma_g^+$ band has been well studied. Previous experiments (Blunt et al., 1995; Landsverk, 1939; Sorkhabi et al., 1997) and theoretical calculations (Schmidt

& Bacskay, 2007) found that the $D - X$ band favors the $\Delta v = 0$ sequence. The most recent study of the Mulliken band explored its $\Delta v = +2$ sequence involving higher vibrational levels of the D state up to μ =11 (Krechkivska et al., 2018). The $D - X$ $(0 - 0)$ band has been widely observed in space (Hupe et al., 2012). The Deslandres–d'Azambuja $C\,^1\Pi_g - A\,^1\Pi_u$ and Messerle-Kruss $C'\,^1\Pi_g - A\,^1\Pi_u$ bands were only observed in very early studies (Dieke & Lochte-Holtgreven, 1930; Herzberg & Sutton, 1940; Messerle & Krauss, 1967; Phillips, 1950). However, recent calculations suggested that the Messerle-Kruss band is actually a part of the Deslandres–d'Azambuja band (Schmidt, 2021), which is also verified by our calculation here. Among the three $^3\Pi_u$ states in this region, the $e\,^3\Pi_g$ state was discovered early (Fox & Herzberg, 1937; Phillips, 1949). The $3\,^3\Pi_g$ and $4\,^3\Pi_g$ states were found recently with the aid of theoretical calculations (Krechkivska et al., 2015, 2017). Experiments involving the quintet states are more challenging because the transition to quintet states from singlet or triplet states are forbidden. Bornhauser et al. (2015) used perturbation-facilitated optical-optical double resonance spectroscopy to observe the first transition $(1\,^5\Pi_u - 1\,^5\Pi_g)$ between quintet states. Another two singlet states $E\,^1\Sigma_g^+$ and $1\,^1\Delta_u$ lie in the UV region. The $E\,^1\Sigma_g^+$ state was detected through the $E\,^1\Sigma_g^+ - A\,^1\Pi_u$ band (Freymark, 1950), and the $1\,^1\Delta_u$ state through in the $1\,^1\Delta_u - B\,^1\Delta_g$ and the two photon $1\,^1\Delta_u - A\,^1\Pi_u$ bands using resonance-enhanced multiphoton ionization (REMPI) spectroscopy (Goodwin & Cool, 1988, 1989).

In space, C_2 was first detected in absorption through the (1-0) band of the Phillips $A - X$ system in the diffuse interstellar medium (ISM) toward Cyg. OB2 No. 12 (Souza & Lutz, 1977), and has since been observed in a wide variety of diffuse cloud sources (Lambert et al., 1995; Snow, 1978; Sonnentrucker et al., 2007). Because rotational emission is forbidden, the rotational levels of C_2 are metastable and their relative populations are used as a tracer for the local gas kinetic temperature (Snow & McCall, 2006). At the low temperatures of diffuse clouds C_2 is unreactive with both H and H_2, and photodissociation is suggested to be its key destruction pathway (Federman & Huntress, 1989). Among the states above the dissociation limit shown in Fig. 4.1 only the $F\,^1\Pi_u$ state is accessible from the ground $X\,^1\Sigma_g^+$ state, and because all C_2 in diffuse clouds is expected to be in the ground $X\,^1\Sigma_g^+$ state, the $F\,^1\Pi_u$ state is especially important for understanding the chemistry of C_2 in astronomical environments. In 2017, Welsh et al. (2017) found that the $v = 12$ level of the $e\,^3\Pi_g$ state has a reduced lifetime due to predissociation. However, the transition from the ground $X\,^1\Sigma_g^+$ state to the $e\,^3\Pi_g$ state is forbidden, thus the predissociation through $e\,^3\Pi_g$ is not likely to be a significant route to C_2 photodissociation in the ISM.

To date, the only laboratory spectroscopy of the $F - X$ transition was by Herzberg et al. (1969), where the $f\,^3\Sigma_g^- - a\,^3\Pi_u$, and $g\,^3\Delta_g - a\,^3\Pi_u$ bands were also detected in the 130–145 nm wavelength region. The derived spectroscopic constants suggested that the three upper states could be described as Rydberg states due to their similarity with those of low-lying electronic states of C_2^+. The $F - X$ transition has also been detected in ultraviolet spectra of several diffuse cloud lines of sight, yet a number of discrepancies in line positions and transition intensities remain unresolved (Hupe et al., 2012; Kaczmarczyk, 2000; Lambert et al., 1995; Sonnentrucker et al., 2007). Linewidths of transitions involving individual levels of the $F - X$ system are found to be broadened, confirming that the F state has a lifetime of only ~6 ps likely due to predissociation (Hupe et al., 2012).

From a theoretical standpoint, the most comprehensive treatment of C_2 states in the 7–10 eV region is a 2001 multireference configuration interaction (MRCI) study by Bruna & Grein (2001). Focusing specifically on the F state, they found that it is well-described as a $3s$ Rydberg state that correlates to the $1\,^2\Pi_u$ state of C_2^+; i.e., the configuration is $\sigma_u^2\pi_u^3 3s$ or $[^2\Pi_u, 3s]$. The (0,0) band within the Herzberg $F - X$ system was calculated to have an oscillator strength $f_{00} = 0.098$, which was in good agreement with a value of $f_{00} = 0.10 \pm 0.01$ inferred from astronomical observations (Lambert et al., 1995). This oscillator strength is the calculated to be the largest among all known electronic transitions of C_2, being larger by nearly a factor of 2 compared with the $D - X$ Mulliken system. The adiabatic potential energy curve (PEC) of the $F\,^1\Pi_u$ state features non-adiabatic interactions with the $3\,^1\Pi_u$ and $4\,^1\Pi_u$ states which cause it to support only three bound vibrational states, two of which have been observed in astronomical spectra (Hupe et al., 2012). Bruna & Grein (2001) estimated a radiative lifetime of ~3 ns for the $F\,^1\Pi_u$ state, which is much longer than the inferred lifetime from the aforementioned linewidth measurements. However, they did not explore potential predissociation mechanisms. Also, their calculation only included excited states which can be reached via absorption from either $X\,^1\Sigma_g^+$ state or $a\,^3\Pi_u$ state into their calculation. The $^3\Sigma_u^+$ and $^3\Sigma_u^-$ states were not investigated, although those states can be involved in predissociation of the F state through spin-orbit couplings.

Estimates of the photodissociation cross section of C_2 in the Leiden photodissociation and photoionization database (Heays et al., 2017) are based on MRCI calculations from the mid-1980s (Pouilly et al., 1983) . Despite great efforts, their computations were severely limited by available computational power at the time. The calculated electronic energy T_e of the $F\,^1\Pi_u$ state was too large by ~0.8 eV and the calculated oscillator

strength for the origin band was only $f_{00} = 0.02$, in considerable disagreement with more recent estimates. These discrepancies, together with the many new astronomical observations since Bruna & Grein (2001), call for a new detailed high-level quantum chemical study.

Recently, we have investigated the photodissociation of CS through high-energy Rydberg states using *ab initio* multireference configuration interaction (MRCI) methods with a reference space generated by the complete active space self-consistent field (CASSCF) technique (Xu et al., 2019). By including several Rydberg molecular orbitals into the active space of the CASSCF reference and adding extra diffuse functions to the basis set, the adiabatic PECs of several Rydberg states were obtained successfully. Photodissociation cross sections were then derived by constructing a coupled system of diabatized states, including non-adiabatic and spin-orbit couplings, and solving the coupled-channel radial Schrödinger equation.

Here, we employ similar methods to study the photodissociation of C_2 with a particular focus on the $F\,^1\Pi_u$ state and the $F - X$ electronic transition. To this end, we have computed the PECs of 57 electronic states, and we explore their potential interactions involving the F state. The paper is organized as follows. Details of our theoretical methods are introduced in Section 4.2. The results from *ab initio* calculations are presented in Section 4.3, along with a discussion of the coupled-channel model and computed photodissociation cross sections and rates are discussed. Finally, a summary of work and future perspectives are given in Section 4.4.

4.2. Theory and Calculations

4.2.1. Ab initio calculation.

Electronic structure calculations were performed using the MOLPRO 2019.1 quantum chemistry software package (H.-J. Werner & P. J. Knowles, 2015; Werner et al., 2012). Initial electronic states were calculated by the dynamically weighted state-averaged complete active space self-consistent field (DW-SA-CASSCF) method, yielding optimized MOs and configuration state functions (Knowles & Werner, 1985; Werner & Knowles, 1985). Dynamic electron correlation was then treated by use of internally contracted multireference configuration interaction with single and double excitations from a subset of the DW-SA-CASSCF optimized configurations, and the Davidson correction was included in the energy calculations (MRCI+Q) (Knowles & Werner, 1988, 1992; Werner & Knowles, 1988). PECs were generated from a total of 268 single point calculations spanning internuclear distances from 0.8 Å to 15.0 Å. In the bonding region, the points were

typically spaced by 0.005 Å, but in some areas near avoided crossings a smaller grid spacing of 0.001 Å or 0.002 Å was employed.

The full point group of C_2 is $D_{\infty h}$, which cannot be calculated directly in MOLPRO. Calculations are done at D_{2h} symmetry, which is the largest Abelian subgroup of $D_{\infty h}$. The irreducible representations of $D_{\infty h}$ up to Δ map onto those of D_{2h} as follows:

$$
\begin{aligned}
&\Sigma_g^+ \rightarrow A_g, && \Sigma_u^+ \rightarrow B_{1u} \\
&\Sigma_g^- \rightarrow B_{1g}, && \Sigma_u^- \rightarrow A_u \\
&\Pi_g \rightarrow (B_{2g}, B_{3g}), && \Pi_u \rightarrow (B_{3u}, B_{2u}) \\
&\Delta_g \rightarrow (A_g, B_{1g}), && \Delta_u \rightarrow (B_{1u}, A_u)
\end{aligned}
\tag{4.1}
$$

Here, when referring to the number of orbitals or states of each symmetry in D_{2h}, we will list them in the order (a_g, b_{3u}, b_{2u}, b_{1g}, b_{1u}, b_{2g}, b_{3g}, a_u) consistent with the MOLPRO convention.

For these calculations, Dunning's augmented correlation consistent polarized valence quintuple-zeta Gaussian basis set (aug-cc-pV5Z or aV5Z) (Dunning, 1989; Kendall et al., 1992) was used with the addition of 2 additional s-type and 2 additional p-type diffuse atomic orbitals per atom. The final basis set we used can therefore be designated as aug-cc-pV5Z-2s2p or aV5Z-2s2p. The extra orbitals are even tempered ratio of 2.5 with exponents 0.01576 and 0.006304 for s-type orbitals and 0.01088 and 0.004352 for p-type ones. As discussed later, the additional diffuse functions are important for obtaining accurate electronic energies for Rydberg states. In total, the basis set comprises 270 orbitals, with (50,33,33,19,50,33,33,19) symmetry-adapted functions in D_{2h}. Tests were also performed using additional Dunning's augmented core-valence basis sets aug-cc-pCV5Z and aug-cc-pCV6Z (Dunning, 1989; Kendall et al., 1992); as expected, for Rydberg states these basis sets had minimal effect on the calculated energy but increased the calculation time by a factor of about 2.5.

The choice of active space is critical for excited state calculations. For the ground state and low-lying electronic states, use of the valence MOs as active space is generally sufficient, but a more careful selection must be made for high-energy and Rydberg states. As mentioned previously, the experimental spectroscopy (Herzberg et al., 1969) and earlier theoretical calculations (Bruna & Grein, 2001) have shown that the F state is a Rydberg state with the configuration $\sigma_u^2\pi_u^3 3s\,[1^2\Pi_u, 3s]$, suggesting that inclusion of the $4a_g$ orbital into the active space is necessary for accurate treatment of static electron correlation in the

F state (see Figure 4.2). After exploratory calculations, we also added the $5a_g$, $6a_g$, and $7a_g$ MOs into the active space to achieve smooth PECs over the entire range of internuclear distances. Our final CAS (8,12) active space contains 12 total MOs (7,1,1,0,3,1,1,0) and 8 valence electrons; the lowest two core MOs (1,0,0,0,1,0,0,0) are closed and doubly-occupied. Rydberg states with 3s, 3d, and potentially 4s Rydberg orbitals are able to be well calculated in our study, while any Rydberg states with a 3p Rydberg orbital are absent in our results. Though it is possible for states with 3p Rydberg orbital to be $^1\Sigma_u^+$ or $^1\Pi_u$ states, near the equilibrium geometry of the $F\,^1\Pi_u$ state they are unlikely to contribute to the electronic character owing to their higher energies.

The DW-SA-CASSCF procedure was used to optimize the orbital shapes and establish the reference functions for the subsequent MRCI+Q calculations. SA-CASSCF involves optimizing orbitals by minimizing the average energy of a set of electronic states with a specified spin multiplicity and symmetry, and has been found to yield smooth PECs for both the ground electronic state and excited states at the same time. For internuclear distances below 3.2 Å, (15,10,10,7,5,6,6,4), (8,13,13,11,14,9,9,12), and (3,1,1,4,1,3,3,3) singlet, triplet, and quintet states were averaged, respectively, and for larger internuclear distances, (11,5,5,5,3,5,5,5), (4,7,7,6,7,7,7,6), and (4,2,2,1,1,2,2,1) states were averaged. The set of states for internuclear distance larger than 3.0 Å correspond to the 6 atomic limits $^3P + {}^3P$ (defined as E=0), $^3P + {}^1D$, $^1D + {}^1D$, $^3P + {}^1S$, $^1D + {}^1S$, $^3P + {}^5S$ (E=0.154 Hartree). The diabatic F state converges to the $^3P + {}^3P^o$ limit theoretically, which lies at E =0.275 Hartree. The selection of states at shorter internuclear distance depends on the SA-MCSCF energy at R =1.25 Å. All states with an energy within 0.50 Hartree (91.2 nm, 13.6 eV) of the ground X state are included. For states with $^1\Sigma_g^+$, $^1\Pi_u$, $^3\Pi_u$, $^3\Sigma_u^+$ and $^3\Sigma_u^-$ symmetry, the thresholds are set to 0.60 Hartree. The calculations around 3.2 Å using both sets of averaged states differ by only ~10 cm^{-1}. After including such a large number of states in the SA-CASSCF calculation, the ground electronic state may not be well-optimized if all states have equal weights in the optimization process. In the dynamically weighted state-averaged method (Deskevich et al., 2004), the weight for each desired state $W(x)$ varies dynamically based on the formula:

$$W(x) = \mathrm{sech}^2(\beta(E_x - E_0)), \tag{4.2}$$

where E_x and E_0 are the energy of each desired state and ground state, and β is a parameter to control how fast the weight decreases as the energy increases. DW-SA-CASSCF has been applied in several quantum

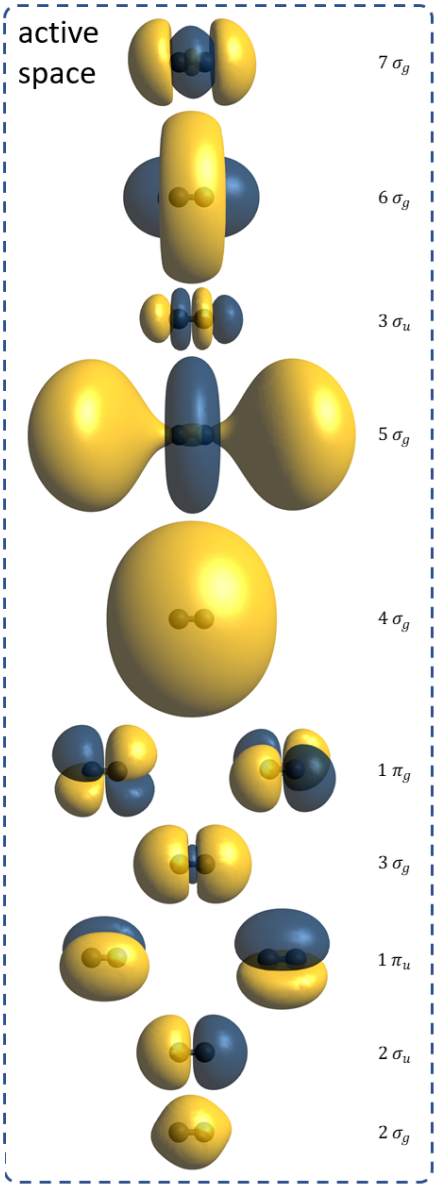

FIGURE 4.2. Molecular orbitals (MOs) in the active space of C_2 optimized at R =1.25 Å, plotted with isosurface value 0.01. The MOs are generated by a DW-SA-CASSCF calculation with details described in the text except that h-type orbitals are removed from basis set.

chemical calculations involving excited states (Dawes et al., 2010; Samanta et al., 2014). Here, we choose $\beta = 3.0\,\text{Hartree}^{-1}$; an excited state at 75,000 cm^{-1} therefore has a weight of about 40% compared to the

ground state. The DW-SA-CASSCF MOs at an internuclear distance of 1.25 Å are shown in Figure 4.2. As the internuclear distance increases, the shapes and energy ordering of the MOs change significantly.

The configuration state functions generated in the DW-SA-CASSCF procedure are used to generate the reference space in the following MRCI+Q calculations. For the calculation of the $^1\Pi_u$ states, there are 4,060 configuration state functions (CSFs) in our reference space. From the reference space, a total of 4,563,905 contracted CSFs formed from 91,843,656 uncontracted CSFs are included in the MRCI calculations. PECs are computed with the Davidson correction added, and the transition dipole moments (TDMs) for allowed transitions from the ground X state are evaluated from the MRCI wavefunctions. Additionally, to study the perturbations and predissociation of the $F\,^1\Pi_u$ state, spin-orbit couplings (SOCs) and non-adiabatic coupling matrix elements (NACMEs) involving the F states are also calculated using the MRCI wavefunctions. The full Breit-Pauli operator is used to calculate the SOC matrix elements between internal configurations and a mean-field one-electron Fock operator is applied to calculate the contribution of external configurations. The NACMEs are calculated by finite differences of the MRCI wavefunctions at ΔR = +0.001 Å.

To further explore the Rydberg nature of F state, we calculated PECs for the two lowest $^2\Pi_u$ electronic states of C_2^+ using a valence CAS(7,8) active space and the same basis set. Finally, for the ground state and most low-lying excited states, spectroscopic constants, including T_e, ω_e, $\omega_e x_e$, B_e, D_e and α_e, were calculated by fitting the rovibrational energy levels derived from a numerical evaluation of the one-dimensional Schrödinger equation using the DUO package (Yurchenko et al., 2016). The dissociation limits D_e are calculated as the energy difference of corresponding atomic limits and the potential well minimum.

4.2.2. Photodissociation cross sections and photodissociation rates.

We apply the coupled-channel Schrödinger equation (CSE) technique to study the predissociation mechanics of C_2 states, focusing on the $F\,^1\Pi_u$ state. This method was adapted from scattering theory (Mies, 1980) and has been detailed by van Dishoeck et al. (1984) and Heays et al. (2010). The CSE method has been used to study the photodissociation of many diatomic molecules, including OH (van Dishoeck et al., 1984), O_2 (Gibson & Lewis, 1996; Lewis et al., 2001), N_2 (Heays et al., 2015), and S_2 (Lewis et al., 2018). In those studies, coupled-channel models of states contributing to predissociation are built using a basis of diabatic states. Then, least-squares fitting programs are used to optimize the model parameters, which include potential energy curves, transition dipole moments and couplings between states, to match the calculated cross sections to experimentally measured cross sections and linewidths. We successfully employed

this method, using *ab initio* model parameters computed at the MRCI level to study the predissociation of CS $^1\Sigma^+$ states (Xu et al., 2019).

In the CSE method, the coupled-channel wavefunctions $\psi_i(r, R, \theta, \phi)$ can be treated as a linear combination of N_T diabatic electronic and nuclear wavefunctions:

$$\psi_i(r, R, \theta, \phi) = \sum_{j=1}^{N_T} \frac{1}{R} \chi_{ij}(R) \phi_j(r; R) \Theta_j(\theta, \phi), \tag{4.3}$$

where the $\chi_{ij}(R)$ are R-dependent expansion coefficients of the electronic-rotational basis states $\phi(r; R)\Theta(\theta, \phi)$. Then the coupled Schrödinger equation in matrix format

$$\frac{d^2}{dR^2}\boldsymbol{\chi}(R) = -\frac{2\mu}{\hbar^2}\boldsymbol{\chi}(R)[E\mathbf{I} - \mathbf{V}(R)]. \tag{4.4}$$

is solved numerically to obtain the set of expansion coefficients $\chi_{ij}(R)$ at a given energy E. $\mathbf{I}$ is identity matrix, μ is the molecular reduced mass, and $\mathbf{V}(R)$ is the interaction matrix with potential energy curves of diabatic basis states as diagonal elements and the couplings among them as off-diagonal elements, including electrostatic, rotational, and spin-orbit interactions. The total photoabsorption cross section from an uncoupled lower state j to an upper state i can be calculated as

$$\sigma_{ij}(v) = \frac{\pi\tilde{\nu}}{3\hbar\epsilon_0} \left| \sum_k^{N_T} \left(\int \chi_{ik}^{\dagger}(R) R_{kj}^e(R) \chi_j(R)\, dR \cdot S^{1/2}_{J_k J_j \Omega_k \Omega_j} \right) \right|^2, \tag{4.5}$$

where R_{kj}^e is the electric transition dipole moments between states j and i, $\tilde{\nu}$ is the photon wavenumber, and $S_{J_k J_j \Omega_k \Omega_j}$ is the corresponding Hönl-London factor. Assuming the photodissociation efficiency of an open channel state is unity, summing over all open-channel cross sections gives the total photodissociation cross section:

$$\sigma_j(v) = \sum_{i=1}^{N_O} \sigma_{ij}(v), \tag{4.6}$$

where N_O is number of open channels. This assumption can be verified by comparing the predissociation lifetime derived from the calculated linewidth with the spontaneous emission lifetime.

The photodissociation rate of a molecule in a UV radiation field can be calculated as

$$k = \int \sigma(\lambda) I(\lambda) d\lambda \tag{4.7}$$

where $\sigma(\lambda)$ is the photodissociation cross section including both direct photodissociation and predissociation and $I(\lambda)$ is the radiation intensity of the radiation field. We compute the photodissociation rate of C_2 from its ground (X) state with $(v'', J'') = (0, 0)$ in the standard interstellar radiation field (ISRF) (Draine, 1978) and several other radiation fields.

4.3. Results and Discussion

4.3.1. PECs.

We have successfully calculated the PECs of 57 states in total, some of the which only have PECs available in a specific range of internuclear distances. The PECs of states which will be discussed in this work are shown in Figure 4.3, while the PECs of other singlet, triplet, and quintet states are shown in Figure 4.4. To estimate the accuracy of our calculations, a comparison between the calculated spectroscopic constants and a selection of experimental values is shown in Table 4.1. Experimental spectra show abundant perturbations among excited states of C_2, so the polynomial fitted basic spectroscopic constants cannot fully reproduce the experimental spectra. The spectroscopic constants shown here only provide a description of the shapes of calculated adiabatic potential energy curves. We will first discuss about experimentally known states, followed by a brief discussion of other states. Quintet states are not important for the photodissociation of C_2 in space, thus they will not be considered further here.

The 11 low-lying states of C_2 primarily involve the molecular orbitals $2\sigma_u$, $1\pi_u$, and $3\sigma_g$. Based on the orbital energies calculated at DW-SA-CASSCF at $R = 1.25$ Å, the $3\sigma_g$ orbital is only 0.63 eV higher than the $1\pi_u$ orbitals, while $1\pi_u$ is about 3.52 eV higher than the $2\sigma_u$ orbital. Keeping the core $1\sigma_g$ and $1\sigma_u$ orbitals, and the first valence orbital $2\sigma_g$ doubly-occupied, these low lying electronic states arise from configurations with 6 electrons distributed among the $2\sigma_u$, $1\pi_u$, and $3\sigma_g$ orbitals. The 11 states coming from these 6 configurations are listed in Table 4.2. It is well known that the ground X state of C_2 has a multi-reference nature. The $2\sigma_u^2\, 1\pi_u^4\, 3\sigma_g^0$ in table is only the dominant configuration around the potential minimum. The other states near the photodissociation threshold, including $1\,^1\Delta_u$, $e\,^3\Pi_g$, $e\,^3\Pi_g$ and $e\,^3\Pi_g$, have equilibrium distances much longer than the ground X state, thus the dominant configurations are more complicated. Few studies have been done on the remaining three excited states. The $F\,^1\Pi_u$ state has been suggested as a Rydberg state corresponding to $1\pi_u \rightarrow 3s$ in several previous studies (Bruna & Grein, 2001;

Pouilly et al., 1983). Bruna & Grein (2001) found that $f\,^3\Sigma_g^-$ is a mixed valence-Rydberg state while $g\,^3\Delta_g$ is a valence state.

For the low-lying electronic states, thousands of high-resolution rovibronic lines have been recorded. Using those transitions, Chen et al. (2015) determined the energy difference between the ground $X\,^1\Sigma_g^+$ and $a\,^3\Pi_u$ states to be 720.008(2) cm^{-1} and derived updated spectroscopic constants for $X\,^1\Sigma_g^+$, $A\,^1\Pi_u$, $a\,^3\Pi_u$ and $b\,^3\Sigma_g^-$ states. Because our calculation averages many electronic states in the CASSCF procedure to treat high-energy states, it is reasonable that the accuracy for low-lying states is diminished relative to calculations focusing only on those states. Nevertheless, our calculation still shows good agreement with the available experimental data. The X state is deeply bound with a dissociation limit D_e 6.2707eV. The calculated vibrational constant ω_e is 1844.178 cm^{-1}, which is about 11 cm^{-1} smaller than the experimental value. The $a\,^3\Pi_u$ state is only 581.232 cm^{-1} higher than the ground X state in our calculation, which is about 140 cm^{-1} smaller than the experimental value derived by Chen et al. (2015). Despite the electronic energy difference, the harmonic vibrational constants of the $X\,^1\Sigma_g^+$ and $a\,^3\Pi_u$ states calculated by our method are quite close to the experimental values.

The singlet states $A\,^1\Pi_u$, $B\,^1\Delta_g$, and $B'\,^1\Sigma_g^+$ have deep potential wells and converge to the $^3P + {}^3P$ atomic limit. Compared with their recently updated spectroscopic constants(Chen et al., 2015, 2016), the T_e values of these three states have been underestimated by our calculation by ~300-500 cm^{-1}, while the vibrational constants are similar ($|\Delta\omega_e| < 15\,\mathrm{cm}^{-1}$). Another three singlet states $C\,^1\Pi_g$, $D\,^1\Sigma_u^+$, and $E\,^1\Sigma_g^+$ involve exciting electrons from the $2\sigma_u$ orbital to the $1\pi_u$ and $3\sigma_g$ orbitals. All have a potential minimum near R = 1.25 Å, similar to the ground $X\,^1\Sigma_g^+$ state, and much smaller than those of A,B, and B' states, which are beyond 1.3 Å. Because the $2\sigma_u$ orbital is an anti-bonding orbital, removing electrons would not be expected to decrease the bond order nor weaken the bond strength significantly. For similar reasons, the vibrational constants of these three states are significantly larger than those of A, B, and B' states. The $C\,^1\Pi_g$ state has a notable avoided crossing with $2\,^1\Pi_g$. The adiabatic $D\,^1\Sigma_u^+$ state has an avoided crossing with the adiabatic $2\,^1\Sigma_u^+$ state at R = 1.75 Å. From the shape of the two adiabatic curves, the diabatic $2\,^1\Sigma_u^+$ state in this region has potential well around R = 1.90 Å, which is very close to the avoided crossing point. The large difference in equilibrium bond length between this adiabatic state and the ground $X\,^1\Sigma_g^+$ state indicates the Frank-Condon factors for the vibronic transitions between them would likely be too low to play an important role in the photodissociation of C_2.

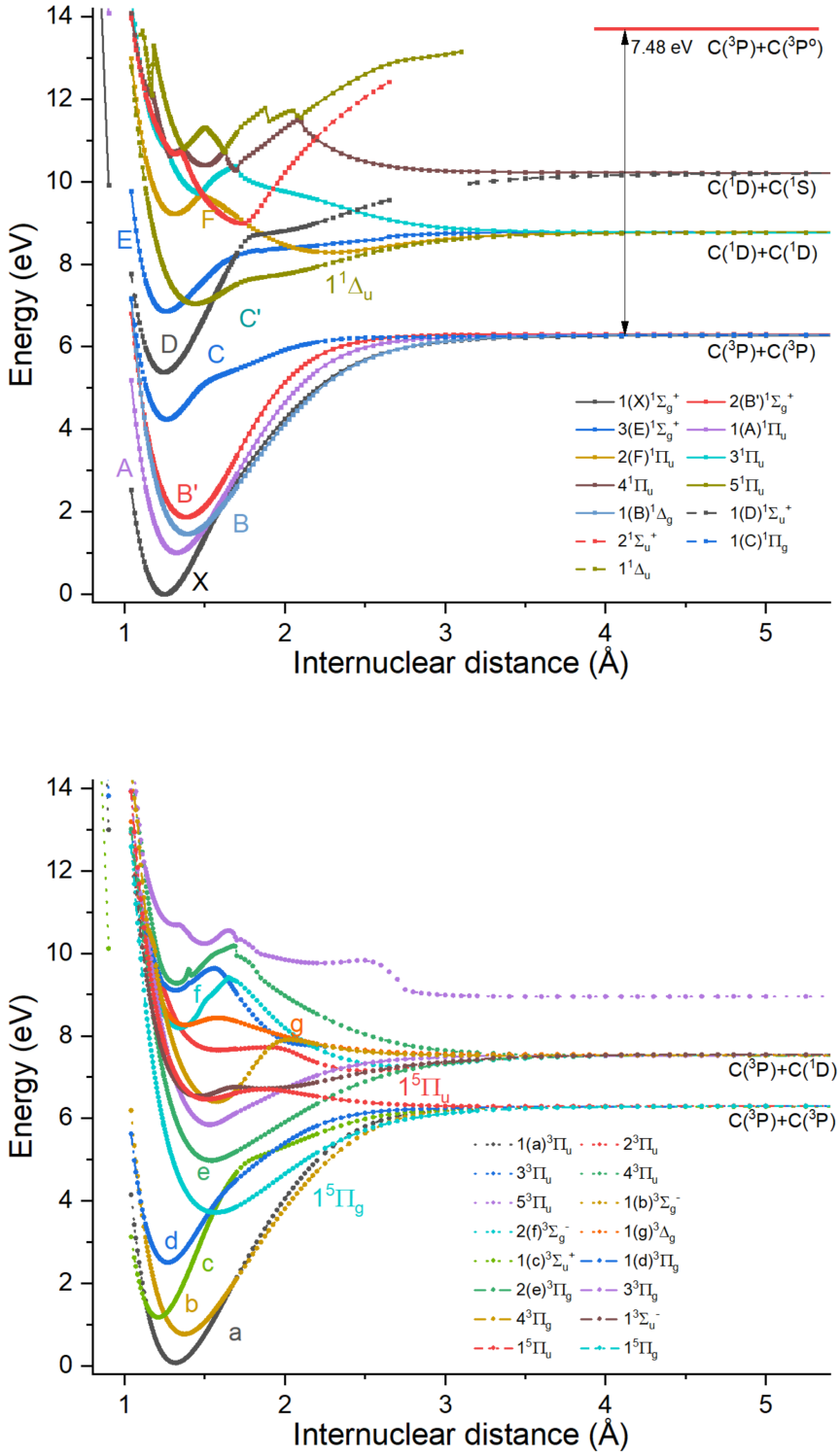

FIGURE 4.3. MRCI+Q PECs of several states of C_2, including all experimentally studied states and several $^1\Pi_u$ and $^3\Pi_u$ states.

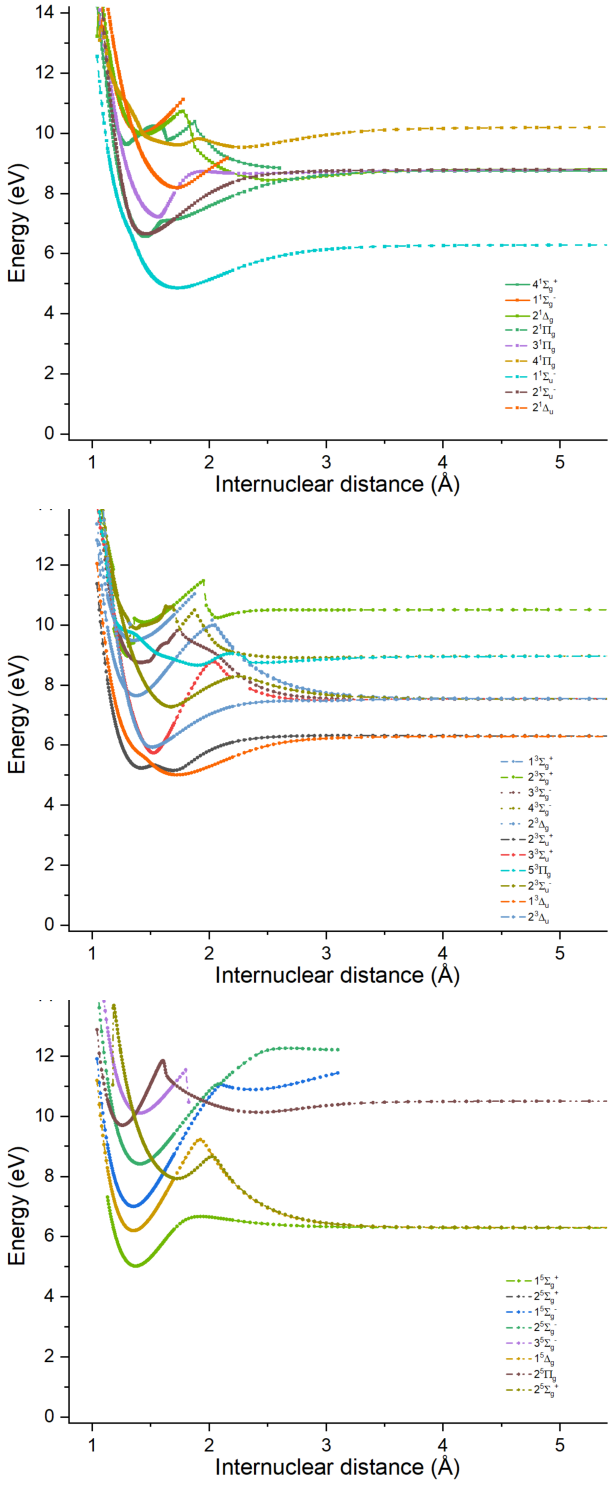

FIGURE 4.4. PECs of remaining singlet, triplet, and quintet states of C_2

TABLE 4.1. Spectroscopic constants for several low-lying and highly excited states in cm^{-1} of C_2, along with equilibrium bond lengths in Å and dissociation limits in eV.-

	Method	T_e (cm^{-1})	ω_e (cm^{-1})	$\omega_e x_e$ (cm^{-1})	$\omega_e y_e$ (cm^{-1})	B_e (cm^{-1})	D_e ($10^{-6} cm^{-1}$)	α_e (cm^{-1})	r_e (Å)	D_e (eV)
$X\,^1\Sigma_g^+$	This work	0	1844.178	12.553	−0.358	1.81281	6.944	0.02205	1.2449	6.2707
	Expt[a]	0	1855.035	13.570	−0.127	1.82005	6.972	0.01790		
$A\,^1\Pi_u$	This work	8115.177	1594.881	11.425	−0.06	1.60703	6.505	0.01762	1.3222	5.2873
	Expt[a]	8391.406	1608.217	12.078	−0.003	1.61660	6.505	0.01693		
$B\,^1\Delta_g$	This work	11795.780	1398.345	11.477	0.015	1.45411	6.307	0.01682	1.3900	4.8285
	Expt[b]	12082.343	1407.451	11.471	0.009	1.46367	6.306	0.01681		
$B'\,^1\Sigma_g^+$	This work	15083.953	1409.625	−2.306	−0.413	1.47361	6.263	0.01084	1.3808	4.4286
	Expt[b]	15410.33	1420.36			1.47967	6.785	0.00943		
$C\,^1\Pi_g$	This work	34221.241	1762.866	1.173	−7.89	1.76747	7.092	0.05462	1.2608	2.0506
$D\,^1\Sigma_u^+$	This work	43416.653	1810.257	14.616	-0.005	1.81134	7.320	0.01949	1.2454	4.8294
	Expt[c]	42315.83	1829.905	14.089	0.001	1.83254		0.01909		
$E\,^1\Sigma_g^+$	This work	55297.535	1663.568	43.806	0.531	1.77829	8.439	0.06309	1.2570	1.9187
$1\,^1\Delta_u$	This work	56842.617	1089.398	−14.306	−7.302	1.35977	7.964	0.04574	1.4374	1.7329
$a\,^3\Pi_u$	This work	581.232	1629.966	11.693	0.001	1.62586	6.425	0.01726	1.3146	6.2253
	Expt[a]	720.008	1641.326	11.649	−0.002	1.63231	6.448	0.01654		
$b\,^3\Sigma_g^-$	This work	6211.833	1459.059	10.865	−0.018	1.49223	6.205	0.01674	1.3722	5.5225
	Expt[a]	6439.083	1470.365	11.135	0.010	1.49866	6.221	0.01629		
$c\,^3\Sigma_u^+$	This work	9466.486	2048.183	12.414	−0.328	1.91621	6.736	0.02005	1.2109	5.1102
	Expt[d]	8662.925[e]	2061.940	14.836		1.9319		0.01855		
$d\,^3\Pi_g$	This work	20207.845	1766.732	12.560	−1.117	1.74613	6.777	0.02988	1.2685	3.7920
$e\,^3\Pi_g$	This work	40142.394	1100.606	29.400	0.771	1.18297	5.737	0.02163	1.5411	2.5459
$3\,^3\Pi_g$	This work	47149.632	1319.834	79.582	3.777	1.20085	4.665	0.02861	1.5296	1.7079
$4\,^3\Pi_g$	This work	51691.940	1226.038	−12.212	−1.721	1.13718	3.863	0.07995	1.5718	1.1315
$1\,^5\Pi_g$	This work	29981.496	963.787	6.245	−0.196	1.14275	6.414	0.01592	1.5680	2.5875

a. Chen et al. (2015) b. Chen et al. (2016) c. Krechkivska et al. (2018) d. Joester et al. (2007) e. V_{00} from $a\,^3\Pi_u$ state

TABLE 4.2. The configurations with $2\sigma_u\ 1\pi_u\ 3\sigma_g$ orbitals and their corresponding electronic states

configuration	electronic state
$2\sigma_u^2\ 1\pi_u^4\ 3\sigma_g^0$	$X\ ^1\Sigma_g^+$
$2\sigma_u^2\ 1\pi_u^3\ 3\sigma_g^1$	$A\ ^1\Pi_u$, $a\ ^3\Pi_u$
$2\sigma_u^2\ 1\pi_u^2\ 3\sigma_g^2$	$B\ ^1\Delta_g$, $B'\ ^1\Sigma_g^+$, $b\ ^3\Sigma_g^-$
$2\sigma_u^1\ 1\pi_u^4\ 3\sigma_g^1$	$D\ ^1\Sigma_u^+$, $c\ ^3\Sigma_u^+$
$2\sigma_u^1\ 1\pi_u^3\ 3\sigma_g^2$	$C\ ^1\Pi_g$, $d\ ^3\Pi_g$
$2\sigma_u^0\ 1\pi_u^4\ 3\sigma_g^2$	$E\ ^1\Sigma_g^+$

The triplet states $b\ ^3\Sigma_g^-$, $c\ ^3\Sigma_u^+$, and $d\ ^3\Pi_g$ have lower electronic energies compared with singlet states with similar configurations but different multiplicities. For example, $d\ ^3\Pi_g$ is about 23000 cm^{-1} lower than $C\ ^1\Pi_g$, but they have similar r_e and ω_e values with differences $\Delta r_e = 0.008$ Å and $\Delta\omega_e = 4\ \mathrm{cm}^{-1}$. $e\ ^3\Pi_g$ was first studied by Fox & Herzberg (1937) through the $e - a$ transition and then by Nakajima et al. (2009) through the $e - c$ transition. The V_{00} energy for the $e - a$ transition is 39296.5 cm^{-1}, which is about 500 cm^{-1} lower than the value reported by Fox & Herzberg (1937). With the aid of *ab initio* calculations, Krechkivska et al. (2015, 2017) found two new $^3\Pi_g$ states: $3\ ^3\Pi_g$ and $4\ ^3\Pi_g$. Their calculated and experimental energy levels indicate a strong vibronic interaction between these two electronic states. Figure 4.5 shows a comparison between the PECs of several $^3\Pi_g$ states calculated in their work and this work. The electronic energies of these states are close at short internuclear distances $R < 1.4$ Å, while the differences increase to about 1200 cm^{-1} around $R \approx 2.2$ Å. Despite the differences in energy, the shapes of these PECs match well with one another, suggesting that our calculation has good accuracy up to an energy of 40000 cm^{-1} (~ 5 eV) even though a slightly smaller basis set is used in this work.

We will focus on $^1\Pi_u$ states here because these states are directly related to the photodissociation of C_2. The $A\ ^1\Pi_u$ state lies only about 1 eV above the ground X state. Our calculated T_e is 8115.177 cm^{-1}, which is a bit smaller than the value 8391.406 cm^{-1}, reported by Chen et al. (2015). Our calculated vibrational constant 1594.881 cm^{-1} shows good agreement with the experimental value of 1608.217 cm^{-1}. The calculated $2\ ^1\Pi_u$ state has a double well structure, with an inner well located at 1.32 Å and an outer shallow well located at 2.25 Å. The dominant configuration of the $2\ ^1\Pi_u$ state at 1.32Å is $2\sigma_g^2\ 2\sigma_u^2\ 1\pi_u^3\ 4\sigma_g$. This inner potential well of $2\ ^1\Pi_u$ corresponds to the experimental $F\ ^1\Pi_u$ state which was first discovered by Herzberg et al. (1969). Our calculation agrees that the $F\ ^1\Pi_u$ state in this region is a Rydberg state with configuration $\sigma_u^2\pi_u^3 3s$ or $[^2\Pi_u, 3s]$. Then, the $2\ ^1\Pi_u$ state has an avoided crossing with the $3\ ^1\Pi_u$ state at 1.47 A. The electronic

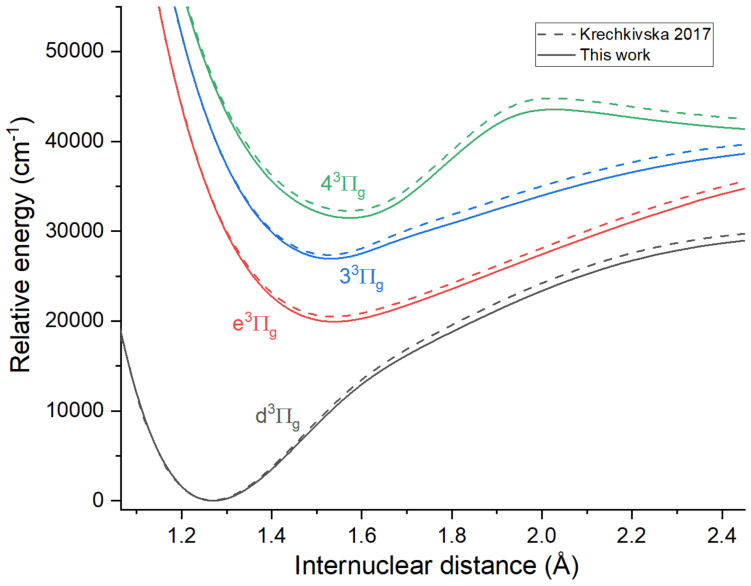

FIGURE 4.5. PECs of CASSCF(8,8)-MRCI/aug-cc-pV6Z+Dav+CV+Rel (Krechkivska et al., 2017) and DW-SA-CASSCF(8,12)-MRCI+Q/aug-cc-pV5Z+2s2p (this work). T_e of the $d\,^3\Pi_g$ state is set to 0 for both calculations.

structure of the outer potential well is more complicated and unable to be represented by just one primary configuration. A similar double-well structure has also been reported by Bruna & Grein (2001). Hereafter, the $2\,^1\Pi_u$ and $F\,^1\Pi_u$ labels are used interchangeably to refer to the Herzberg F state. The PECs of $^1\Pi_u$ states at energies higher than the F state contain frequent avoided crossings all over the internuclear distance range, with segments corresponding to different bound or non-bound states. From the PECs, at least another two bound states can be recognized. The first bound state contains these main segments built from $3\,^1\Pi_u$ at R <1.3 Å, $4\,^1\Pi_u$ from 1.3 to 1.4 Å, and $5\,^1\Pi_u$ from 1.4 to 1.5 Å. The dominant configuration of this state is $2\sigma_g^2\,2\sigma_u^2\,1\pi_u^3\,5\sigma_g$. The other bound $^1\Pi_u$ state has the potential well of the $4\,^1\Pi_u$ state at 1.5 Å.

$^3\Pi_u$ states are also important in C_2 photodissociation because they have spin-orbit couplings with $^1\Pi_u$ states. No $^3\Pi_u$ other than $a\,^3\Pi_u$ states have been studied by experiments so far. Bruna & Grein (2001) calculated and discussed the PECs of the 2-5 $^3\Pi_u$ states. Our calculation shows some substantial differences. In our calculation, the $2\,^3\Pi_u$ state is repulsive with avoided crossings with $3\,^3\Pi_u$ at R = 1.235 and 1.98 Å. The latter avoided crossing has a energy gap of 0.2 eV, indicating a strong non-adiabatic coupling. An almost flat shape is observed in the PEC from 1.5-2.0 Å. Both the $3\,^3\Pi_u$ and $4\,^3\Pi_u$ states have a deep potential well at R = 1.32 Å and have a barrier at longer distance. The $4\,^3\Pi_u$ state has obvious discontinuities at R = 1.40

and 1.69 Å, indicating some potential avoided crossings are not calculated correctly in our study. Those corresponding states may not be well described by our active space. For the same reason, The $5\,^3\Pi_u$ state calculated and shown here is likely inaccurate.

The last state shown in Figure 4.3 is $1\,^1\Delta_u$, which has been only studied experimentally by Goodwin & Cool (1988) and Goodwin & Cool (1989). The calculated PEC of the $1\,^1\Delta_u$ state has a potential minimum at 1.436 Å, which matches the experimental value exactly. The calculated T_e in this work is about 878 cm^{-1} higher than the experimental value of 57720^{-1}, while the ω_e in our work is about 60 cm^{-1} smaller than the experimental value of 1150 cm^{-1}. In the PEC, a slight bending is observed around 1.75 Å, indicating a strong adiabatic interaction with the $2\,^1\Delta_u$ state (shown in Figure 4.4) with a coupling estimated as 0.3 eV. By constructing a diabatic $1\,^1\Delta_u$ state from the adiabatic PECs, the resultant ω_e value would be expected to lie much closer to experimental one.

4.3.2. Important electronic transitions and their TDMs.

The selection rules for electronic transitions between homonuclear diatomic atoms in Hund's case (a) and (b) are:

$$\Delta\Lambda = 0, \pm 1; \quad \Delta S = 0; \quad + \nleftrightarrow -; \quad g \leftrightarrow u \tag{4.8}$$

To study the photodissociation of C_2, we need to consider not only the absorption from the ground state to available excited states, but also the spontaneous emission from the excited states which may decrease their lifetime and compete with predissociation. Among all states discussed so far, only those with $^1\Sigma_u^+$ and $^1\Pi_u$ symmetry can be directly excited from the ground $X\,^1\Sigma_g^+$ state. The $^1\Sigma_u^+$ excited states can relax to $^1\Pi_g$ and $^1\Sigma_g^+$ states by spontaneous emission, while the $^1\Pi_u$ states can relax to $^1\Sigma_g^+$, $^1\Sigma_g^-$, $^1\Pi_g$, and $^1\Delta_g$ states. For example, the $F\,^1\Pi_u$ state is able to relax to $X\,^1\Sigma_g^+$, $B'\,^1\Sigma_g^+$, $E\,^1\Sigma_g^+$, $C\,^1\Pi_g$, $2\,^1\Pi_g$, $3\,^1\Pi_g$, and $B\,^1\Delta_g$ states. Calculated TDMs for transitions relevant for C_2 photodissociation are shown in Figure 4.6 and Figure 4.7. All the TDMs shown here are in their absolute values. It is well known that TDMs calculated by MOLPRO are in random phases at different internuclear distances, thus a manual correction needs to be done to assign the correct phases for the TDMs.

As previously discussed, two $^1\Sigma_u^+$ states are calculated here, $D\,^1\Sigma_u^+$ and $2\,^1\Sigma_u^+$. Although the $v \geq 5$ vibrational states of $D\,^1\Sigma_u^+$ state are calculated to lie above the photodissociation threshold, transitions from the ground $X\,^1\Sigma_g^+$ (v=0) state are expected to have small Franck-Condon factors, and the corresponding

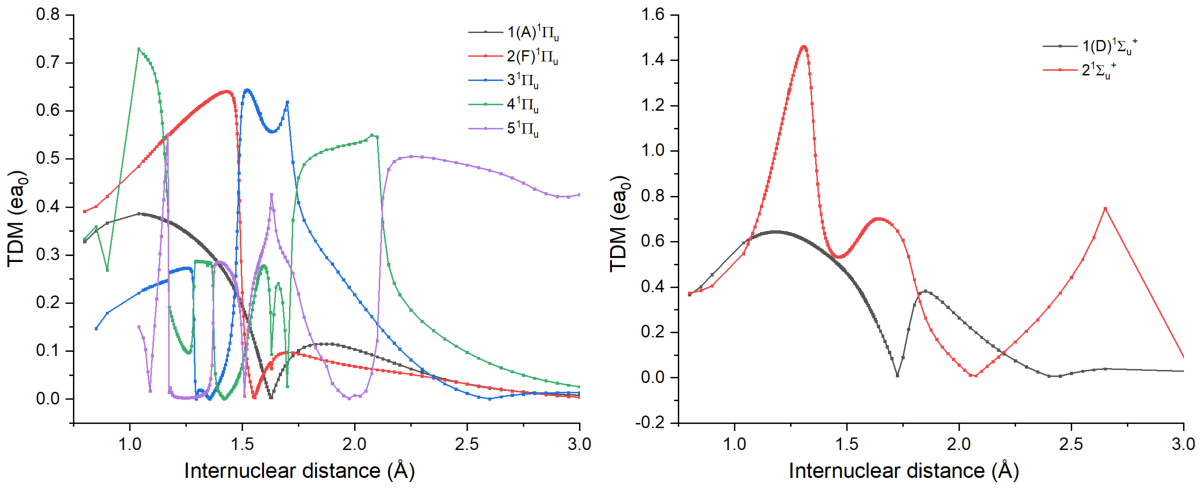

FIGURE 4.6. TDMs for transitions from the $X\,^1\Sigma_g^+$ state of C_2.

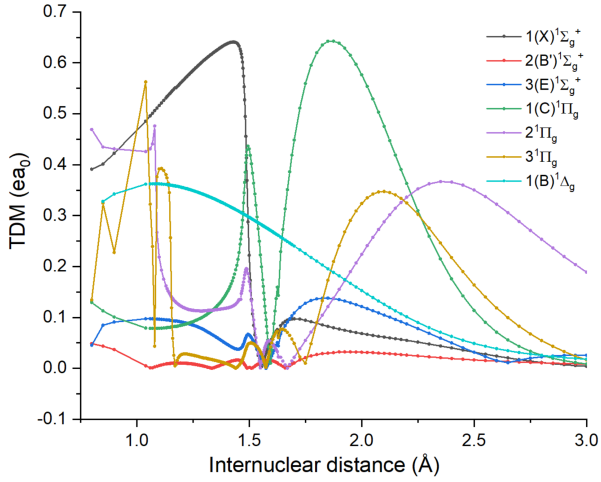

FIGURE 4.7. TDMs for transitions from the $F\,^1\Pi_u$ state of C_2.

bands have never been detected experimentally. The calculated $2\,^1\Sigma_u^+$ shows a double-well structure. The potential well at $R = 1.73$ Å arises from the avoided crossing with $D\,^1\Sigma_u^+$ state. The potential barrier at $R = 1.35$ Å, which is only about 0.042 eV above the potential well at $R = 1.31$ Å, is from the avoided crossing with another higher energy state which is not included in the calculation. As shown in Figure 4.8, the dominant configuration of the adiabatic $2\,^1\Sigma_u^+$ state changes smoothly from Rydberg $(2\sigma_g^2\,2\sigma_u^1\,1\pi_u^4\,4\sigma_g^1)$ to valence $(2\sigma_g^2\,2\sigma_u^2\,1\pi_u^1\,3\sigma_g^2\,1\pi_g^1)$ character though this avoided crossing. The TDM for the $X\,^1\Sigma_g^+ - 2\,^1\Sigma_u^+$ transition shown in Figure 4.6 (right) is quite large around $R = 1.25$Å. Therefore, it is expected that a strong

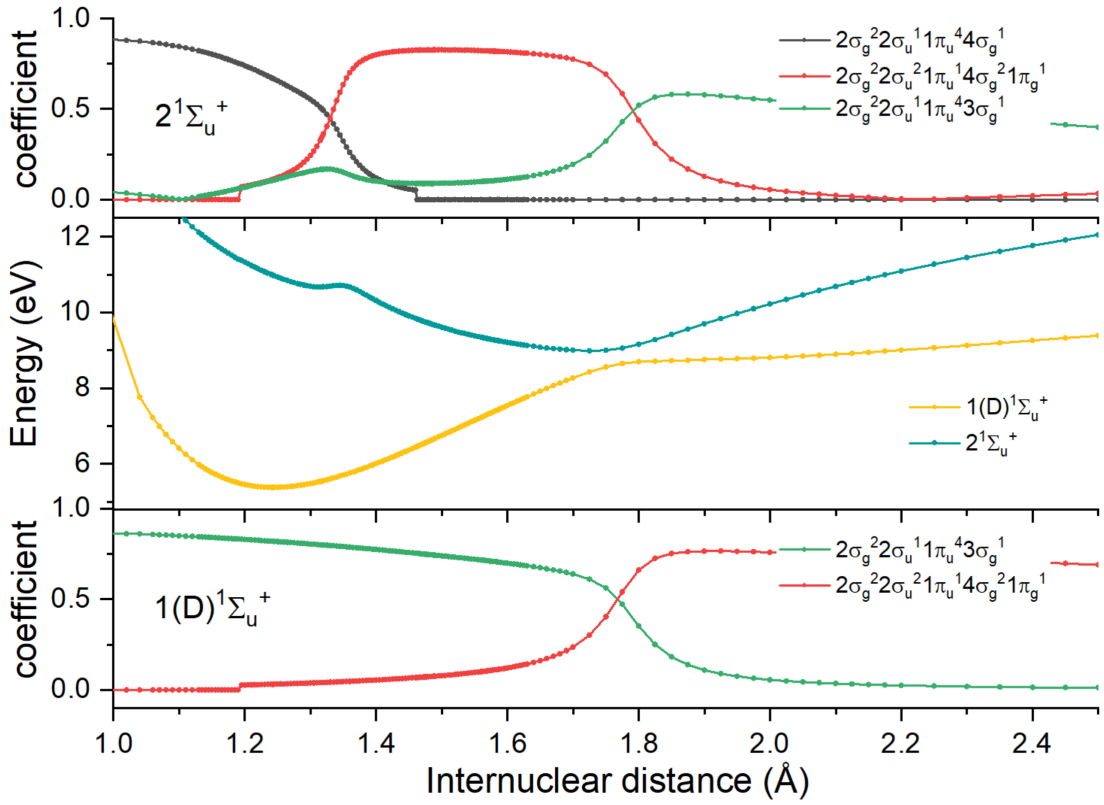

FIGURE 4.8. PECs of the $D\,^1\Sigma_u^+$ and $2\,^1\Sigma_u^+$ states, with the most important configurations. The same configuration is shown in same color between states.

absorption peak around 10.7 eV (116 nm) can be observed, and could give rise to predissociation through the nonadiabatic coupling with lower diabatic $^1\Sigma_u^+$ states. However, the spectrum in Herzberg et al. (1969) only covers 130-145 nm and the electronic states calculated by Bruna & Grein (2001) only covers 7-10 eV. This $2\,^1\Sigma_u^+$ state has not been reported by any previous studies, to the author's knowledge. Unfortunately, the PEC of the $3\,^1\Sigma_u^+$ state needed to construct a complete diabatic model of $2\,^1\Sigma_u^+$ is not calculated in this work, and thus a complete study on its absorption and dissociation is not carried out here.

Five $^1\Pi_u$ states are calculated in this work. Besides $A\,^1\Pi_u$, all are above the photodissociation threshold. As shown in Figure 4.6 (left), the TDM of the $F\,^1\Pi_u - X\,^1\Sigma_g^+$ transition is about 0.6 ea_0 around $R = 1.245$ Å, which is the equilibrium distance of the ground X state. The TDM from the ground X state to the diabatic state which can be constructed from the $3\,^1\Pi_u$, $4\,^1\Pi_u$, and $5\,^1\Pi_u$ states is about 0.27 ea_0 at $R = 1.245$ Å. The TDMs of transitions from $F\,^1\Pi_u$ to lower states are shown in Figure 4.7. Around R =1.245 Å, besides

$F\,^1\Pi_u - X\,^1\Sigma_g^+$, only the $F\,^1\Pi_u - B\,^1\Delta_g$ transition has a modest TDM of about 0.35 ea_0. It can be expected that the spontaneous emissions from the $F\,^1\Pi_u$ state to other states is insignificant.

4.3.3. Perturbations and Predissociation of $F\,^1\Pi_u$ state.

The CSE method is applied to study the photodissociation of C_2 in this work. Diabatic states are more convenient to use as an electronic state basis in the coupled-channel model. Building the coupled-channel model essentially involves building an interaction matrix $\mathbf{V}(R)$ whose diagonal elements are selected PECs of diabatic electronic states and whose off-diagonal elements are and couplings among them, including electrostatic couplings and SOCs.

The first step is to build diabatic PECs of $^1\Pi_u$ states from adiabatic ones. The NACMEs between excited $^1\Pi_u$ states are shown in Figure 4.9, along with the PECs of these states. Although it is possible to construct diabatic PECs by applying a unitary adiabatic-to-diabatic transformation (ADT) which can be calculated mathematically from NACMEs, the frequent nonadiabatic couplings among the $^1\Pi_u$ states makes such a transformation challenging (Nakamura, 2002). Thus, the NACMEs are only used as a guide to identity where interactions occur.

As previously discussed, $F\,^1\Pi_u$ is a Rydberg state with the configuration $[^2\Pi_u, 3s]$, so it is expected to have similar PEC shape as a $C_2^+\,^2\Pi_u$ state. The MRCI+Q PECs of the two lowest $^2\Pi_u$ electronic states of C_2^+ are shown in Figure 4.10 (left). The PEC of the $1\,^2\Pi_u$ state is slightly bent around $R = 1.6$ Å, indicating it has a nonadiabatic coupling with the $2\,^2\Pi_u$ state. The potential energy well of the $2\,^2\Pi_u$ state at $R = 1.52$ Å is from this nonadiabatic coupling, instead of an actual potential minimum. This can be verified by the calculated NACMEs, which show a broad and smooth peak centered at $R = 1.6$Å. Since this is a simple two-state system, a unitary ADT is used to diabatize these two states. We shifted the diabatic PECs of the $1\,^2\Pi_u$ and $2\,^2\Pi_u$ states to make the PEC of adiabatic $1\,^2\Pi_u$ state overlap with the $F\,^1\Pi_u$ state of C_2, as shown in Figure 4.10 (right). The PEC of the shifted diabatic $C_2^+\,1\,^2\Pi_u$ state follow the PECs of $C_2\,^1\Pi_u$ states closely (Nakamura, 2002). Thus, we use the the shifted PEC of $C_2^+\,1\,^2\Pi_u$ state to represent the C_2 $F\,^1\Pi_u$ state. Then, we connect the PECs of $4\,^1\Pi_u$ ($R < 1.26$ Å), $3\,^1\Pi_u$ ($1.26 < R < 1.47$ Å), and $F\,^1\Pi_u$ ($R > 1.47$ Å) to build the PEC for a repulsive diabatic $3\,^1\Pi_u$ state. The electrostatic interaction between these two diabatic states is estimated by half of the energy difference at R =1.475 Å as 0.015 eV (120 cm^{-1}). Another two diabatic bound states can be constructed from other $^1\Pi_u$ states. One corresponds to the C_2^+ diabatic $2\,^2\Pi_u$ state. Its r_e is about 1.6 Å, thus it should not be important for photodissociation studies of C_2

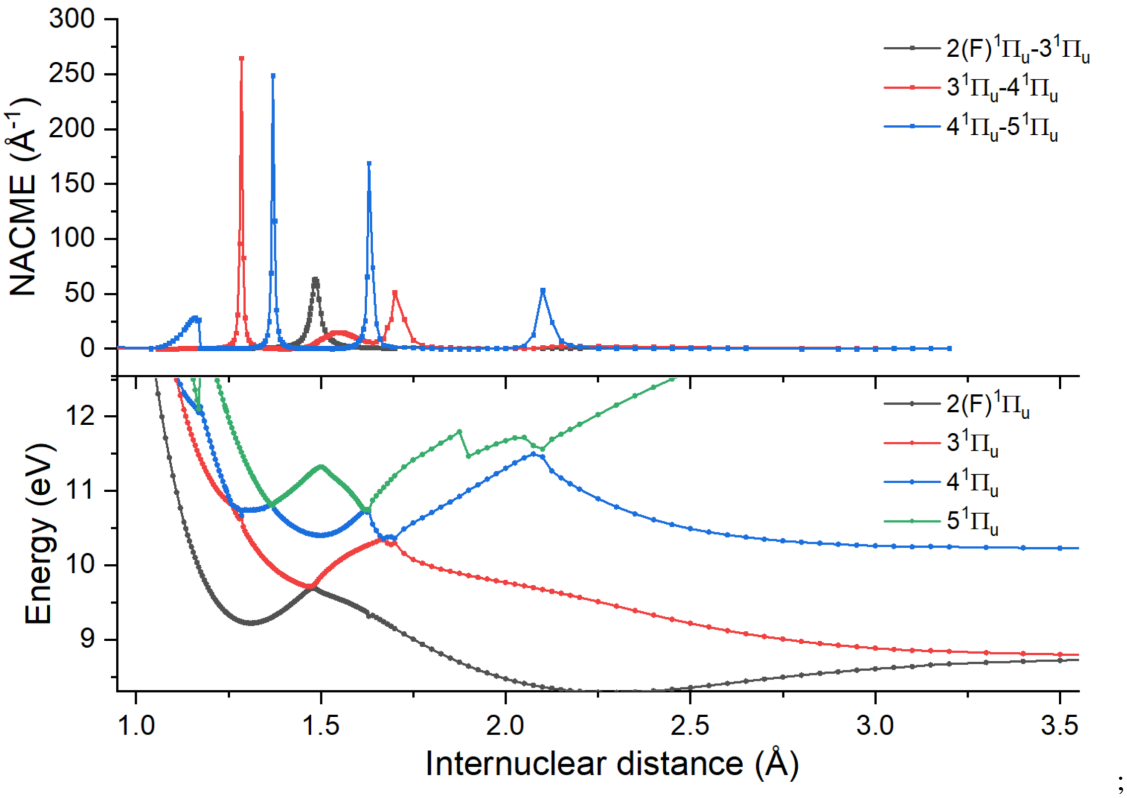

;

FIGURE 4.9. Top: MRCI NACMEs of C_2 $^1\Pi_u$ states. Bottom: MRCI+Q PECs.

owing to small Franck-Condon factors with the ground X state. Another constructed from the 3, 4, and 5 $^1\Pi_u$ states with r_e about 1.31 Å. The corresponding TDM is about half of the $F\,^1\Pi_u$ state, thus the intensity of absorption from the ground X state is estimated to be one fourth of the $F\,^1\Pi_u - X\,^1\Sigma_g^+$ band. In this study, we will only focus on the photodissociation via the $F\,^1\Pi_u$ state. The corresponding TDMs are diabatized by exchanging the curves on both sides of the avoided crossings and interpolating using cubic splines.

The spin-orbit interaction has been shown to be important in the predissociation of many diatomic molecules, such as O_2 (Lewis et al., 2001) and S_2 (Lewis et al., 2018). Based on the selection rules for spin-orbit coupling which are summarized as

$$\Delta J = \Delta\Omega = 0; \quad \Delta S = 0, \pm 1; \quad \Sigma^+ \leftrightarrow \Sigma^-; \quad g \nleftrightarrow u; \tag{4.9}$$

$$\Delta\Lambda = \Delta\Sigma = 0 \text{ or } \Delta\Lambda = -\Delta\Sigma = \pm 1,$$

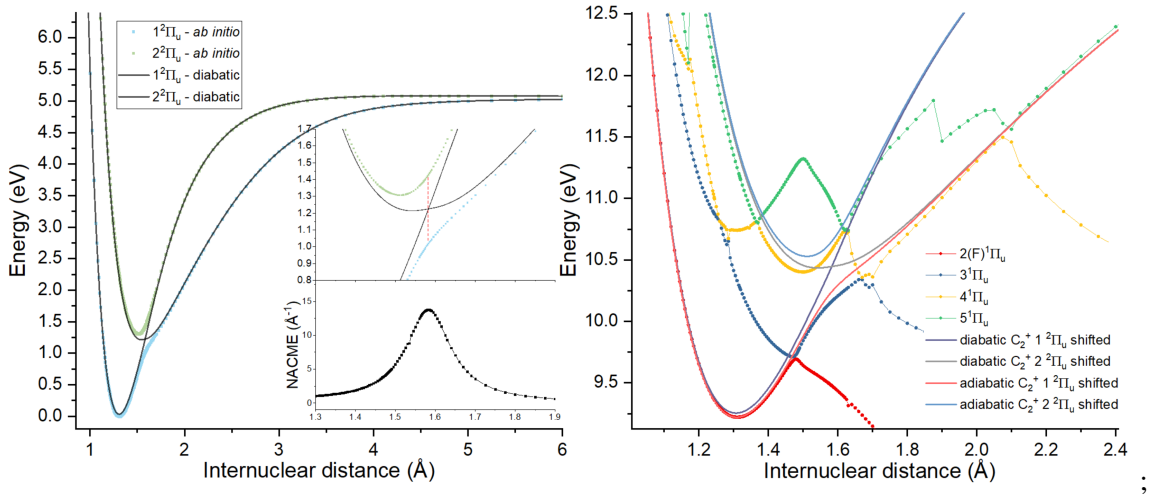

FIGURE 4.10. Left: adiabatic and diabatic PECs of C_2^+ $^2\Pi_u$ states. Inset: NACME between the two adiabatic $^2\Pi_u$ states. Right: shifted diabatic C_2^+ $^2\Pi_u$ states overlapped with C_2 $^1\Pi_u$ states.

the $F^2\,\Pi_u$ state is coupled with $^3\Sigma_u^+$, $^3\Sigma_u^-$, $^3\Pi_u$, and $^3\Delta_u$ states. The PECs of the $3\,^3\Sigma_u^+$, $2\,^3\Sigma_u^-$, and $2\,^3\Delta_u$ states cross that of the $F^1\,\Pi_u$ state at R =1.21, 1.33, and 1.21 Å, respectively. In addition, the $2\,^3\Pi_u$, $3\,^3\Pi_u$, and $4\,^3\Pi_u$ states are all close in energy to the PEC of $F^2\,\Pi_u$. Thus diabatic representations of those states are needed to build the coupled-channel model for predissociation through the $F\,^2\Pi_u$ state. The calculated SOCs are shown in Figure 4.11. The diabatic PEC of the $3\,^3\Sigma_u^+$ state is constructed similarly to the $3\,^1\Pi_u$ diabatic states: $3\,^3\Sigma_u^+$ converts to $2\,^3\Sigma_u^+$ around R =1.53 Å, and then to $1\,^3\Sigma_u^+$ around R = 1.75 Å. Likewise, the diabatic PEC of $2\,^3\Sigma_u^-$ is constructed from the adiabatic PEC of the $2\,^3\Sigma_u^-$ state at R <1.67 Å and the $1\,^3\Sigma_u^-$ state at R >1.67 Å. The diabatic PEC of $2\,^3\Delta_u$ crosses with $1\,^3\Delta_u$ around R =1.45 Å. However, the SOCs between the $3\,^3\Sigma_u^+$ and $2\,^3\Delta_u$ states with the $F\,^2\Pi_u$ state are almost 0 in the internuclear distance range of 1.2-1.5 Å, thus these two states are not considered further. The SOC value at R =1.33 Åwhere the $2\,^3\Sigma_u^-$ PEC crosses with the $F^1\,\Pi_u$, 1.6 cm^{-1} is adopted in the coupled-channel model. The $3\,^3\Pi_u$ and $4\,^3\Pi_u$ states lie close with each other around r =1.25 Å, thus it is challenging to construct diabatic states for them. In this study, we use the adiabatic curves of the $2\,^3\Pi_u$, $3\,^3\Pi_u$ and $4\,^3\Pi_u$ states as their diabatic representations. The SOCs between them and the $F^1\,\Pi_u$ state are stable around the equilibrium bond length of the $F^1\,\Pi_u$ state, so 0.5, 15, 8.0 cm^{-1} are adopted as the constant SOC value between the $F^1\,\Pi_u$ state and the $2\,^3\Pi_u$, $3\,^3\Pi_u$ and $4\,^3\Pi_u$ states, respectively. Thus final coupled-channel model, including the diabatic $F^1\,\Pi_u$, $3^1\,\Pi_u$, $2\,^3\Sigma_u^-$, $2\,^3\Pi_u$, $3\,^3\Pi_u$ and $4\,^3\Pi_u$ states, is shown in Figure 4.12.

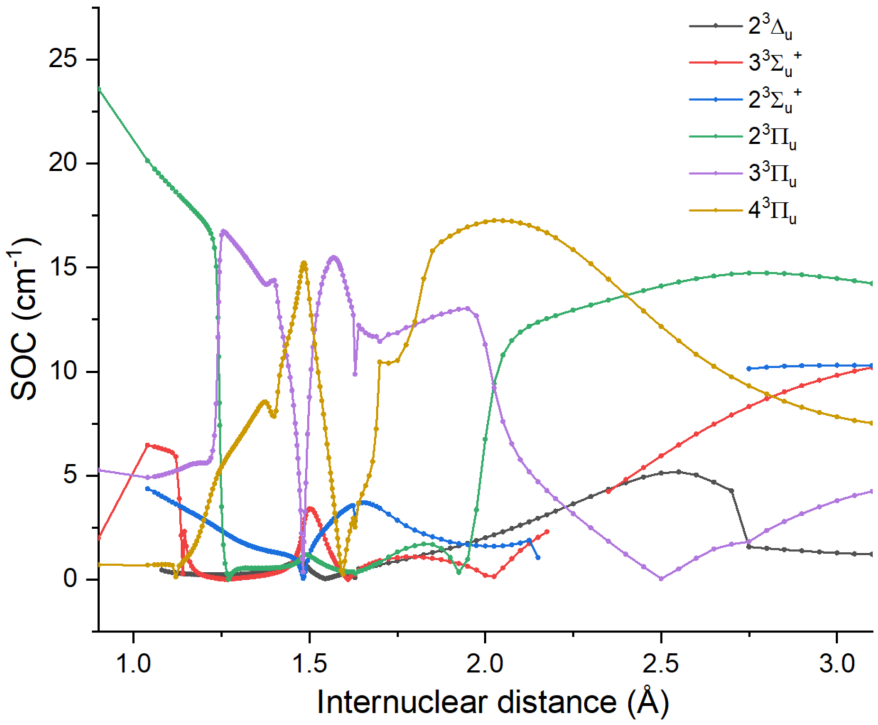

FIGURE 4.11. SOCs between several triplet states and the $F\ ^1\Pi_u$ state of C_2.

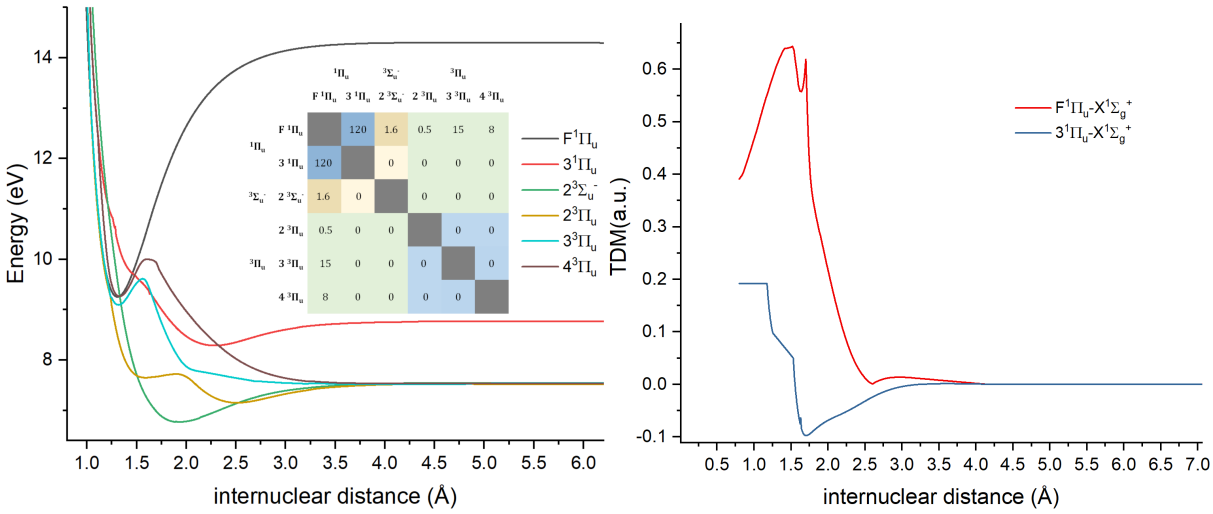

FIGURE 4.12. Coupled-channel model built for predissociation of the C_2 $F\ ^1\Pi_u$ state. Left: PECs of the electronic states, with the interaction matrix inset. Right: TDMs between the ground $X\ ^1\Sigma_g^+$ state and diabatic $F\ ^1\Pi_u$ and $3\ ^1\Pi_u$ states.

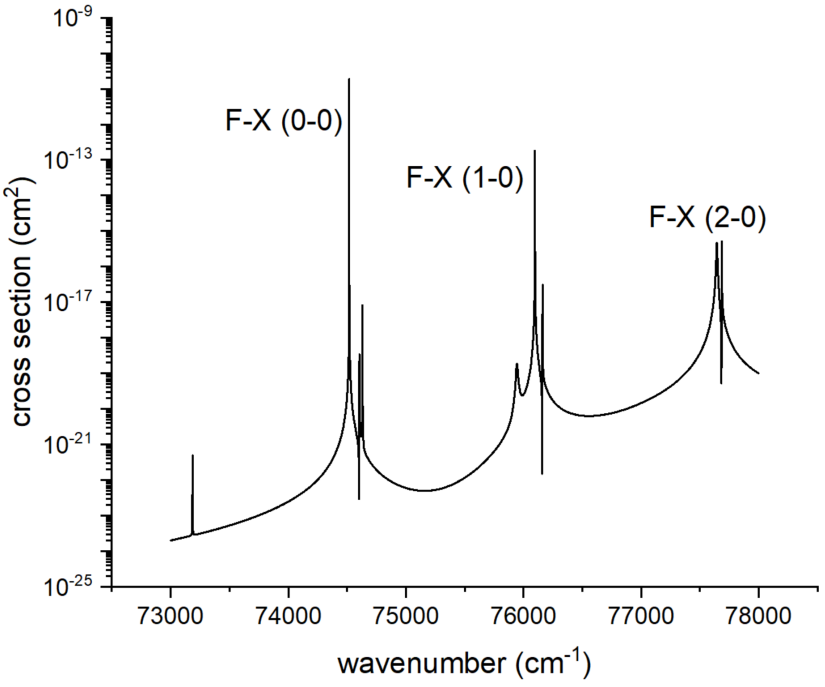

FIGURE 4.13. Rotationless photodissociation cross sections of the $X\,^1\Sigma_g^+$ state of C_2 via the $F\,^1\Pi_u$ state.

From the coupled-channel model, we calculated the rotationless photodissociation cross sections in the energy range between 73000-78000 cm^{-1} from the ground vibronic $X\,^1\Sigma_g^+$ (v=0) state via the $F\,^1\Pi_u - X\,^1\Sigma_g^+$ transition, as shown in Figure 4.13. The calculated $F - X$ (0-0) band is located at 74521.2 cm^{-1} with a linewidth of 0.0014 cm^{-1} and an integrated cross section 7.98×10^{-14} cm^{2}cm^{-1}, while the $F - X$ (1-0) band is at 76099.7 cm^{-1} with a linewidth of 0.079 cm^{-1} and integrated cross section of 4.00×10^{-14} cm^{2}cm^{-1}. The derived predissociation lifetime τ_{pd} is 3.78 ns and 0.067 ns for the $F\,^1\Pi_u$ v=0 and v=1 states.

Spontaneous emission lifetimes (τ_{se}) of the $F\,^1\Pi_u$ v =0 and v =0 states are computed from the adiabatic PECs and TDMs shown in Figure 4.3 and Figure 4.7 using the program DUO (Yurchenko et al., 2016). As discussed above, only the $F\,^1\Pi_u - X\,^1\Sigma_g^+$ and $F\,^1\Pi_u - B\,^1\Delta_g$ transitions are considered. The total Einstein A_{21} coefficient is computed by

$$A_{21}(F, v') = \sum_{v''} A_{21}(F - X, v' - v'') + \sum_{v''} A_{21}(F - B, v' - v''). \tag{4.10}$$

The A_{21} coefficients for the $F\,^1\Pi_u - X\,^1\Sigma_g^+$ transition are 2.95×10^8 s^{-1} for the v=0 state and 2.92×10^8 s^{-1} for the v=1 state, while for the $F\,^1\Pi_u - B\,^1\Delta_g$ transition are 5.34×10^7 s^{-1} for the v=0 state and 5.28×10^7 s^{-1}

for the v=1 state. The values of the A_{21} coefficients yield a total lifetime of 2.87 ns for the v=0 state and 2.90 ns for the v=1 state. Based on our model, the predissociation through $F\,^1\Pi_u$ v=1 state is more than 40 times faster than spontaneous emission, while the predissociation via its v=0 state is a little slower than spontaneous emission, as summarized in Table 4.3.

Hupe et al. (2012) reported a lifetime of 0.006 ns for the $F\,^1\Pi_u$ state derived from measured linewidths of the $F\,^1\Pi_u - X\,^1\Sigma_g^+$ (0-0) and (1-0) transitions, which suggests the upper states decay rapidly via predissociation. The accuracy of our calculations relies on the calculated *ab initio* couplings. For example, if the SOC between $F\,^1\Pi_u$ and $2\,^3\Sigma_u^-$ state increases from 1.6 cm^{-1} to 10 cm^{-1}, then the calculated linewidth for $F - X$ (0-0) increases from 0.0014 cm^{-1} to 0.050 cm^{-1}, which corresponding to a lifetime of 0.11 ns. The predissociation in this model would then be significantly faster than spontaneous emission.

TABLE 4.3. Properties of the $F - X$ transitions of C2.

Band		v_{expt} [a] (cm^{-1})	v (cm^{-1})	γ (cm^{-1})	σ_0 ($cm^2 cm^{-1}$)	τ_{pd} ns	$A_{21,(F-X)}$ (s^{-1})	$A_{21,(F-B)}$ (s^{-1})	$A_{21,tot}$ (s^{-1})	τ_{se} (ns)
$F - X$	(0-0)	74550[c]	74521.2	0.0014	7.98×10^{-14}	3.78	2.95×10^{8}	5.34×10^{7}	3.48×10^{8}	2.87
	(1-0)	76105[c]	76099.7	0.079	4.00×10^{-14}	0.067	2.92×10^{8}	5.28×10^{7}	3.45×10^{8}	2.90

a. band heads reported by Herzberg et al. (1969).

In our current model, the branching ratios can be obtained by comparing the photodissociation cross sections of different open channels. Predissociation of both $v = 0$ and $v = 1$ states produce $^3P + {}^1D$ atomic carbon products.

Assuming all photoabsorption leads to photodissociation, under the standard interstellar radiation field (ISRF), the photodissociation rate over this range of wavenumbers is $4.76\times10^{-10}\,s^{-1}$, with a contribution from the $F - X$ (0-0) transition of $2.84\times10^{-10}\,s^{-1}$ and from the $F - X$ (1-0) transition of $1.39\times10^{-10}\,s^{-1}$. The Leiden database contains two transitions involving the F state. One is in the wavelength range 130-134 nm, which is likely from the Herzberg $F - X$ band, and the other, in the range 110-120 nm, is likely from the theoretical $F - X$ transition in Pouilly et al. (1983). The photodissociation rates calculated from these two bands are $6.66\times10^{-11}\,s^{-1}$ and $4.40\times10^{-11}\,s^{-1}$, respectively. It is likely that the photodissociation rate under the ISRF is underestimated by present astronomical models.

4.4. Conclusion

Here we have presented a detailed *ab initio* theoretical study of C_2 photodissociation focusing on the predissociation of the $F\,^1\Pi_u$ state. Potential energy curves for a total of 57 electronic states were calculated with the DW-SA-CASSCF/MRCI+Q method with a basis set aug-cc-pV5Z+2s2p. By using an (8,12) active space, the Rydberg nature of the $F\,^1\Pi_u$ state was confirmed, and non-adiabatic couplings among the excited $^1\Pi_u$ states as well as SOCs between $F\,^1\Pi_u$ and other triplet states were explored. Then, a coupled-channel model was used to simulate the photodissociation cross section of C_2 via its $F\,^1\Pi_u - X\,^1\Sigma^+$ transition.

We reproduced the $F\,^1\Pi_u - X\,^1\Sigma^+$ (0-0) and (1-0) bands in our photodissociation cross section calculation. By comparing the derived predissociation lifetime with the computed spontaneous emission lifetime, the v =1 state was found to decay rapidly through predissociation. Unlike the results reported by Hupe et al. (2012), the predissociation rate of the v=0 state was found to be comparable with spontaneous emission in this study. Accurate modeling of predissociation depends on precise coupling terms, which would benefit from further experimental studies of the $F - X$ band. Moreover, we predict a strong $D\,1\Sigma_u^+ - X\,^1\Sigma^+$ absorption peak around 10.7 eV which could also give rise to fast predissociation, and should be a priority for experimental measurements.

CHAPTER 5

Experimental Exploration of the CS photodissociation with VUV-VUV-VMI Technique

5.1. Introduction

5.1.1. Photodissociation of CS.

The background and motivation of studying the photodissociation of carbon monosulfide (CS) is already thoroughly discussed in Chapter 3.1. In summary, carbon monosulfide (CS) is one of the most abundant S-bearing molecules detected in space (Neufeld et al., 2015; Semenov et al., 2018) and plays an important role in sulfur chemistry in many astronomical environments. In general, the S-chemistry is poorly reproduced by modern astrochemical models. Lucas & Liszt (2002) and Neufeld et al. (2015) measured the abundances of several S-bearing molecules including CS, SO, and HCS^+ in diffuse clouds and built the most recent S-chemistry model. Lucas & Liszt (2002) found that the column density of HCS^+ is under-predicted by a factor of 25 by their model, although it is able to reproduce the column density of CS easily. Corby et al. (2018) observed S-bearing species in a variety of diffuse/translucent clouds, finding that the CS:HCS^+ ratio exhibits greater variability among environments in comparison with the observations of Lucas & Liszt (2002), and that SO and H_2CS are significantly over-predicted by chemical model. Thus they suggested that the S-chemistry in models of diffuse clouds should be revisited. In photon-dominated regions (PDRs) and diffuse molecular clouds, photodissociation by ultraviolet (UV) radiation is the key destruction pathway for CS (Lucas & Liszt, 2002). Determining the accurate photodissociation rate of CS may improve the S-related parts of astrochemical models.

While a number of studies have been conducted on the ground $X\,^1\Sigma^+$ state and several other low-lying excited states (Barrow et al., 1960; Bell et al., 1972; Cossart & Bergeman, 1976; Field & Bergeman, 1971; Huber & Herzberg, 1979; Kewley et al., 1963; Lovas & Krupenie, 1974; Mockler & Bird, 1955; Taylor et al., 1972; Tewarson & Palmer, 1968), spectroscopy of CS in UV regions has only been studied experimentally by Crawford & Shurcliff (1934), Donovan et al. (1970), and Stark et al. (1987). Bruna et al. (1975) carried

out a low-level theoretical calculation on highly excited states of CS, including the $B\,^1\Sigma^+$ and $C\,^1\Sigma^+$ states. However, all spectra obtained to date were low-resolution and none of them particularly focused on the photodissociation of CS. With the increase of computing capabilities, theoretical calculations using higher levels of theory and larger basis set are achievable. Pattillo et al. (2018) and Chapter 3 (Xu et al., 2019) conducted high-level *ab initio* studies to derive the photodissociation cross sections of CS in UV region. Although the calculation presented in Chapter 3 is able to reproduce several $B - X$ and $C - X$ vibronic transitions, the calculation still has limitations. For example, the choice of active space in the calculations may not be adequate for describing the potential energy curves of Rydberg states with higher principal quantum number n. Also, the treatment of couplings among the electronic states in the coupled-channel model is probably oversimplified. Thus, further high resolution experiments are required to verify the results of quantum theoretical calculations. Moreover, the calculation in Chapter 3 predicts that the main atomic products generated by predissociation through the $C\,^1\Sigma^+ - X\,^1\Sigma^+$ (0-0) and (1-0) transitions are C(^3P) + S(^1D). S atoms in metastable ^1D state may contribute internal energy to gas-phase chemical reactions. However, the branching ratios are sensitive to the details of the couplings in the coupled-channel model. Experiments are able to distinguish the different branching ratios, and thereby improve the theoretical treatment of the excited states.

High resolution state-to-state experimental studies of CS photodissociation are extremely challenging. Using the vacuum UV laser pump-probe velocity-map imaging (VUV-VUV-VMI) technique, Gao et al. (2013a), Song et al. (2016),and Lu et al. (2015) conducted studies on photodissociation of CO , N_2, and CO_2 successfully. However, no transient molecules have been studied using this apparatus yet so far. CS is a short-lived, highly reactive gaseous species. To study the photodissociation of CS, it must be produced and manipulated directly in the vacuum chamber. In astronomical environments such as diffuse clouds and PDRs, the molecule CS is almost purely distributed in its ground vibronic ($X\,^1\Sigma^+, v'' = 0$) state. Thus the CS generated in the vacuum chamber must be cooled to the ground vibronic state before interacting with photodissociation laser. This presents an extra challenge compared to all the previous experiments done with this apparatus.

The most straightforward method to generate CS is through photolysis of carbon disulfide (CS_2):

$$CS_2 \xrightarrow{h\nu} CS + S. \tag{5.1}$$

This dissociation reaction can also be accomplished by thermolysis or discharge. In general, the overall energetics of CS_2 photodissociation have been well-established, but the internal state distribution of CS formed though the processes is still not well understood. Other possible precursors to generate CS include thiophene (C_4H_4S), methanethiol (CH_3SH), dimethyl sulfide ($(CH_3)_2S$), methyl thiocyanate (CH_3SCN), methyl isothiocyanate (CH_3NCS), diethyl methylphosphonothioate ($C_5H_{13}O_2PS$), and isothiocyanic acid (HNCS) (Moltzen et al., 1988). However, compared to CS_2, those precursors have more atoms than just C and S atoms, and therefore may generate complicated molecules in the dissociation process, introducing additional experimental complications. So CS_2 is the most suitable precursor for our research purpose.

This dissertation describes efforts to measure the photodissociation of CS cooled to its ground vibronic state following by CS_2 photodissociation. Initially, the plan was to use the VUV-VUV-VMI technique to probe the $B\,^1\Sigma^+ - X\,^1\Sigma^+$ and $C\,^1\Sigma^+ - X\,^1\Sigma^+$ electronic transition and the excited electronic state $C\,^1\Sigma^+$ will be studied. The photodissociation cross sections measured could than be compared with the cross sections calculated in Chapter 3.1. However, due to several instrument failures and the experimental delays caused by COVID pandemic, the experiments has not been completed. Preliminary results obtained to date are shown in this chapter. The next steps for improving instruments are also discussed.

5.1.2. Photodissociation of CS_2.

Disulfur (S_2) has been detected in many comets, including C/1995 O1 (Hale-Bopp), C/1996 B2 (Hyakutake), and 67P, with an abundance of up to 0.02% relative to water (Le Roy et al., 2015). In comets, the dominant destruction pathway of S_2 is photodissociation through the absorption $B\,^3\Sigma_u^- - X\,^3\Sigma_g^-$ at around 280 nm. Given the short photodissociation lifetime, calculated to be about 500 s, the high abundance of S_2 in comets is surprising, suggesting the production rate of S_2 is higher than predicted by chemical models of comets (Almeida & Singh, 1986). This high abundance has been proposed to arise from larger than expected amounts of S_2 present in the cometary ices or from production in the gas phase from unverified reactions. For example, Ahearn et al. (1983), Cochran et al. (2015), and Despois et al. (2005) suggested that CS_2 is likely the parent molecule of S_2. On the other hand, Jiménez-Escobar et al. (2012) proposed that the main source of S_2 in comets could be dissociation of H_2S_2 in the ice by X-rays. At present, the origin of S_2 remains unclear (Trabelsi et al., 2018).

In 2014, Lu et al. (2014) found that photodissociation of CO_2 can produce C + O_2 directly. The results show the branching fraction of the $C(^3P)$ + $O_2(X\,^3\Sigma_g^-)$ channel is about 5% compared to the most favorable

$O(^1S)$ + $CO(X\,^1\Sigma^+)$ channel near the energetic threshold of the $C(^3P)$ + $O_2(X\,^3\Sigma_g^-)$ channel. Because CO_2 and CS_2 are valence isoelectronic, direct photodissociation of $CS_2 \longrightarrow C(^3P) + S_2\,(X\,^3\Sigma_g^-)$ may also be feasible. Inspired by this study, Trabelsi et al. (2018) conducted a theoretical calculation at the MRCI/aug-cc-pV(5+d)Z level which found that the process $CS_2 \longrightarrow CSS \longrightarrow C + S_2$ is possible. At the time this project began, there had been no experimental evidence of this reaction.

While optimizing the production of CS from photodissociation of CS_2 in the VUV-VUV-VMI apparatus, evidence for the C + S_2 photodissociation channel was observed. This may provide new ideas for understanding the high abundance of S_2 detected in comets despite its short photodissociation lifetime. In 2021, Li et al. (2021) also reported the direct observation of the C + S_2 channel in CS_2 photodissociation using a similar experimental design, albeit at different wavelengths than used here. Here we present the preliminary observation of C + S_2 in the 201.22 nm photodissociation of CS_2.

5.2. Experimental setup

Figure 5.1 shows the schematic diagram of the VUV-VUV-VMI apparatus designed for state-to-state photodissociation studies. The apparatus was initially set up with the main vacuum chamber and a single VUV system in 2008 (Zhou et al., 2008). Later, a second VUV system with same design was added (Gao et al., 2013b). In its present form, the apparatus consists of two VUV laser systems, a molecular beam production system, and a VMI detector system. For CS studies, a molecular beam of CS_2 seeded in buffer gas (He, N_2, or Ar) is produced by supersonic expansion through an Evan-Lavie pulsed valve (E-L valve). A UV laser is focused on the exit of the E-L valve and photolyzes CS_2 to form CS and S. The molecular beam of CS, S, and remaining CS_2 enters the photodissociation/photoionization (PD/PI) interaction region after dual skimmers. In the PD/PI region, the molecular beam crosses with two VUV lasers: the first one performs state-selective excitation in the $C\,^1\Sigma^+ - X\,^1\Sigma^+$ band of CS. After a delay of about 10 ns to allow for predissociation to form C and S atoms, the second laser selectively photoionizes either an atomic fragment or the parent molecule CS. The ionized products are then accelerated by a set of ion lenses toward a pair of microchannel plates (MCP) coupled to a phosphor screen for detection.

The VUV lasers are generated by four-wave mixing, which is a parametric nonlinear process. In four-wave mixing, a fourth frequency is generated by the interaction of three frequencies in a nonlinear medium. In 1982, Hilbig & Wallenstein (1982) successfully generated narrow band tunable VUV radiation in Kr

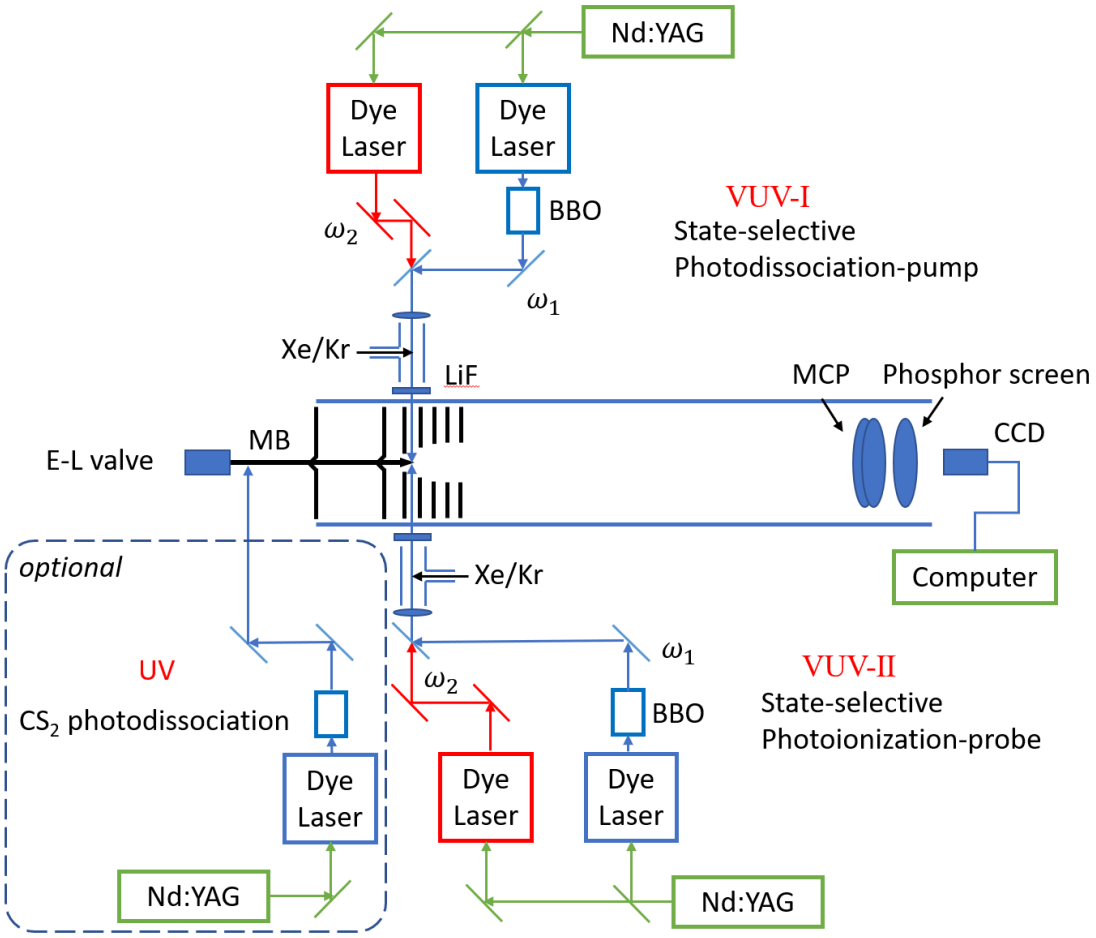

FIGURE 5.1. Schematic diagram of the VUV-VUV-VMI technique with an optional UV laser

and Xe with the frequency $\omega_{\mathrm{VUV}} = 2\omega_{\mathrm{UV}} \pm \omega_{\mathrm{vis}}$ using the sum- and difference-frequency four-wave mixing technique. The VUV laser system in this apparatus is based on same four-wave mixing design shown in Figure 5.2. In the nonlinear medium Xe or Kr, the output of a UV laser (ω_1) and the output of a visible dye laser (ω_2) give rise to sum-frequency output $2\omega_1 + \omega_2$ and difference-frequency output $2\omega_1 - \omega_2$ when twice the frequency of a UV laser ($2\omega_1$) matches with an electronic transition of Xe or Kr. As shown in Figure 5.1, the UV laser is produced from the second or third harmonic output of a dye laser. Both dye lasers are pumped by an injection seeded Nd:YAG laser. By using several ω_1 frequencies and tuning ω_2, coherent tunable VUV radiation is obtained with continuous coverage in the 7-16 eV spectral range with an optical bandwidth of 0.45 cm^{-1} (Zhou et al., 2008). The most used ω_1 frequencies and the VUV energy coverage are

shown in Figure 5.3, with some ionization energies (IE) and photodissociation thresholds of several species related to this dissertation.

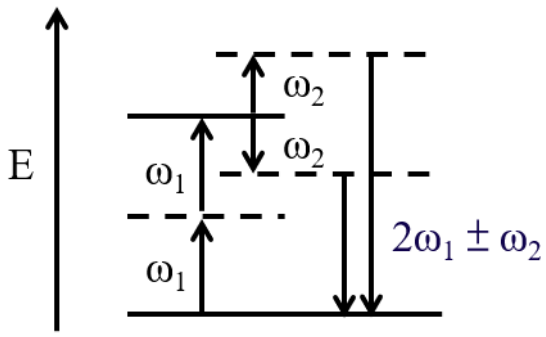

FIGURE 5.2. Schematic of four-wave mixing to generate VUV in Xe or Kr.

The UV laser used for CS_2 dissociation is generated from a frequency tripled dye laser pumped by An Nd:YAG laser. The fundamental wavelength (603.66 nm) of the dye laser is first frequency-doubled with a SHG crystal to yield a wavelength of 301.83 nm. The doubled frequency thus generated along with the residual fundamental frequency are mixed by a THG crystal to yield a wavelength of 201.22 nm and a pulse energy of about 1 mJ/pulse. This UV laser was aligned to cross molecular beam either at the exit of the E-L valve or in the PD/PD region.

5.3. Results and discussions

5.3.1. Photodissociation study of CS_2 by UV in 201.22 nm.

Figure 5.4 shows the CS_2 absorption spectrum in the UV region (Xu & Joens, 1993). Following excitation in the 185-230 nm region, CS_2 presents strong absorption structures which is attributed to the $^1B_2(^1\Sigma_u^+) - X\,^1\Sigma_g^+$ transition. The photodissociation energy threshold for CS_2 is 4.46 eV (278 nm). The $^1B_2(^1\Sigma_u^+)$ state is predissociative and has been chosen for CS_2 photodissociation studies for decades. In this work, a wavelength of 201.22 nm was utilized to photolyze CS_2 and one VUV laser was used to selectively probe an atomic fragment (C or S). Both lasers cross with the molecular beam in the PD/PI interaction region.

Figure 5.5 shows the photo-fragment excitation (PHOFEX) spectrum of the S atom from CS_2 photodissociation as function of VUV energy between 69450-70300 cm^{-1} (8.6107-8.7161 eV), which produce S^+ via a VUV-vis resonance-enhanced multiphoton ionization (REMPI) scheme. In Figure 5.5, five transition

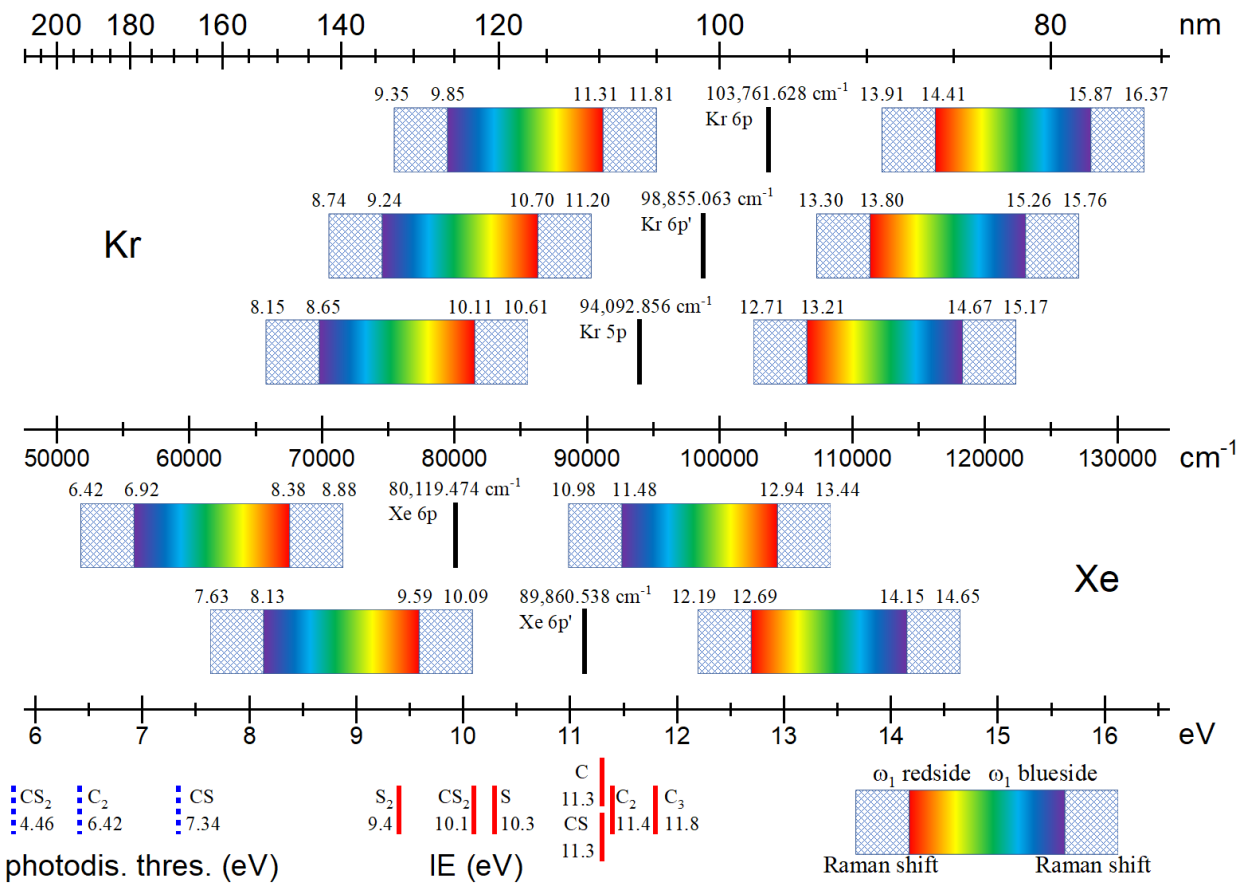

FIGURE 5.3. The energy coverage of VUV photons generated by four-wave mixing using xenon and krypton as a nonlinear medium. The IE and photodissociation threshold of several C- and S-containing species are also shown.

peaks are observed with VUV energies of 69591.41, 69768.96, 69770.30, 70166.22 and 70174.36 cm^{-1}, which are assigned to $[3s^23p^3(^4S^o)3d]\,^3D_1^o - {}^3P_0$, $[3s^23p^3(^4S^o)3d]\,^3D_1^o - {}^3P_1$, $[3s^23p^3(^4S^o)3d]\,^3D_2^o - {}^3P_1$, $[3s^23p^3(^4S^o)3d]\,^3D_2^o - {}^3P_2$, and $[3s^23p^3(^4S^o)3d]\,^3D_3^o - {}^3P_2$, respectively.

We then utilized the transitions at 69591.41, 69770.3 and 70174.36 cm^{-1}, which selectively probe S($^3P_0$), S($^3P_1$) and S($^3P_2$), to study the CS_2 photodissociation dynamics. Figure 5.6 (a, c, e) shows the time-sliced velocity map image (TS-VMI) of S($^3P_0$), S($^3P_1$), and S($^3P_2$) produced by CS_2 photolysis at 201.22 nm and probed by the VUV-vis (1+1′) REMPI method. The 0 K heats of formation for CS_2 ($X\,^1\Sigma_g^+$), CS ($X\,^1\Sigma^+$), and S ($^3P_2$) are 1.2013, 2.8316, and 2.8493 eV, respectively (Chase, 1998). The 0 K dissociation energy for CS_2 ($X\,^1\Sigma_g^+$) to split into CS ($X\,^1\Sigma^+$) + S ($^3P_2$) is thus derived to be D_0 = 4.4798 eV. The TKER of this

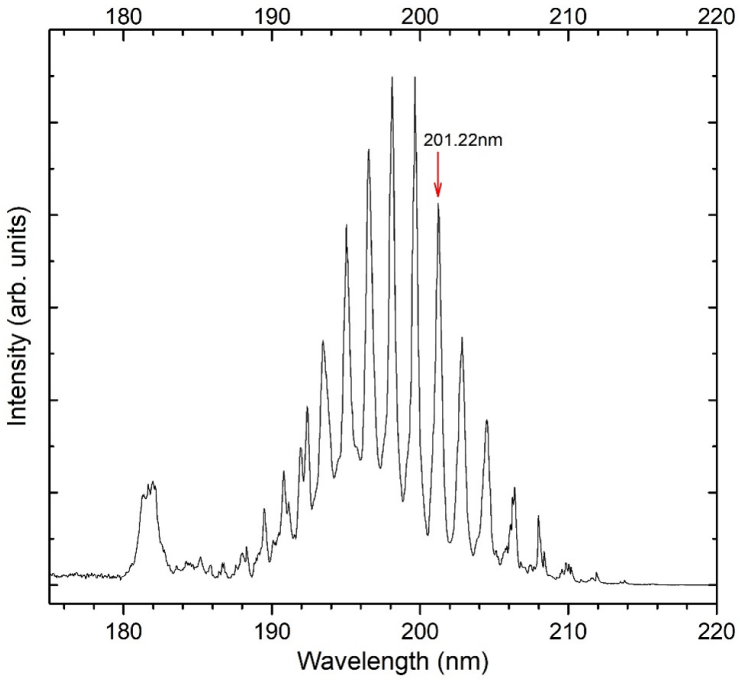

FIGURE 5.4. CS_2 absorption spectrum (Xu & Joens, 1993).

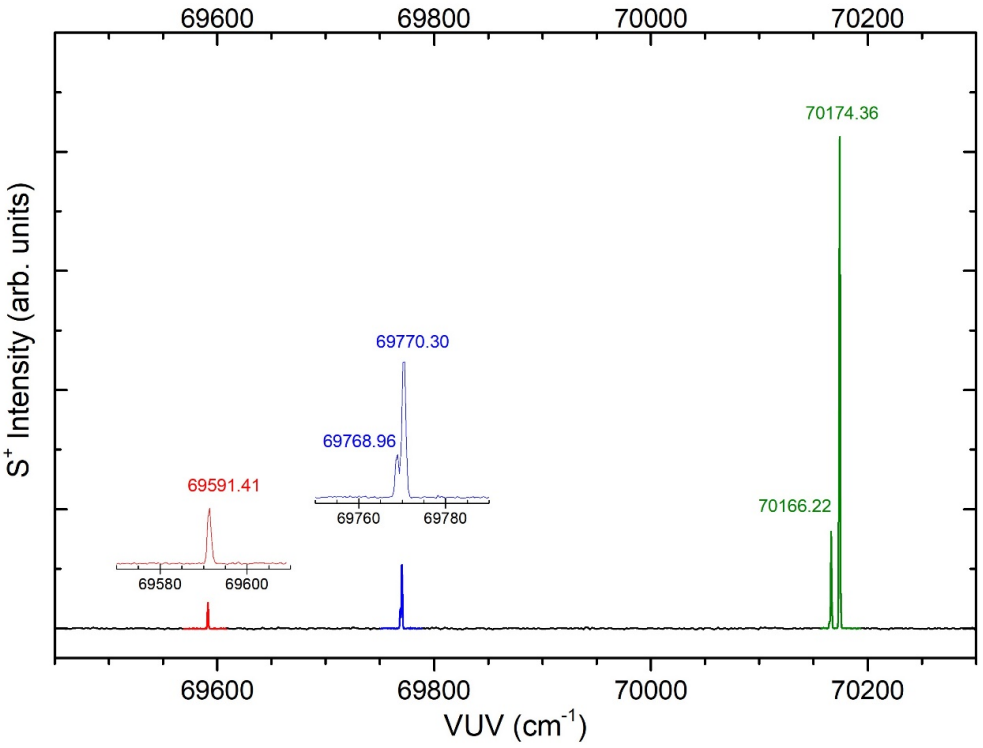

FIGURE 5.5. PHOFEX spectrum of S from CS_2 photodissociation at 201.22 nm.

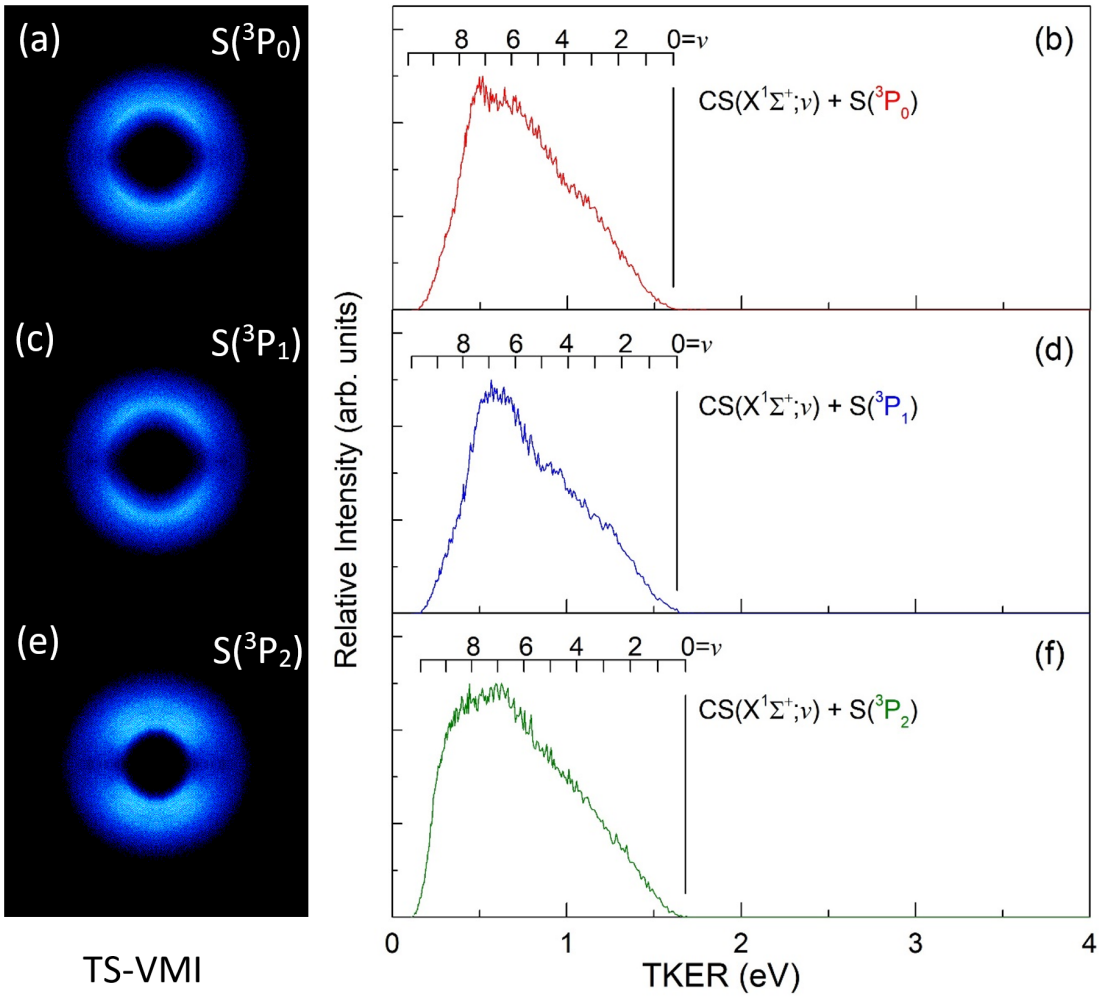

FIGURE 5.6. TS-VMI images for photofragments of (a) S($^3P_0$), (c) S($^3P_1$), and (e) S($^3P_2$) from CS_2 photodissociation at 201.22 nm UV and the corresponding TKER spectra for (b) S($^3P_0$)+CS, (d) S($^3P_1$)+CS, and (f) S($^3P_2$)+CS.

reaction can be calculated by

$$\text{TKER}[\text{CS}(X\,^1\Sigma^+) + \text{S}(^3P_J)] = h\nu(202.22\,\text{nm}) - D_0 - E_{\text{int}}[\text{S}(^3P_J)] - E_{\text{int}}[\text{CS}(X\,^1\Sigma^+)] \tag{5.2}$$

Here, the $E_{\text{int}}[\text{S}(^3P_J)]$ is the internal energy of the S atom, and $E_{\text{int}}[\text{CS}(X\,^1\Sigma^+)]$ is the internal energy of CS compared to its ground vibronic state CS $X\,^1\Sigma^+, v = 0, J = 0$. For dissociation with a photon energy of 49696.85 cm^{-1} (6.1616 eV), the TKER of CS ($X\,^1\Sigma^+$, $v = 0, J = 0$) + S ($^3P_{J=0,1,2}$) is 1.6108, 1.6328, and 1.6820 eV, respectively. Figure 5.6 (b, d, f) shows the corresponding TKER spectrum. The onsets of

the TKER spectra agree well with the thermochemical thresholds mentioned above, indicating that they are indeed associated with formation of CS ($X\,^1\Sigma^+$, v, J) + S ($^3P_{J=0,1,2}$). The TKER spectra reveal that the photofragments yielded by CS_2 photolysis at 201.22 nm populate the $v = 0 - 10$ vibrational states of CS ($X\,^1\Sigma^+$), with the peak of distribution at $v = 7$.

By instead scanning the VUV sum frequency over the region 105710-105835 cm^{-1}, the PHOFEX spectrum of C ($^3P_{J=0,1,2}$) was recorded as shown in Figure 5.7. The red curve is the spectrum recorded when both UV and VUV were present, while the blue curve is the spectrum when only VUV was introduced into the PD/PI interaction region. Three strong transitions are observed at 105755.9, 105783.0, and 105799.2 cm^{-1}. These three peaks are assigned as $[2s2p^3]\,^3S_1^o - {}^3P_2$, $[2s2p^3]\,^3S_1^o - {}^3P_1$, and $[2s2p^3]\,^3S_1^o - {}^3P_0$ transitions, respectively. The excited state C ($[2s2p^3]\,^3S_1^o$) is above carbon's ionization energy of 11.3 eV. Therefore, it undergoes prompt autoionization to yield C^+. The absence of peaks in the blue curve indicates that the C atomic fragments are generated from the 201.22 nm photodissociation of CS_2, and not the interaction of the VUV laser with CS_2.

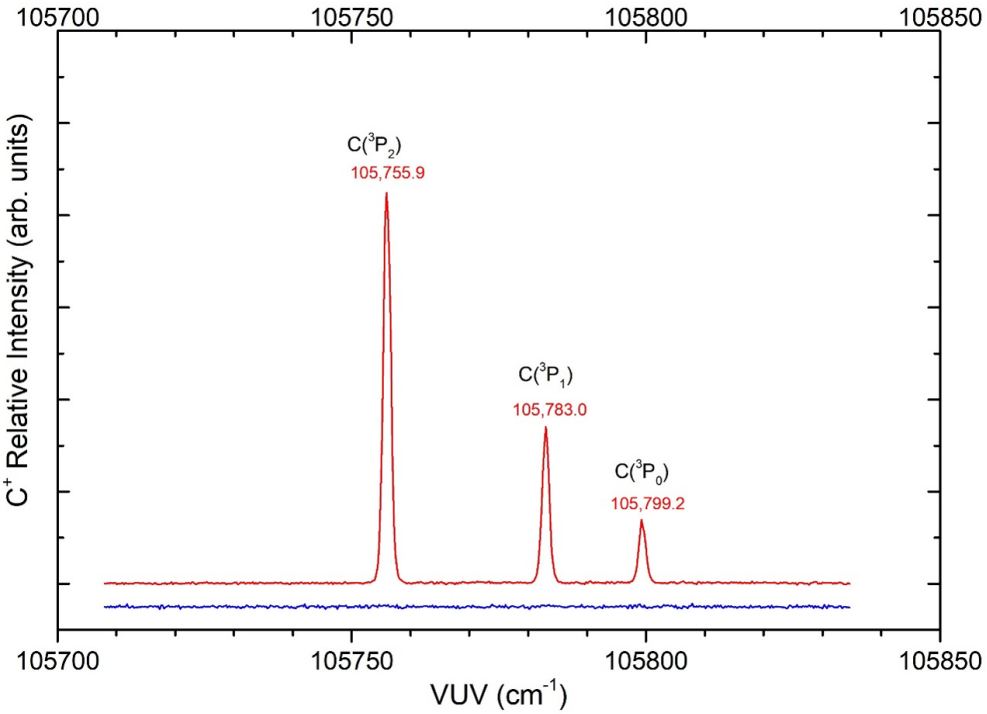

FIGURE 5.7. PHOFEX spectrum of C produced from CS_2 photodissociation at 201.22 nm.

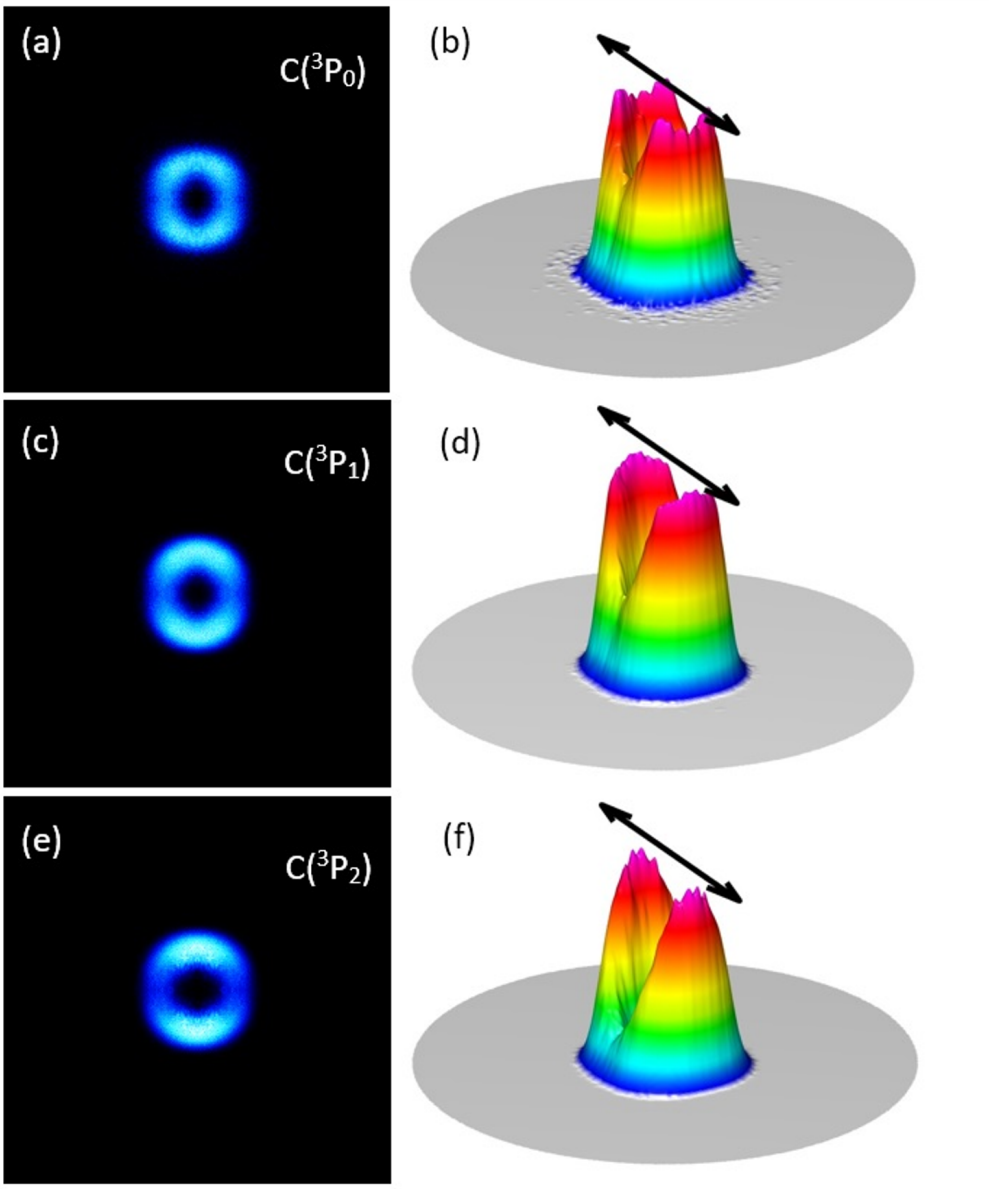

FIGURE 5.8. TS-VMI image and the corresponding 3D image for photofragments of (a,b) C($^3P_0$), (c,d) C($^3P_1$), and (e,f) C($^3P_2$) from CS_2 photodissociation at 201.22 nm.

Figure 5.8 (a, c, e) shows the TS-VMI images of C($^3P_0$), C($^3P_1$), and C($^3P_2$) which were produced by CS_2 photolysis, and in Figure 5.8 (b, d, f) are the corresponding 3D images constructed from the TS-VMI images. The 0 K heats of formation of CS_2 ($X\,^1\Sigma_g^+$), S_2 ($X\,^3\Sigma_u^-$), and C ($^3P_0$) are 1.2013, 7.3710, and 1.3296 eV, respectively (Chase, 1998). The 0 K dissociation threshold of $CS_2\,(X\,^1\Sigma_g^+) \longrightarrow S_2\,(X\,^3\Sigma_u^-)$ + C ($^3P_0$) is $D_0 = 7.4993\,\text{eV} = 60485.90\,\text{cm}^{-1}$, which is greater than the energy of a 201.22 nm photon

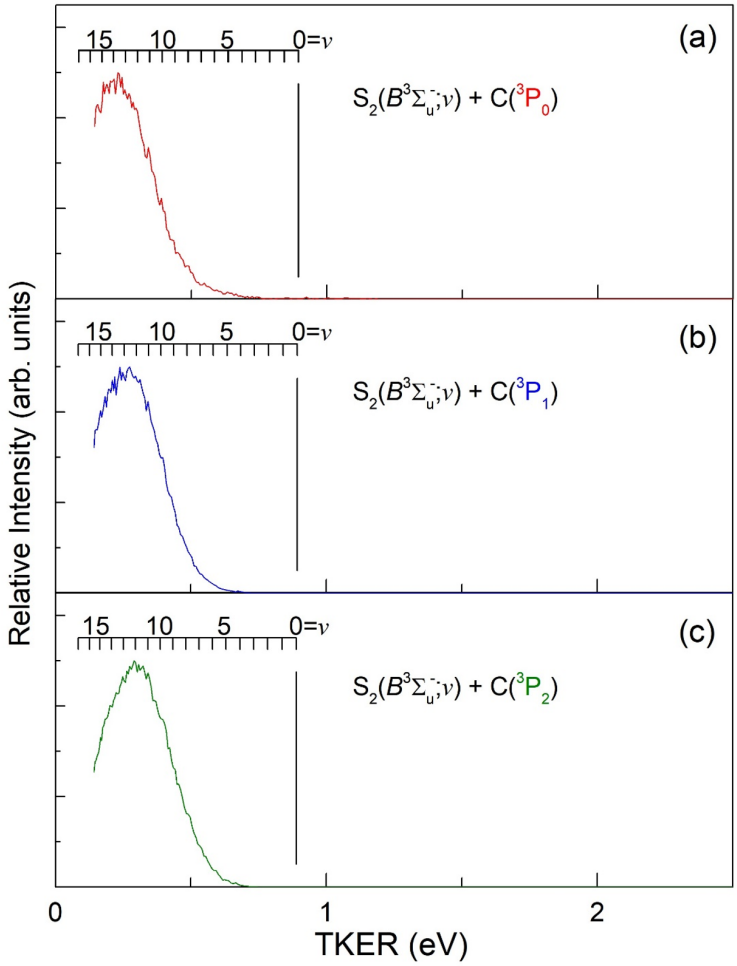

FIGURE 5.9. TKER spectra converted from TS-VMI images of (a) C($^3P_0$), (b) C($^3P_1$), and (c) C($^3P_2$) photofragments from CS_2 photodissociation at 201.22 nm.

(6.1616 eV = 49696.85 cm^{-1}). Therefore, CS_2 photolysis by a single 201.22 nm photon is not feasible. The C atomic fragment must be formed by CS_2 photodissociation after absorbing at least two 201.22 nm photons (E_{2UV} = 12.3232 eV).

The excited state $B\,^3\Sigma_u^-$ of S_2 is about 3.93 eV above its ground state $X\,^3\Sigma_u^-$. In the case that CS_2 is photolyzed by two UV photons, the excited state $B\,^3\Sigma_u^-$ state is energetically accessible in addition to the ground state $X\,^3\Sigma_u^-$. The TKER of these two channels can be calculated by

$$\text{TKER}[S_2(X\,^3\Sigma_u^-) + C(^3P_J)] = 2h\nu(202.22\,\text{nm}) - D_0 - E_{\text{int}}[C(^3P_J)] - E_{\text{int}}[S_2(X\,^3\Sigma_u^-)] \tag{5.3}$$

$$\text{TKER}[S_2(B\,^3\Sigma_u^-) + C(^3P_J)] = 2h\nu(202.22\,\text{nm}) - D_0 - E_{\text{int}}[C(^3P_J)] - E_{\text{int}}[S_2(B\,^3\Sigma_u^-)] \tag{5.4}$$

Here, the $E_{\rm int}[{\rm C}(^3P_J)]$ is the internal energy of the C atom, and $E_{\rm int}[{\rm S_2}(X\,^3\Sigma_u^-)]$ and $E_{\rm int}[{\rm S_2}(B\,^3\Sigma_u^-)]$ are the internal energies of S_2 compared to its ground rovibronic state $S_2\ X\,^3\Sigma_u^-, v = 0, J = 0$. Figure 5.9 shows the TKER spectra that are converted from the TS-VMI images of $C(^3P_0)$, $C(^3P_1)$, and $C(^3P_2)$. The TKER peaks do not match with the formation of $S_2\ (X\,^3\Sigma_u^-, v) + C\ (^3P_{J=0,1,2})$. The calculated TKER values for $S_2\ (B\,^3\Sigma_u^-, v = 0, J = 0) + C\ (^3P_{J=0,1,2})$ are 0.8950, 0.8930, and 0.8896 eV, respectively. The onsets for formation of $S_2\ (B\,^3\Sigma_u^-, v = 0 - 17) + C\ (^3P_{J=0,1,2})$ are marked in Figure 5.9.

In summary, besides the $CS\ (X\,^1\Sigma^+) + S\ (^3P)$ channel, we observed the $S_2\ (B\,^3\Sigma_u^-) + C\ (^3P)$ channel in CS_2 photodissociation at 201.22 nm. To study the formation mechanics of $S_2 + C$, several further experiments are proposed. The photodissociation threshold of $CS_2\ (X\,^1\Sigma_g^+) \longrightarrow S_2\ (B\,^3\Sigma_u^-) + C\ (^3P)$ is 11.43 eV (108.5 nm). By recording the VMI images and TKER spectra of CS_2 photodissociation via one-photon VUV excitation with energies above 11.43 eV, we can verify if the results are consistent with the finding above. Although 11.43 eV is already larger than the photoionization threshold of CS_2 at 10.1 eV (123 nm), the photodissociation cross section in this range is still much higher than the photoionization cross section (Heays et al., 2017). Unlike Li et al. (2021), We did not observe the $S_2\ (X\,^3\Sigma_u^-) + C\ (^3P)$ channel in our experiments. We plan to tune one VUV laser to 7.50 eV (165 nm) and search for the C^+ signal corresponding to formation of S_2 in $X\,^3\Sigma_u^-$ states. Alternatively, photodissociation of CS_2 by a two-photon excitation using a UV laser with an energy around 3.75 eV (330 nm) is possible. There are at least 67 emission bands in the range of 300-330 nm (Jackson & Scodinu, 2004). CS_2 can be photolyzed via a (1+1) or (1+1') resonance-enhanced multiphoton dissociation using one of these bands as the resonant frequency.

5.3.2. A Preliminary Spectrum of CS $C - X$ (0-0) and/or (1-1) bands.

The VUV-VUV-VMI setup was also used to look for potential CS $C\,^1\Sigma^+ - X\,^1\Sigma^+$ electronic transition signals around 140.1 nm, which was reported by Stark et al. (1987). Both VUV lasers were aligned to cross with the molecular beam in the PD/PI interaction region. By fixing the frequency of the first VUV laser (VUV-1) at $\omega_1 = 44930.1\,{\rm cm}^{-1}$, and scanning ω_2 from 18018 to $18690\,{\rm cm}^{-1}$, VUV light was produced at the difference frequency $(2\omega_1 - \omega_2)$ from 71169 to $71842\,{\rm cm}^{-1}$ and at the sum frequency $(2\omega_1 + \omega_2)$ from 108552 to $107878\,{\rm cm}^{-1}$ using Xe gas as nonlinear medium. The sum frequency output of second VUV laser (VUV-2) was tuned to $105756\,{\rm cm}^{-1}$ (94.557 nm), which corresponds to the $C[2s2p^3\ (^3S_1^o)] \leftarrow C[2s^22p^2\ (^3P_2)]$ transition. The C atom was then ionized to form C^+ through autoionization and was recorded by TOF or TS-VMI.

A molecular beam of CS_2 seeded in the carrier gas N_2 was introduced into the PD/PI interaction region through two skimmers. The two VUV lasers were then applied in sequence separated by 15 ns, yielding a C^+ signal. In this experiment, we propose the following pathway for the generation of C^+:

$$CS_2 \xrightarrow{\text{VUV}-1} CS + S \tag{5.5a}$$

$$CS \xrightarrow{\text{VUV}-1} C + S \tag{5.5b}$$

$$C \xrightarrow{\text{VUV}-2} C^+ + e^- \tag{5.5c}$$

The amount of CS generated in step 5.5a should be proportional to the product of the VUV-1 intensity and the photodissociation efficiency of CS_2. If the latter is about a constant in this frequency range, then the CS produced is directly related to the VUV-1 intensity, which can be monitored by the signal of $CS_2{}^+$ in the TOF spectra. Because the VUV-2 frequency and intensity are fixed, the signal of C^+ observed is proportional to the amount of atomic C generated in step 5.5b, which in turn reflects the rovibrational cross sections of the CS $C - X$ band.

The TOF spectra obtained under different experimental conditions are shown in Figure 5.10 left. When only VUV-2 was present(yellow line), a small peak of C^+ signal was observed due to a complicated multi-step process done by just VUV-2, including photodissociation of CS_2, then photodissociation of CS followed by photoionization of C atom. On the other hand, no C^+ signal was observed when only VUV-1 was present (not shown in the figure), since the photoionization cross section of C is very small in the VUV-1 sum frequency range. When VUV-1 was applied at 15 ns before VUV-2 but without Xe gas, (i.e., ω_1 and ω_2 were present but no VUV-1 sum frequency or difference frequency were generated), the C^+ signal was enhanced (blue line), indicating that the ω_1 of VUV-1 itself enhanced the photodissociation of CS_2 and produced more CS in the interaction region, which was then photoionized by VUV-2. When the VUV-1 sum frequency and difference frequency were generated by introducing the Xe gas (red line), a higher C^+ peak was recorded, showing additional CS production (and therefore C production). The difference of the red and blue lines indicates the contribution of step 5.5a from the actual VUV-1.

Figure 5.10 (right) shows the C^+ signal at different VUV-1/VUV-2 delay times. When both VUV lasers arrive to the PD/PI interaction region at the same time (blue curve), the fragments generated by VUV-1 are not exposed to VUV-2, thus there was no enhancement observed. When the delay time was increased to

30 ns, the enhancement decreased, possibly due to the diffusion of fragments generated by VUV-1. The optimized delay time 15 ns (red line) was used in the following experiments.

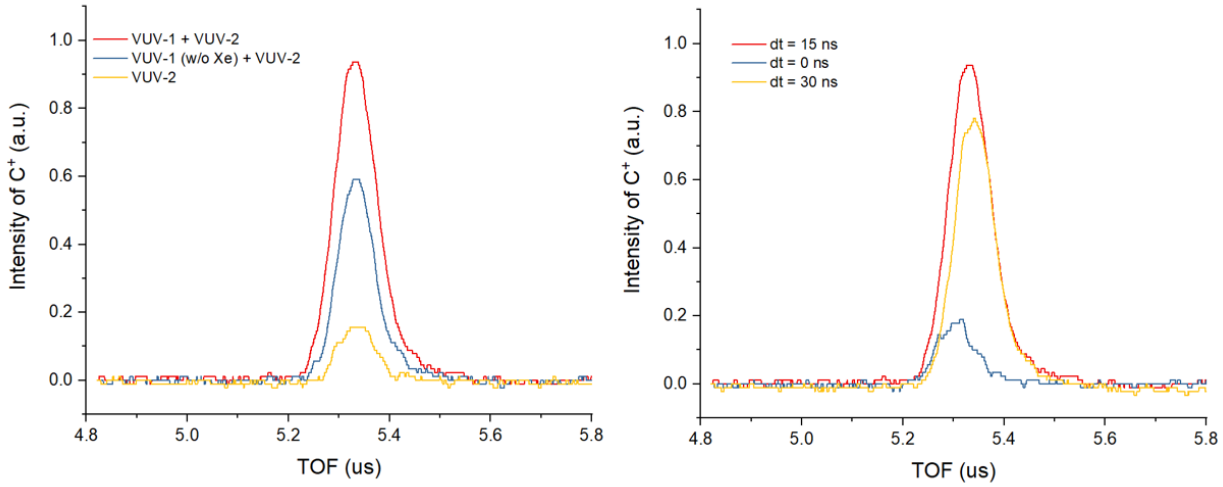

FIGURE 5.10. left: TOF spectra of C^+ when only VUV-2 existed, and VUV-1 (with and without Xe gas) existed in addition to VUV-2 laser. right: When both VUV-1 and VUV-2 existed, TOF spectra of C^+ recorded at delay times of VUV-2 compared to VUV-1.

The result of scanning the VUV-1 ω_2 between 18018 to 18690 cm^{-1} is shown in Figure 5.11. The intensity of the VUV laser which is represented by the CS_2^+ signal (average of two scans) is shown in the top subfigure, while the C^+ signal (average of three scans) is shown in the middle subfigure. The normalized C^+ signal calculated as the ratio of these two curves is shown in the bottom subfigure. A peak with a shape similar to P and R branches was observed around ω_2 =18455 cm^{-1}. The signal depends on both VUV-1 and VUV-2 lasers, thus it is highly likely to reveal electronic transitions of CS. The signal-to-noise ratio of the peak is too low to make a confident assignment. Two Pgogher simulations of the CS $C\,^1\Sigma^+ - X\,^1\Sigma^+$ band are shown in Figure 5.12. The band origin positions were set to 71327 and 71480 cm^{-1}, which were reported as (0-0) and (1-1) band heads , respectively, by Donovan et al. (1970). Rotational constants of all four vibrational states ($v = 0, 1$ of $C\,^1\Sigma^+$ and $X\,^1\Sigma^+$ states) are set to 0.82 cm^{-1}, which is suggested by our calculation in Chapter 3. The linewidth is assumed to be 1 cm^{-1} with a Lorentzian shape, and the rotational temperature is set to 50 K and 800 K in the two simulations. For convenience, the populations of the $v = 0$ and $v = 1$ vibrational states are set to equal.

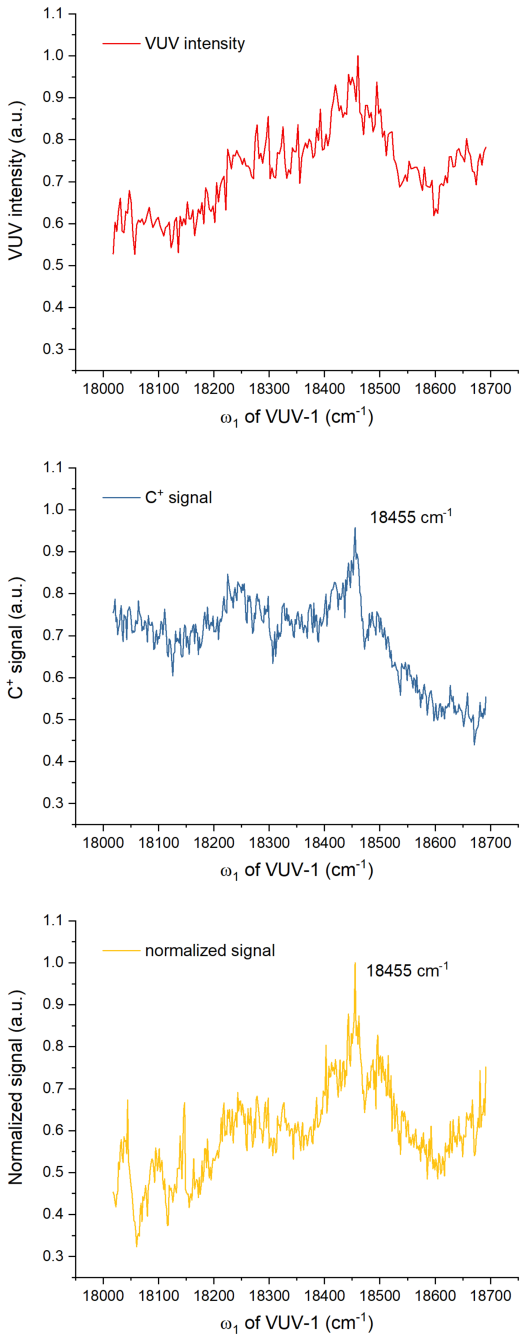

FIGURE 5.11. Top: VUV intensity of VUV-1. Middle: C^+ signal of VUV-VUV-TOF experiment. Bottom: Normalized C^+ signal (middle curve divided by top curve).

It can be noticed that the observed signal is between the reported (0-0) and (1-1) bands. If the peak is actually an individual vibronic band, then the rotational temperature needs to be $\gtrsim 800\,\mathrm{K}$ to reproduce

the width of the P and R branches. Alternatively, it is possible that the structure observed is the result of several $(v' - v'')\ \Delta v = 0$ bands and $\Delta v = -1$ bands Previous experiments and our calculations suggest that the $C\ ^1\Sigma^+$ state has a fundamental vibration frequency about 100 cm^{-1} higher than that of the ground X state. So potentially one or several $(v' - v'')\ \Delta v = -1$ bands could appear in this frequency range. If the potential energy curve of diabatic $C\ ^1\Sigma^+$ state deviates from a harmonic potential curve faster than ground X state, then the frequencies of $(v' - v'')\ \Delta v = 0$ transitions first increase and then decrease as v increases. Thus one or several $(v' - v'')\ \Delta v = 0$ bands for high v numbers could also show in this range. We were unable to verify the vibrational distribution of CS generated in this experimental configuration, but it is likely that the generated CS has a hot vibrational and rotational temperature as observed when CS_2 was photodissociated at 201.22 nm in the PD/PI interaction region. The observed structure could potentially be explained as overlap among several transitions arising from high v states of the CS ground $X\ ^1\Sigma^+$ state.

Further higher signal-to-noise ratio spectroscopy studies are needed to validate this observation. Also, cooling CS to lower vibrational states could simplify the spectrum and enhance the signal from lower rovibrational states. Efforts to cool CS are discussed in the next subsection.

5.3.3. Photodissociation of CS_2 before skimmers.

From the above experiments described in Section 5.3.1 we verified that the UV 201.22 nm laser is able to generate CS + S in the PD/PI region and that the CS is produced in higher vibrational levels. However, CS generated directly in PD/PI region has kinetic energy in all directions, making it difficult for further VMI studies. Ideally, CS needs to be generated in the source chamber and enter into the PD/PI region through two skimmers so that CS has no kinetic energy except along the center axis of the apparatus. Another benefit of doing this is that collisions with carrier gas could relax the CS molecule to its vibrational ground v=0 state.

In an effort to accomplish this, we aligned the UV 201.22 nm laser at the E-L valve outlet position and aligned the two VUV lasers in the PD/PI region. The time delay between the UV 201.22 nm laser and the VUV-1 laser was optimized to be about 393 μs. The TOF spectra obtained are shown in Figure 5.13. When only the UV 201.22 nm laser was turned on, no signals were observed (yellow line), as the energy of UV photon is not enough to ionize CS_2 or its photodissociation products. When both VUV lasers were present, C^+, S^+, CS^+, and $CS_2{}^+$ signals were all detected (red line). Those products were generated by photodissociation and photoionization of CS_2 in the PD/PI interaction region. However, when the UV 201.22 nm laser was added, all signals of C^+, CS^+, and $CS_2{}^+$ decreased by a similar ratio (blue line). This

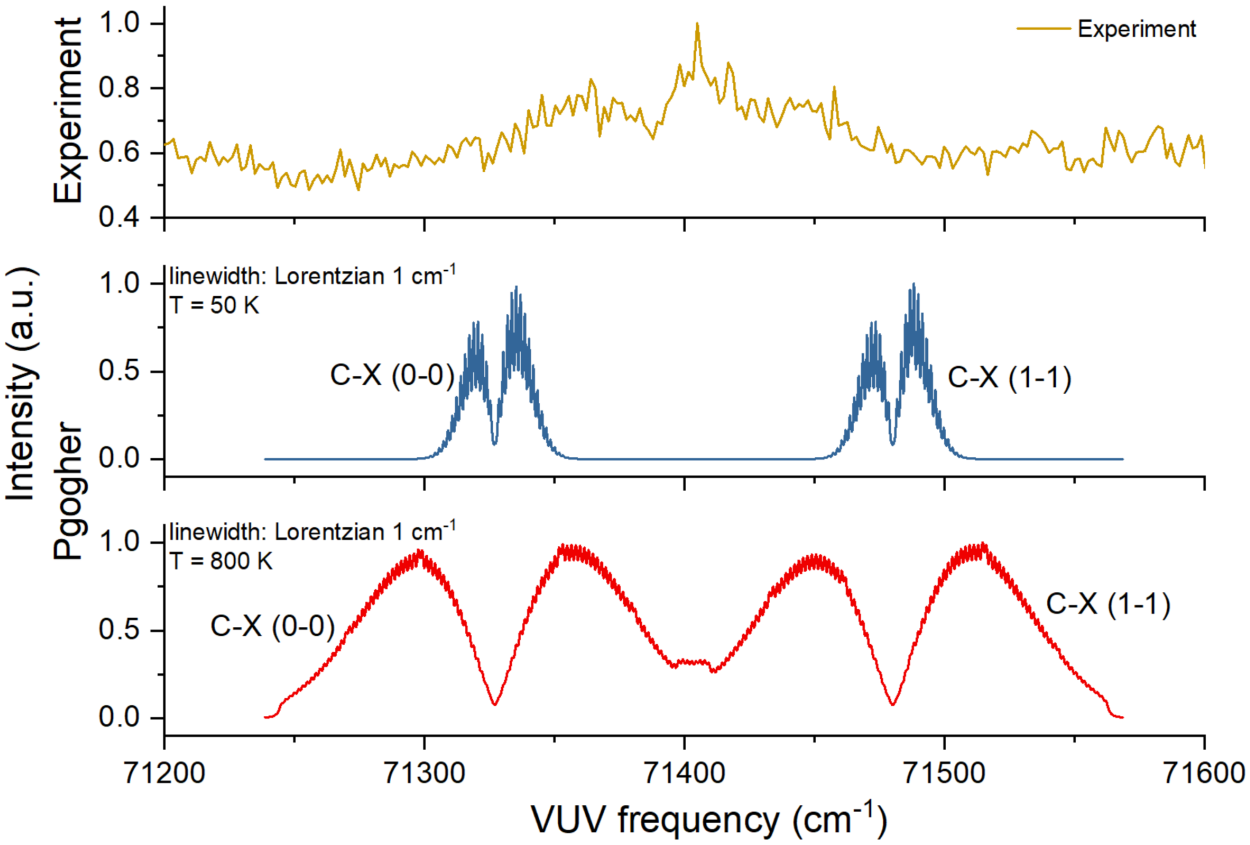

FIGURE 5.12. Experimental spectrum (up) and simulated CS $C\,^1\Sigma^+ - X\,^1\Sigma^+$ (0-0) and (1-1) bands at 50 K (middle) and 800 K (bottom).

indicates the amount of CS_2 entering the PD/PI interaction region decreased, and the CS and S fragments generated from photodissociation of CS_2 did not arrive into the PD/PI interaction region.

To further understand the results of the TOF spectra, in a subsequent UV-VUV-VMI experiment, the UV 201.22 nm laser was aligned to the exit of E-L valve. The VUV laser was tuned to 70174.36 cm^{-1} to selectively probe S($^3P_2$) and was aligned to cross the molecular beam in the PD/PI interaction region, yielding a detection of S^+ with TS-VMI. Figure 5.14 shows the TS-VMIs of S($^3P_2$) when (a) only the VUV laser, (b) both UV 201.22 nm and VUV lasers, and (3) only the UV 201.22 nm laser was/were turned on. The corresponding 3D images constructed from (a) and (b) are shown in Figure 5.14 (d) and (e). When only the UV 201.22 nm laser was turned on, S generated by photodissociation of CS_2 was unable to be ionized, thus no signal was recorded in TS-VMI. When only the VUV laser was turned on, a diffuse ring was observed in TS-VMI, giving information about the kinetic energy distribution of S atoms produced by VUV

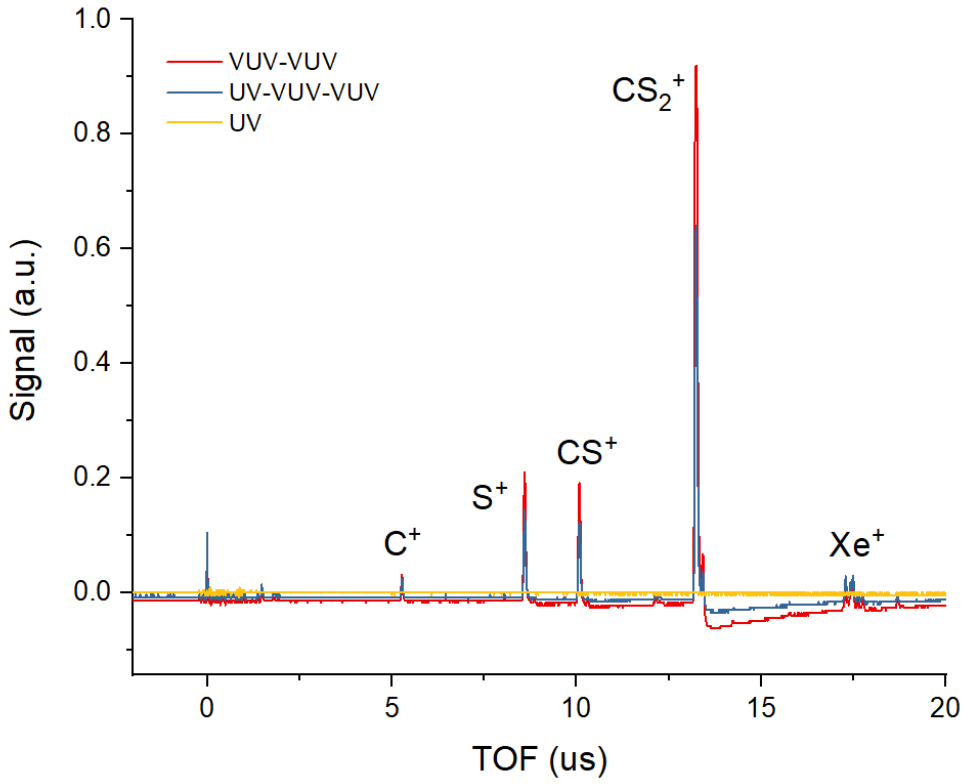

FIGURE 5.13. TOF spectra of CS_2 photodissociation products with VUV-VUV, UV-VUV-VUV, and UV only.

photodissociation of CS_2. When both UV 201.22 nm and VUV lasers were turned on, a dot was observed in the center of VMI signal (Figure 5.14 (b)). This is attributed to S atoms generated in the source chamber by the UV 201.22 nm laser being photoionized by the VUV laser in the PD/PI interaction region. The S atoms therefore only carried kinetic energy along the center axis of the apparatus, going rise to an S^+ signal with almost no transverse kinetic energy. The diffuse ring signal in Figure 5.14 (b) arises from CS_2 which was not photolyzed by UV 201.22 nm, and instead was dissociated in the interaction region as in Figure 5.14 (a).

From the TS-VMI images, we were able to see that some S atom generated by photodissociation of CS_2 arrived to the PD/PI interaction region. Since CS is heavier than S, it carries less velocity compared with S upon CS_2 photodissociation and should also reach the interaction region. However, as shown by TOF spectra, the total amount of CS^+ and S^+ decreased when the UV 201.22 nm laser was turned on, which indicates the main contribution of the S^+ and CS^+ signal was from the photodissociation of VUV in the PD/PI interaction region. This shows two new difficult problems. First, CS_2 is easy to photolyzed, thus the existence of CS_2

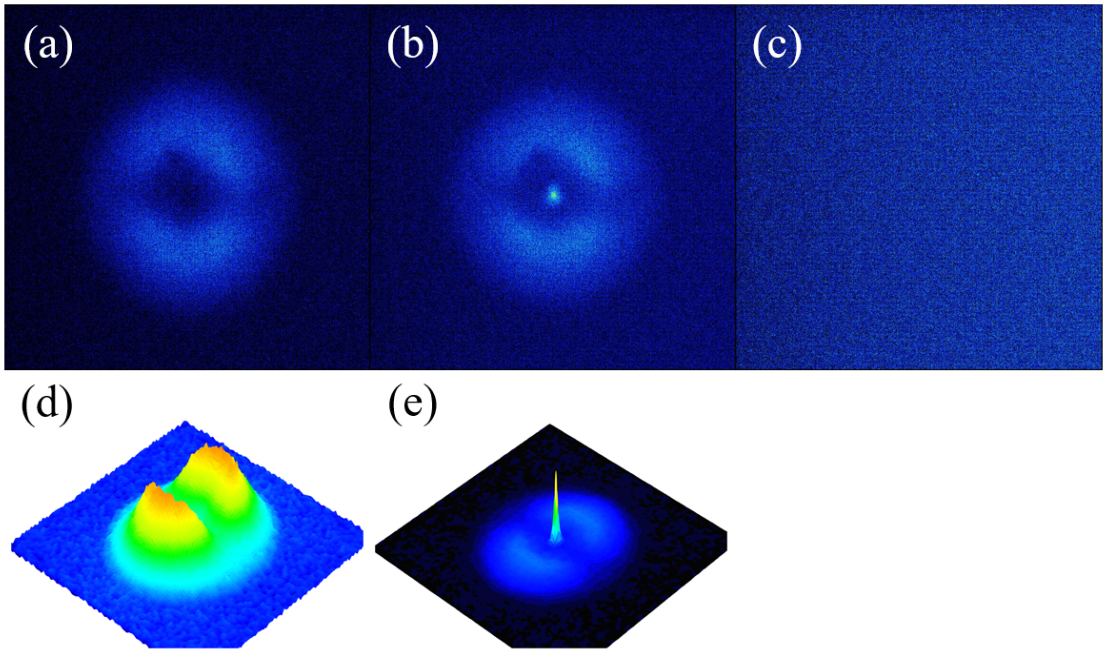

FIGURE 5.14. TS-VMIs and corresponding 3D images for S($^3P_0$) when (a,d) only VUV laser, (b,e) both UV 201.22 nm and VUV laser, and (c) only UV 201.22 nm was/were turned on.

in the PD/PI interaction region would interact with VUV lasers to produce unwanted CS, S, and even C, which appear on our desired m/z values in the TOF spectra. Second, though a large amount of CS_2 was photolyzed by the UV 201.22 nm laser in the source chamber, only a small percentage of S and CS entered the interaction region. A higher amount of CS is required to achieve a good signal-to-noise spectrum.

In another attempt, a Teflon tube with a side hole was attached to the E-L valve. This was inspired by a study of the reaction of $CH_3NH + O(^1D)$, in which gas mixture including O_3 was photolyzed in a 3 cm long quartz tube with a 1 mm inner diameter prior to supersonic expansion into a vacuum chamber (Bunn et al., 2020). In our setup, the UV 201.22 nm laser was introduced through the side hole to photolyze CS_2. The CS generated is able to cool to lower vibrational states through collisions with carrier gas in the short tube before the supersonic expansion. However, we were unable to observe a stable signal from the molecular beam in the interaction region even the UV 201.22 nm laser was not firing. It is possible a better understanding of the supersonic expansion dynamics is required to solve the problem.

5.4. Summary and perspectives

First, we have studied the photodissociation of CS_2 by UV 201.22 nm laser. Based on the TS-VMI iamges obtained, we observed both CS + S and S_2 + C dissociation channels in our experiments. The CS generated populates several vibrational states and the distribution peak is at $v = 7$. The S_2 + C photodissociation channel was verified independent from the study done by Li et al. (2021). The observation of this channel may provide new insight into the origin of the large abundance of S_2 in comets.

Several attempts to study the photodissociation of CS were made using the UV-VUV-VUV-VMI apparatus. However, we found in our experimental setup, the CS generated in source chamber was unable to enter PD/PI interaction region successfully. CS_2 is a good precursor to generate CS, however, the remaining CS_2 in the system interacts with VUV lasers and provides a large background signal of CS and S. There are several possible future directions: first, by replacing the Teflon tube with a fused silica tube without side holes, it is possible that the supersonic expansion dynamics would allow the molecular beam to enter the PD/PI interaction region successfully. Changing the CS_2 photodissociation laser from the third harmonic output of a dye laser to an ArF excimer laser would provide more UV photons, leading to a larger dissociation efficiency of CS_2. Also, an electrical discharge of CS_2 can be a potential method to generate CS. Ultimately, delivery of rovibrationally cool CS into the PD/PI interaction region will enable VUV-VUV-VMI studies of state-selective CS photodissociation.

CHAPTER 6

Generation of C_2 From Laser Ablation and New Measurement of Ionization Energy of C_3

6.1. Introduction

6.1.1. Photodissociation of C_2.

A short overview of the research history about C_2 and the motivation to study its photodissociation, especially via the $F\,^1\Pi_u - X\,^1\Sigma_g^+$ band, is presented in Chapter 4.1. Dicarbon (C_2) is of great interest to both quantum chemists and experimental chemists. It is well known that multi-reference theoretical methods must be used to calculate its ground $X\,^1\Sigma_g^+$ state accurately, due to the quasi-degeneracy of its $2\,\sigma_u^*$, $1\,\pi_u$, and $3\,\sigma_g$ molecular orbitals. Several low lying excited states have similar energies, leading to abundant perturbations among them. Thus C_2 has a spectrum with rich structures. Many theoretical and experimental studies have been done on those low-lying excited states, and their transitions. Recently, with the aid of high accuracy quantum chemical calculations, Schmidt and his colleagues successfully obtained high resolution spectra of several new electronic states (Kokkin et al., 2006; Krechkivska et al., 2015, 2017). However, the $F\,^1\Pi_u$, $f\,^3\Sigma_u^-$, and $g\,^3\Delta_g$ states, which are about 9 eV above the ground $X\,^1\Sigma_g^+$ state, have not been studied again since they were first measured in 1969 (Herzberg et al., 1969).

C_2 is widely detected in a variety of diffuse clouds (Cecchi-Pestellini & Dalgarno, 2002; Chaffee et al., 1980; Hupe et al., 2012; Lambert et al., 1995; Snow, 1978; van Dishoeck & Black, 1982) and comets (Jackson, 1976; Johnson et al., 1983; Stockhausen & Osterbrock, 1965). In diffuse clouds, C_2 is formed following a series of reactions starting with $C^+ + CH \longrightarrow C_2{}^+ + H$ and ending with the dissociative recombination of CH_2H^+. Photodissociation is one of its main destruction pathways. Astronomical detection of C_2 is mainly through its $D\,^1\Sigma_u^+ - X\,^1\Sigma_g^+$ and $A\,^1\Pi_u - X\,^1\Sigma_g^+$ transitions since pure rotational and vibrational transitions are forbidden. The $F\,^1\Pi_u - X\,^1\Sigma_g^+$ band has been detected in several diffuse clouds. However, the low-J values covered by the astronomical observations appear to show frequency perturbations relative to their expected

positions derived from the higher-J measurements of Herzberg et al. (1969) (Hupe et al., 2012). The nature of these perturbations and their implications for C_2 photodissociation in space remain unclear.

The photodissociation energy threshold for C_2 is 193 nm (6.42 eV). Among all 19 known excited states, $F\,^1\Pi_u$ is the only electronic state that lies above the photodissociation threshold and can be reached directly from the ground state by single photon excitation. Thus theoretical and experimental studies on the $F\,^1\Pi_u$ state and the $F\,^1\Pi_u - X\,^1\Sigma_g^+$ transition are important for modeling C_2 photodissociation in space. The only experimental spectrum of the $F\,^1\Pi_u - X\,^1\Sigma_g^+$ transition is the one obtained by Herzberg et al. (1969), and its frequency and intensity accuracy are limited. Also, the low-J lines are not distinguished due to the low resolution of the spectrum. A further theoretical study firmly established that the electronic character of $F\,^1\Pi_u$ is a Rydberg state with the configuration $[\sigma_u^2\pi_u^3 3s]$ (Bruna & Grein, 2001). In Chapter 4, MRCI+Q/aug-cc-pV5Z+R potential energy curves were calculated for the excited electronic states of C_2, including $F\,^1\Pi_u$ and and a coupled-channel model has been built to study C_2 predissociation focusing on this state.

The objective of the work presented in this chapter is to use the vacuum UV laser pump-probe velocity-map imaging (VUV-VUV-VMI) apparatus described in chapter 5 to study the $F\,^1\Pi_u - X\,^1\Sigma_g^+$ band experimentally. like CS, C_2 is a transient molecule and therefore must be produced and manipulated in the vacuum chamber directly. Methods previously used to produce C_2 include electrical discharge of acetylene (C_2H_2) (Krechkivska et al., 2018) and toluene ($C_6H_5CH_3$) (Krechkivska et al., 2016), two-step photolysis of acetylene (C_2H_2) at 193 nm (Sorkhabi et al., 1997), reactions between atomic fluorine (F) and methane (CH_4) in a flow-tube reactor (Harper et al., 2020), and laser ablation of a graphite rod (Belau et al., 2007). The electrical discharge of acetylene (C_2H_2) is most widely used in previous studies to produce C_2 due to its simple but reliable design. However, one of the disadvantages of this method is that a variety of possible byproducts C_xH_y are also generated. Although these are easily distinguishable by direct spectroscopic measurements, in the VUV-VUV-VMI apparatus, these byproducts are likely to be photolyzed by the high energy of the VUV laser and interfere with the TOF-MS (time-of-flight mass spectrometry) and VMI detection methods. For this reason, the laser ablation method is preferred in our experimental design. With the use of a deflection plate to block ions, the output of a laser ablation source only consists of carbon atoms and carbon clusters C_x ($x \geqslant 2$). The C^+ patterns generated from C_x ($x \geqslant 3$) in the VMI can be readily distinguished from those generated from C_2.

The first step of the experiments is to verify that C_2 is able to be generated successfully. In the current setup of the VUV-VUV-VMI apparatus, the gas source is a pulsed E-L valve. It is not straightforward to replace it with a laser ablation source. Thus, we carried experiments to test the production of C_2 in another apparatus equipped with such a source and verified the C_2 can be produced by laser ablation successfully. The future plan of the experiment is to build a similar laser ablation chamber and incorporate it into the VUV-VUV-VMI apparatus.

6.1.2. Photoionization of C_3.

C_3 is an unstable linear molecule with a ground $\tilde{X}\,^1\Sigma_g^+$ state. In space, it was first detected in Comet b 1881 through its $\tilde{A}\,^1\Pi_u - \tilde{X}\,^1\Sigma_g^+$ band (Huggins, 1882), although its identity was unknown at the time. C_3 has also been detected in different astronomical environments, including circumstellar shells of carbon stars (Cernicharo et al., 2000; Mookerjea et al., 2010; Roueff et al., 2002), molecular clouds (Cox & Patat, 2014; Maier et al., 2001; Roueff et al., 2002), and comets (Cernicharo et al., 2000). C_3 is believed to be one of the key molecules to the formation of more complex carbon clusters, long-chain cyanopolyynes, and polycyclic aromatic hydrocarbons (Van Orden & Saykally, 1998). Also, it plays an important role in combustion processes and hot carbon vapour (Varandas & Rocha, 2018).

Experimental studies of photodissociation and photoionization of C_3 are also challenging because it is unstable (Heays et al., 2017). A review of early spectroscopic studies on C_3 has been given by Van Orden & Saykally (1998) including low-lying states and several states in the UV region. The assignments of the bands in the UV region are still difficult even with the aid of theoretical calculations. In 2008, van Hemert & van Dishoeck (2008) calculated the vertical excitation energies and oscillator strengths for absorption from the ground $\tilde{X}\,^1\Sigma_g^+$ state to five highly excited states above the photodissociation threshold, which is calculated as about 4.6 eV.

Previous photoionization studies on C_3 give a range of IE values and have not yet firmly established cross sections. IE values have been reported as 13.0±0.1 eV (Ramanathan et al., 1993) and 9.98-11.61 eV (Rohlfing et al., 1984), and appearance energy values as 11.1±0.5 eV (Gupta & Gingerich, 1979), 12.1±0.3 eV (Kohl & Stearns, 1970), and 12.6±0.6 eV (Drowart et al., 1959). Early theoretical calculations suggest that the ground state of C_3^+ is a $^2B_2$ state with a bent structure (Fura et al., 2002; Orlova & Goddard, 2002) instead of the linear $\tilde{X}\,^2\Sigma_u^+$ state. In 2006, Nicolas et al. (2006) recorded the photoionization efficiency (PIE) curves using the Advanced Light Source (ALS) as a tunable VUV source. The experimental results suggested an

11.70±0.05 eV difference between the C_3 ($\tilde{X}\,^1\Sigma_g^+$) and the C_3^+ ($\tilde{X}\,^2\Sigma_u^+$) vibronic ground states. They also carried out a CASSCF-MRCI/cc-pVQZ calculation and found that the $\tilde{X}\,^2\Sigma_u^+$ state is 0.09±0.02 eV above the global $^2B_2$ minimum and another $^2A_1$ minimum with a similar energy as the $^2B_2$ state. Complemented by the *ab initio* calculations, they determined the ionization energy as 11.61±0.07 eV between the neutral and ionic ground states. This is the only recent experiment regarding the photoionization of C_3. The photodissociation and photoionization rates in space are estimated with a uncertainty of 10 in astrochemical models (Heays et al., 2017).

However, the low spectra resolution of the ALS measurement (Nicolas et al., 2006) precluded the detection of vibrational structures and limited the precision of the derived PIE. A higher resolution study is therefore needed to refine the ionization energy measurement. In our experimental setup, we observed generation of C_3 alongside C_2 in the output of the laser ablation source. Then, we combined the VUV laser with the pulse field ionization-photoion (PFI-PI) technique to measure the ionization energy as 11.8341±0.0025 eV between the C_3 $\tilde{X}\,^1\Sigma_g^+$ and the C_3^+ $\tilde{X}\,^2\Sigma_u^+$ states.

6.2. Experiment

The setup of PFI-PI apparatus was described in detail previously (Chang et al., 2019a, 2012, 2019b). As shown in Figure 6.1, the apparatus consists of a supersonically cooled laser ablation beam source for the preparation of C_x ($x \geqslant 2$), a VUV laser for photoexcitation and photoionization, and a TOF electron spectrometer for PFI–PE detection.

A modified Smalley-type (Dietz et al., 1981) laser ablation beam source was used to produce carbon clusters. The design of this laser ablation source has been detailed by Chang et al. (2009) and Reed et al. (2009). The second harmonic output (532 nm) of a Nd:YAG laser operated at 30 Hz iss used to ablate a rotating graphite rod, which is translated vertically to ensure a fresh sample is ablated on each laser pulse. The ablation products are entrained in the pulsed buffer gas (He) and flow through a skimmer into the interaction region. High voltage is applied to a deflection plate located before the skimmer to block any ions generated from the laser ablation. The sample is then cooled by a the supersonic expansion when it exits the capillary.

In the interaction region, the molecular beam intersects a tunable VUV laser generated by four-wave mixing (Chapter 5.2). In the PIE mode of the apparatus, when the VUV energy is higher than the IE of the

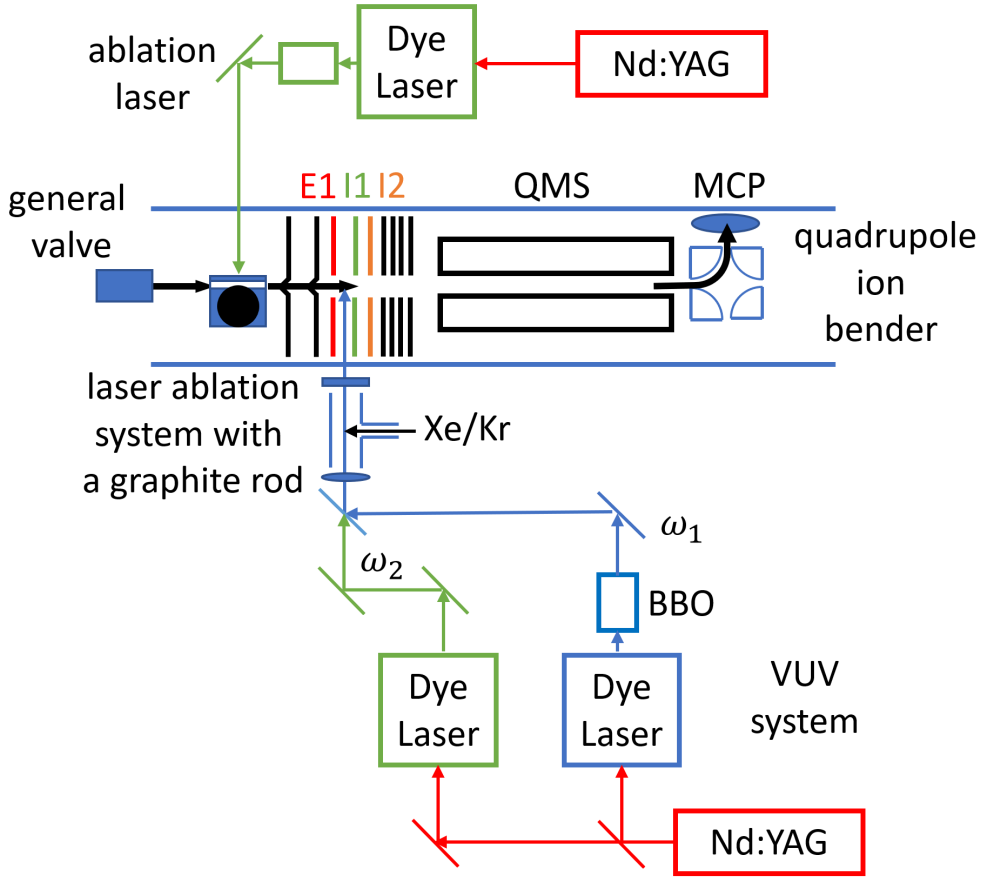

FIGURE 6.1. Schematic diagram of the VUV laser PFI-PI apparatus.

species C_3, C_3^+ is generated and guided by ion optics into the MCP detector. In the PFI-PI mode of the apparatus, a sequential electric field pulse scheme generated by three ion lenses, E1, I1, and I2, is applied after the VUV laser interacts with the molecular beam. Between E1 and I1, an electric field F_R with amplitude 4.0 V/cm and duration 3.5 μs is applied, followed by F_{PFI} with amplitude 75.0 V/cm and duration 0.7 μs. The small F_R electric field slows any "prompt ion" generated by the direct interaction between molecular beam and the VUV laser. C_3 molecules excited by the VUV laser into high Rydberg states are ionized by the Stark field F_{PFI} to form C_3^+ "PFI-PI" ions, which are pushed in the direction of ion lens I2. The voltage applied to I2 creates a potential energy barrier that blocks all prompt ions. If the VUV photon energy is too small, then the C_3 promoted into excited states cannot be ionized and remain in the form of neutral molecules. If the VUV photon energy is too large, then the C_3 molecules in excited states autoionize to form prompt ions and are blocked by the I2 ion lens. Only when the VUV photon energy is similar to the IE threshold

are C_3 molecules excited into Rydberg states with large n that may be ionized by the Stark field. The C_3^+ ions are then counted by TOF-MS. Further details about the PFI-PI technique are presented in Chang et al. (2019a).

6.3. Results and discussion

6.3.1. Generation of C_2 and C_3.

To identify products of laser ablation, the VUV sum-frequency energy was tuned to 13.119 eV, and the TOF spectrum was recorded when the laser ablation laser was on and off. The calibrated spectra are shown in Figure 6.2. When the laser ablation was off, residual air in the chamber and Xe gas leaking from the four-wave mixing chamber were ionized by the VUV laser, as indicated by their corresponding ions in the TOF spectrum. The intensities of the peaks H_2O^+, N_2^+, and O_2^+ gradually decay over a period of days after the whole system opens and pumps to vacuum. When the laser ablation was on, new peaks appeared around m/z =12, 24, and 36, which are assigned as C^+, C_2^+, and C_3^+. Tiny peaks were also observed at m/z =48 and 60, which are C_4^+, and C_5^+. The new peaks of carbon clusters show that neutral carbon atoms and carbon clusters were generated by laser ablation successfully.

6.3.2. Photoionization energy of C_3.

In the PIE mode of the apparatus,the VUV sum frequency was scanned over the range 11.77-11.87 eV with a step size of 0.0003 eV, and the photon ionization efficiency spectrum of the C_3^+ was recorded. The results are shown as the black curve in Figure 6.3. The curve began to increase around 11.81 eV, rapidly increased around 11.83 eV, and reached a local maximum around 11.835 eV. The photoionization energy lies in this range. A point fitting procedure to extrapolate the range with largest slope can give rise to an estimated ionization energy. This is the method used in previous C_3 ionization studies (Nicolas et al., 2006).

To more accurately determine the PIE, the apparatus was switched to PFI-PI mode, and the VUV sum frequency energy was scanned over 11.81-11.87 eV with a step size of 0.00014 eV. The results are shown as the blue curve in Figure 6.3. A single peak appeared in the PFI-PI spectrum from 11.827 to 11.838 eV with a center energy of 11.8317 eV with a full width at half maximum (FWHM) of 0.005 eV. This indicates that the C_3 molecules are excited to Rydberg states in the energy range and are subsequently ionized by the R_{PFI} Stark field.

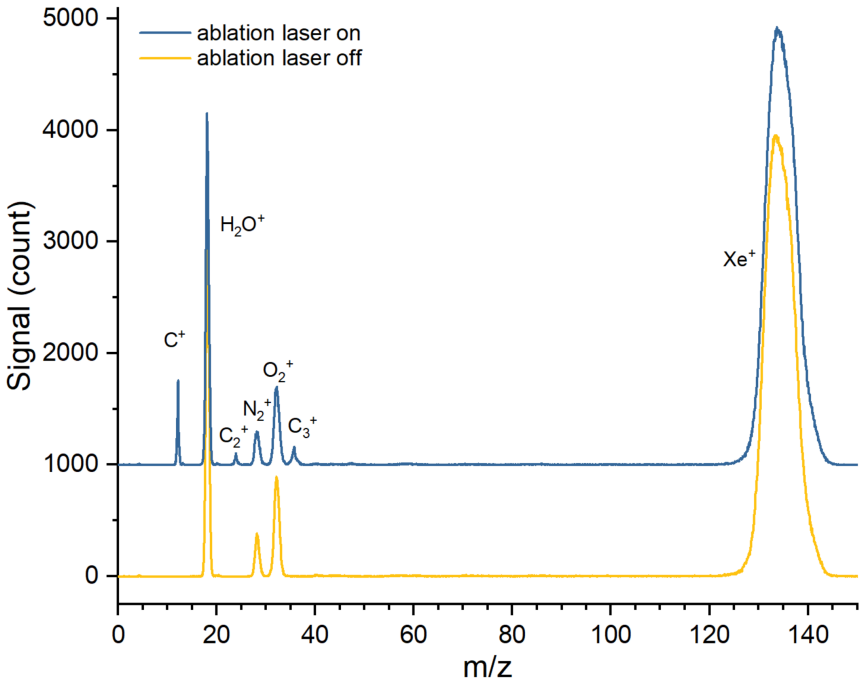

FIGURE 6.2. TOF spectrum when the ablation laser is on (blue) and off (yellow). The peaks of H_2O^+, N_2^+, and O_2^+ are from residual air in the system, the peak Xe^+ is from the Xe leaking from the four-wave mixing chamber. The blue trace is offset vertically by a 1000 counts.

Under the Stark field, the ionization energy of a molecule is shifted by

$$\Delta E = \frac{a}{2}\left(\sqrt{F_R} + \sqrt{F_{PFI}}\right) = IE - IE_{PFI}. \tag{6.1}$$

In a previous study, the coefficient a of this apparatus has been calibrated as $3.72\pm0.07\,\mathrm{cm}^{-1}/(\mathrm{V/cm})^{1/2}$ by comparing the measured PFI-PI IE values of Ar and V recorded under varying F_R and F_{PFI} with known values (Chang et al., 2019a). The F_R and F_{PFI} used in this experiment are 3.5 and 75 V/cm, respectively, yielding a field-free IE of

$$IE = 11.8317\,\mathrm{eV} + \frac{3.72}{2}\left(\sqrt{3.5} + \sqrt{75}\right)\,\mathrm{cm}^{-1} = 11.8317\,\mathrm{eV} + 19.6\,\mathrm{cm}^{-1} = 11.8341\,\mathrm{eV}. \tag{6.2}$$

The uncertainty mainly comes from the FWHM of the peak which is 0.0025 eV. Low-lying vibrational excited states may contribute to the line shape. Therefore, the measured IE is conservatively reported as 11.8341 ± 0.0025 eV.

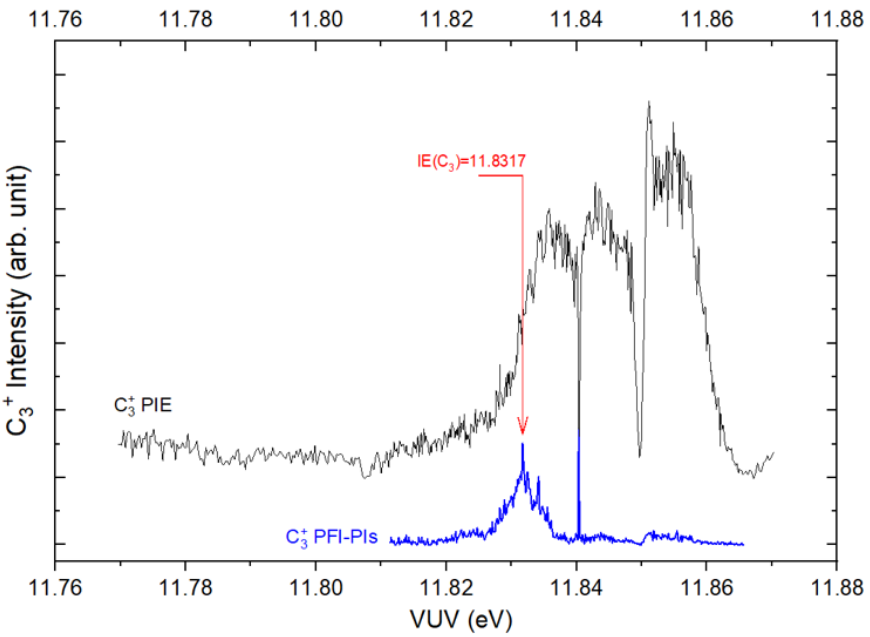

FIGURE 6.3. (black) PIE spectrum scanning VUV sum frequency in energy region 11.77-11.87 eV. (blue) PFI-PIs spectra scanning VUV sum frequency in energy region of 11.81-11.87 eV. The experimental ionization energy under Stark field is marked. The black trace is offset vertically for clarity.

Ab initio of the IE of C_3 are difficult owing to its quasi-linearity and large-amplitude bending motions of C_3 (Varandas & Rocha, 2018) together with the aforementioned complicity of the C_3^+ geometry (Van Orden & Saykally, 1998). Although fully understanding the behavior of C_3 ground and low-lying excited states requires treatment of the strong Renner-Teller vibronic interactions, it is widely accepted that the ground $\tilde{X}\,^1\Sigma_g^+$ state has a linear geometry. The $C-C$ bond length is calculated as 1.309 Å (Varandas & Rocha, 2018), which is consistent with the measured value of 1.297±0.001 Å (Hinkle et al., 1988). The theoretical treatment of C_3^+ is challenging because of symmetry breaking problems. As previously discussed, the ground state of C_3^+ is bent with $^2B_2$ symmetry, but a $^2A_1$ state and the linear $\tilde{X}\,^2\Sigma_u^+$ state both have minimum within ~0.1 eV of the $^2B_2$ state (Nicolas et al., 2006). The equilibrium bond angles $\angle CCC$ are calculated as ~65° for $\tilde{X}\,^2B_2$ and ~57° $\tilde{X}\,^2A_1$. Strictly, the IE of C_3 should be defined as the energy from the C_3 $\tilde{X}\,^1\Sigma_g^+$ to the C_3^+ $\tilde{X}\,^2B_2$ state. In the experimental study, Nicolas et al. (2006) interpreted their measured PIE curve as the ionization process to C_3^+ $\tilde{X}\,^2\Sigma_u^+$ state from Franck-Condon arguments. We likewise assign our measured value to this ionization process for the same reason.

There are no theoretical studies reporting vibrational frequencies of C_3^+ to date, to the author's knowledge. In the experiment, the VUV laser was scanned as high as 12.318 eV, which is 0.486 eV (3920 cm^{-1}) above the IE peak we observed, and as low as 11.730 eV. No signals were detected from C_3^+ vibrational states, likely also due to poor Franck-Condon overlap.

6.4. Conclusion

A laser ablation source was tested for production of C_2 for photodissociation studies. The TOF spectrum shows the C_2 and C_3 are generated successfully when the laser ablates the rotating graphite rod. The photoionization of C_3 has been rarely studied due to its complicated structure. Because the laser ablation source readily produce C_3, we conducted PFI-PI experiments to improve the accuracy of the previous reported ionization energy of C_3. From the PFI-PI spectrum, a photoexcitation peak was observed clearly. Combining the photoexcitation energy of the PFI-PI and the calculated shift under the Stark field, we reported the new IE as 11.8341±0.0025 eV between the C_3 $\tilde{X}\,^1\Sigma_g^+$ and the C_3^+ $\tilde{X}\,^2\Sigma_u^+$ states. The accurate determination of IE from C_3 to the ground C_3^+ bent state requires further experimental and theoretical studies.

Bibliography

Agúndez, M., & Wakelam, V. 2013, Chemical Reviews, 113, 8710

Ahearn, M. F., Schleicher, D. G., & Feldman, P. D. 1983, The Astrophysical Journal, 274, L99

Almeida, A. A. D., & Singh, P. D. 1986, Earth, Moon, and Planets, 36, 117

Amiot, C., Chauville, J., & Maillard, J. P. 1979, Journal of Molecular Spectroscopy, 75, 19

Asplund, M., Grevesse, N., Sauval, A. J., & Scott, P. 2009, Annual Review of Astronomy and Astrophysics, 47, 481

Babb, J. F., Smyth, R. T., & McLaughlin, B. M. 2019, The Astrophysical Journal, 876, 38

Baer, M. 2006, Beyond Born-Oppenheimer: Conical Intersections and Electronic Non-Adiabatic Coupling Terms (Hoboken, N.J: Wiley)

Ballik, E. A., & Ramsay, D. A. 1963, The Astrophysical Journal, 137, 84

Barrow, R., Dixon, R., Lagerqvist, A., & Wright, C. 1960, arkiv foer Fysik, 18, 543

Belau, L., Wheeler, S. E., Ticknor, B. W., et al. 2007, Journal of the American Chemical Society, 129, 10229

Bell, S., Ng, T. L., & Suggitt, C. 1972, Journal of Molecular Spectroscopy, 44, 267

Bernath, P. F. 2016, Spectra of Atoms and Molecules, third edition edn. (Oxford ; New York: Oxford University Press)

Blunt, V. M., Lin, H., Sorkhabi, O., & Jackson, W. M. 1995, Journal of Molecular Spectroscopy, 174, 274

Bornhauser, P., Marquardt, R., Gourlaouen, C., et al. 2015, The Journal of Chemical Physics, 142, 094313

Bruna, P. J., & Grein, F. 2001, Can. J. Phys., 79, 653

Bruna, P. J., Kammer, W. E., & Vasudevan, K. 1975, Chemical Physics, 9, 91

Bunker, P. R. 1968, Journal of Molecular Spectroscopy, 28, 422

Bunn, H. A., Schultz, C. P., Jernigan, C. M., & Widicus Weaver, S. L. 2020, The Journal of Physical Chemistry A, 124, 10838

Canaves, M. V., de Almeida, A. A., Boice, D. C., & Sanzovo, G. C. 2007, Advances in Space Research, 39, 451

Carlson, T. A., Copley, J., Durić, N., Erman, P., & Larsson, M. 1979, Chemical Physics, 42, 81

Cecchi-Pestellini, C., & Dalgarno, A. 2002, Mon. Not. R. Astron. Soc., 331, L31

Cernicharo, J., Goicoechea, J. R., & Caux, E. 2000, The Astrophysical Journal, 534, L199

Chaffee, F. H., Lutz, B. L., Black, J. H., Bout, P. A. V., & Snell, R. L. 1980, Symposium - International Astronomical Union, 87, 263

Chang, Y.-C., Lam, C.-S., Reed, B., et al. 2009, The Journal of Physical Chemistry A, 113, 4242

Chang, Y. C., Xiong, B., Xu, Y., & Ng, C.-Y. 2019a, The Journal of Physical Chemistry A, 123, 2310

Chang, Y. C., Xu, Y., Lu, Z., Xu, H., & Ng, C. Y. 2012, The Journal of Chemical Physics, 137, 104202

Chang, Y. C., Xu, Y., & Ng, C.-Y. 2019b, Physical Chemistry Chemical Physics, 21, 6868

Chase, M. W., ed. 1998, NIST-JANAF Thermochemical Tables, 4th edn. (Washington, DC : New York: American Chemical Society ; American Institute of Physics for the National Institute of Standards and Technology)

Chen, W., Kawaguchi, K., Bernath, P. F., & Tang, J. 2015, The Journal of Chemical Physics, 142, 064317

—. 2016, The Journal of Chemical Physics, 144, 064301

Cochran, A. L., Levasseur-Regourd, A.-C., Cordiner, M., et al. 2015, Space Science Reviews, 197, 9

Coppens, P., & Drowart, J. 1995, Chemical Physics Letters, 243, 108

Corby, J. F., McGuire, B. A., Herbst, E., & Remijan, A. J. 2018, Astronomy & Astrophysics, 610, A10

Cossart, D., & Bergeman, T. 1976, The Journal of Chemical Physics, 65, 5462

Cox, N. L. J., & Patat, F. 2014, Astronomy & Astrophysics, 565, A61

Crawford, F. H., & Shurcliff, W. A. 1934, Phys. Rev., 45, 860

Dawes, R., Jasper, A. W., Tao, C., et al. 2010, The Journal of Physical Chemistry Letters, 1, 641

Deskevich, M. P., Nesbitt, D. J., & Werner, H.-J. 2004, The Journal of Chemical Physics, 120, 7281

Despois, D., Biver, N., Bockelée-Morvan, D., & Crovisier, J. 2005, Proceedings of the International Astronomical Union, 1, 469

Destree, J. D., Snow, T. P., & Black, J. H. 2009, Astrophys. J., 693, 804

Dieke, G. H., & Lochte-Holtgreven, W. 1930, Zeitschrift für Physik, 62, 767

Dietz, T. G., Duncan, M. A., Powers, D. E., & Smalley, R. E. 1981, The Journal of Chemical Physics, 74, 6511

Donati, G. B. 1864, Astronomische Nachrichten, 62, 375

Donovan, R. J., Husain, D., & Stevenson, C. D. 1970, Trans. Faraday Soc., 66, 1

Douay, M., Nietmann, R., & Bernath, P. F. 1988, Journal of Molecular Spectroscopy, 131, 261

Draine, B. T. 1978, The Astrophysical Journal Supplement Series, 36, 595

Drdla, K., Knapp, G. R., & van Dishoeck, E. F. 1989, Astrophys. J., 345, 815

Drowart, J., Burns, R. P., DeMaria, G., & Inghram, M. G. 1959, The Journal of Chemical Physics, 31, 1131

Druard, C., & Wakelam, V. 2012, Monthly Notices of the Royal Astronomical Society, 426, 354

Dunning, T. H. 1989, J. Chem. Phys., 90, 1007

Dunning, T. H., Peterson, K. A., & Wilson, A. K. 2001, The Journal of Chemical Physics, 114, 9244

Federman, S. R., Fritts, M., Cheng, S., et al. 2001, The Astrophysical Journal Supplement Series, 134, 133

Federman, S. R., & Huntress, W. T., J. 1989, Astrophys. J., 338, 140

Field, R. W., & Bergeman, T. H. 1971, The Journal of Chemical Physics, 54, 2936

Fox, J. G., & Herzberg, G. 1937, Physical Review, 52, 638

Freymark, H. 1950, Annalen der Physik, 443, 221

Friedman, R. S., Du, M. L., & Dalgarno, A. 1990, The Journal of Chemical Physics, 93, 2375

Fura, A., Turecˇek, F., & McLafferty, F. W. 2002, International Journal of Mass Spectrometry, 16

Gao, H., Song, Y., Chang, Y. C., et al. 2013a, J. Phys. Chem. A, 117, 6185

Gao, H., Song, Y., Jackson, W. M., & Ng, C. Y. 2013b, J. Chem. Phys., 138, 191102

Gauyacq, D., & Horani, M. 1978, Canadian Journal of Physics, 56, 587

Gibson, S. 2016, Pydiatomic: Pydiatomic Initial Release, Zenodo

Gibson, S. T., & Lewis, B. R. 1996, Journal of Electron Spectroscopy and Related Phenomena, 80, 9

Goodwin, P. M., & Cool, T. A. 1988, The Journal of Chemical Physics, 89, 6600

—. 1989, Journal of Molecular Spectroscopy, 133, 230

Gupta, S. K., & Gingerich, K. A. 1979, The Journal of Chemical Physics, 71, 3072

H.-J. Werner, & P. J. Knowles. 2015, Molpro Users Manual

Hansson, A., & Watson, J. K. 2005, Journal of Molecular Spectroscopy, 233, 169

Harper, O. J., Boyé-Péronne, S., Garcia, G. A., et al. 2020, The Journal of Chemical Physics, 152, 041105

Heays, A., Theses, A. D., & of Physical Sciences, A. N. U. R. S. 2010, Thesis

Heays, A. N., Bosman, A. D., & van Dishoeck, E. F. 2017, Astronomy & Astrophysics, 602, A105

Heays, A. N., Lewis, B. R., Gibson, S. T., Stark, G., & de Oliveira, N. 2015, EPJ Web of Conferences, 84, 03004

Heithausen, A., Corneliussen, U., & Grossmann, V. 1998, Astronomy and Astrophysics, 330, 311

Herbst, E., & van Dishoeck, E. F. 2009, Annual Review of Astronomy and Astrophysics, 47, 427

Herczeg, G. J., Wood, B. E., Linsky, J. L., Valenti, J. A., & Johns-Krull, C. M. 2004, The Astrophysical Journal, 607, 369

Herzberg, G., Lagerqvist, A., & Malmberg, C. 1969, Canadian Journal of Physics, 47, 2735

Herzberg, G., & Spinks, J. W. T. 1950, Molecular Spectra and Molecular Structure: Diatomic Molecules, Vol. 1 (van Nostrand)

Herzberg, G., & Sutton, R. B. 1940, Canadian Journal of Research, 18a, 74

Hilbig, R., & Wallenstein, R. 1982, Applied Optics, 21, 913

Hilborn, R. C. 1982, American Journal of Physics, 50, 982

Hinkle, K. W., Keady, J. J., & Bernath, P. F. 1988, Science, 241, 1319

Huber, K. P., & Herzberg, G. 1979, Molecular Spectra and Molecular Structure (Boston, MA: Springer US)

Huebner, W. F., & Mukherjee, J. 2015, Planetary and Space Science, 106, 11

Huggins, W. 1882, Proceedings of the Royal Society of London, 33, 1

Hupe, R. C., Sheffer, Y., & Federman, S. R. 2012, The Astrophysical Journal, 761, 38

Jackson, W. M. 1976, J. Photochem., 5, 107

Jackson, W. M., J. B. Halpern, P. D. Feldman, & J. Rahe. 1982, Astronomy & Astrophysics, 107, 385

Jackson, W. M., & Scodinu, A. 2004, in The New Rosetta Targets: Observations, Simulations and Instrument Performances, ed. L. Colangeli, E. M. Epifani, & P. Palumbo, Astrophysics and Space Science Library (Dordrecht: Springer Netherlands), 85–95

Jiménez-Escobar, A., Caro, G. M. M., Ciaravella, A., et al. 2012, The Astrophysical Journal Letters, 751, L40

Joester, J. A., Nakajima, M., Reilly, N. J., et al. 2007, The Journal of Chemical Physics, 127, 214303

Johnson, B. R. 1978, The Journal of Chemical Physics, 69, 4678

Johnson, J. R., Fink, U., & Larson, H. P. 1983, Astrophys. J., 270, 769

Kaczmarczyk, G. 2000, Acta Astron., 50, 151

Kendall, R. A., Dunning, T. H., & Harrison, R. J. 1992, The Journal of Chemical Physics, 96, 6796

Kewley, R., Sastry, K. V. L. N., Winnewisser, M., & Gordy, W. 1963, The Journal of Chemical Physics, 39, 2856

Kirby, K. P., & Van Dishoeck, E. F. 1989, in Advances in Atomic and Molecular Physics, ed. D. Bates & B. Bederson, Vol. 25 (Academic Press), 437–476

Knowles, P. J., & Werner, H.-J. 1985, Chem. Phys. Letters, 115, 259

—. 1988, Chem. Phys. Letters, 145, 514

—. 1992, tca, 84, 95

Kohl, F. J., & Stearns, C. A. 1970, The Journal of Chemical Physics, 52, 6310

Kokkin, D. L., Bacskay, G. B., & Schmidt, T. W. 2007, The Journal of Chemical Physics, 126, 084302

Kokkin, D. L., Reilly, N. J., Morris, C. W., et al. 2006, The Journal of Chemical Physics, 125, 231101

Krechkivska, O., Bacskay, G. B., Troy, T. P., et al. 2015, The Journal of Physical Chemistry A, 119, 12102

Krechkivska, O., Bacskay, G. B., Welsh, B. A., et al. 2016, The Journal of Chemical Physics, 144, 144305

Krechkivska, O., Welsh, B. A., Bacskay, G. B., et al. 2017, The Journal of Chemical Physics, 146, 134306

Krechkivska, O., Welsh, B. A., Fréreux, J. N., et al. 2018, Journal of Molecular Spectroscopy, 344, 1

Lambert, D. L., & Mallia, E. A. 1974, Bulletin of the Astronomical Institute of Czechoslovakia, 26, 216

Lambert, D. L., Sheffer, Y., & Federman, S. R. 1995, The Astrophysical Journal, 438, 740

Landsverk, O. G. 1939, Physical Review, 56, 769

Langhoff, S. R., & Davidson, E. R. 1974, International Journal of Quantum Chemistry, 8, 61

Le Gal, R., Öberg, K. I., Loomis, R. A., Pegues, J., & Bergner, J. B. 2019, The Astrophysical Journal, 876, 72

Le Roy, L., Altwegg, K., Balsiger, H., et al. 2015, Astronomy & Astrophysics, 583, A1

Le Roy, R. J. 1989, Computer Physics Communications, 52, 383

Lefebvre-Brion, H., & Field, R. W. 2004, The Spectra and Dynamics of Diatomic Molecules, rev. and enlarged ed edn. (Amsterdam: Elsevier Acad. Press)

Lewis, B. R., Gibson, S. T., Hawes, F. T., & Torop, L. W. 2001, Physics and Chemistry of the Earth, Part C: Solar, Terrestrial & Planetary Science, 26, 519

Lewis, B. R., Gibson, S. T., Stark, G., & Heays, A. N. 2018, The Journal of Chemical Physics, 148, 244303

Li, R., Wei, C., Sun, Q., et al. 2013, The Journal of Physical Chemistry A, 117, 2373

Li, Z., Zhao, M., Xie, T., et al. 2021, The Journal of Physical Chemistry Letters, 12, 844

Lique, F. 2019, Gas-Phase Chemistry in Space (IOP Publishing)

Loison, J.-C., Halvick, P., Bergeat, A., Hickson, K. M., & Wakelam, V. 2012, Monthly Notices of the Royal Astronomical Society, 421, 1476

Lovas, F. J., & Krupenie, P. H. 1974, Journal of Physical and Chemical Reference Data, 3, 245

Lu, Z., Chang, Y. C., Yin, Q.-Z., Ng, C. Y., & Jackson, W. M. 2014, Science, 346, 61

Lu, Z., Chang, Y. C., Benitez, Y., et al. 2015, Phys. Chem. Chem. Phys., 17, 11752

Lucas, R., & Liszt, H. S. 2002, Astron.Astrophys., 384, 1054

Mahon, C. A., Stampanoni, A., Luque, J., & Crosley, D. R. 1997, Journal of Molecular Spectroscopy, 183, 18

Maier, J. P., Lakin, N. M., Walker, G. A. H., & Bohlender, D. A. 2001, The Astrophysical Journal, 553, 267

McElroy, D., Walsh, C., Markwick, A. J., et al. 2013, Astronomy & Astrophysics, 550, A36

McGuire, B. A. 2018, The Astrophysical Journal Supplement Series, 239, 17

McKemmish, L. K., Syme, A.-M., Borsovszky, J., et al. 2020, Monthly Notices of the Royal Astronomical Society

McQuinn, K. B. W., Simon, R., Law, C. J., et al. 2002, The Astrophysical Journal, 576, 274

Messerle, G., & Krauss, L. 1967, Zeitschrift für Naturforschung A, 22, 2015

Mies, F. H. 1980, Molecular Physics, 41, 953

Mockler, R. C., & Bird, G. R. 1955, Physical Review, 98, 1837

Moltzen, E. K., Klabunde, K. J., & Senning, A. 1988, Chemical Reviews, 88, 391

Mookerjea, B., Giesen, T., Stutzki, J., et al. 2010, Astronomy & Astrophysics, 521, L13

Nakajima, M., Joester, J. A., Page, N. I., et al. 2009, The Journal of Chemical Physics, 131, 044301

Nakamura, H. 2002, Nonadiabatic Transition: Concepts, Basic Theories and Applications (River Edge, NJ: World Scientific)

Neufeld, D. A., Godard, B., Gerin, M., et al. 2015, Astron. Astrophys., 577, A49

Nicolas, C., Shu, J., Peterka, D. S., et al. 2006, Journal of the American Chemical Society, 128, 220

Orlova, G., & Goddard, J. D. 2002, Chemical Physics Letters, 6

Ornellas, F. R. 1998, Chemical Physics Letters, 296, 25

Pattillo, R. J., Cieszewski, R., P. C. Stancil, et al. 2018, The Astrophysical Journal, 858, 10

Penzias, A. A., Solomon, P. M., Wilson, R. W., & Jefferts, K. B. 1971, Astrophys. J., 168, L53

Phillips, J. G. 1948, Astrophysical Journal, 107, 389

—. 1949, The Astrophysical Journal, 110, 73

—. 1950, The Astrophysical Journal, 112, 131

Pouilly, B., Robbe, J. M., Schamps, J., & Roueff, E. 1983, Journal of Physics B: Atomic and Molecular Physics, 16, 437

Prasad, S. S., & Huntress, Jr., W. T. 1980, The Astrophysical Journal Supplement Series, 43, 1

Ramanathan, R., Zimmerman, J. A., & Eyler, J. R. 1993, The Journal of Chemical Physics, 98, 7838

Reed, B., Lam, C.-S., Chang, Y.-C., et al. 2009, The Astrophysical Journal, 693, 940

Rohlfing, E. A., Cox, D. M., & Kaldor, A. 1984, The Journal of Chemical Physics, 81, 3322

Roueff, E., Felenbok, P., Black, J. H., & Gry, C. 2002, Astronomy & Astrophysics, 384, 629

Samanta, K., Beames, J. M., Lester, M. I., & Subotnik, J. E. 2014, The Journal of Chemical Physics, 141, 134303

Scappini, F., Cecchi-Pestellini, C., Casu, S., & Olberg, M. 2007, Astron. Astrophys., 466, 243

Schaefer, H. F., ed. 1977, Applications of Electronic Structure Theory, Modern Theoretical Chemistry No. 4 (New York: Plenum Press)

Schindhelm, E., France, K., Herczeg, G. J., et al. 2012, The Astrophysical Journal, 756, L23

Schinke, R. 1995, Photodissociation Dynamics: Spectroscopy and Fragmentation of Small Polyatomic Molecules, 1st edn., Cambridge Monographs on Atomic, Molecular and Chemical Physics No. 1 (Cambridge: Cambridge University Press)

Schmidt, H., von Vangerow, J., Stienkemeier, F., et al. 2015, The Journal of Chemical Physics, 142, 044303

Schmidt, T. W. 2021, Accounts of Chemical Research, 54, 481

Schmidt, T. W., & Bacskay, G. B. 2007, The Journal of Chemical Physics, 127, 234310

Schöier, F. L., van der Tak, F. F. S., van Dishoeck, E. F., & Black, J. H. 2005, Astronomy & Astrophysics, 432, 369

Semenov, D., Favre, C., Fedele, D., et al. 2018, Astronomy & Astrophysics, 617, A28

Shaik, S., Danovich, D., & Hiberty, P. C. 2017, Computational and Theoretical Chemistry, 1116, 242

Shaik, S., Danovich, D., Wu, W., et al. 2012, Nature Chemistry, 4, 195

Shi, D., Niu, X., Sun, J., & Zhu, Z. 2013, The Journal of Chemical Physics, 139, 044306

Shi, D., Zhang, X., Sun, J., & Zhu, Z. 2011, Molecular Physics, 109, 1453

Smith, I. W. 2011, Annual Review of Astronomy and Astrophysics, 49, 29

Snow, T. P. 1978, Astrophys. J., 220, L93

Snow, T. P., & McCall, B. J. 2006, Annual Review of Astronomy and Astrophysics, 44, 367

Song, Y., Gao, H., Chang, Y. C., et al. 2016, Astrophys. J., 819, 23

Sonnentrucker, P., Welty, D. E., Thorburn, J. A., & York, D. G. 2007, Astrophys. J. Suppl. Ser., 168, 58

Sorkhabi, O., Blunt, V. M., Lin, H., et al. 1997, The Journal of Chemical Physics, 107, 9842

Souza, S. P., & Lutz, B. L. 1977, Astrophys. J., 216, L49

Stark, G., Yoshino, K., & Smith, P. L. 1987, J. Mol. Spectrosc., 124, 420

Stockhausen, R. E., & Osterbrock, D. E. 1965, Astrophys. J., 141, 287

Taylor, G. W., Setser, D. W., & Coxon, J. A. 1972, Journal of Molecular Spectroscopy, 44, 108

Tewarson, A., & Palmer, H. B. 1968, Journal of Molecular Spectroscopy, 27, 246

Tielens, A. G. G. M. 2013, Reviews of Modern Physics, 85, 1021

Torop, L., McCoy, D. G., Blake, A. J., Wang, J., & Scholz, T. 1987, Journal of Quantitative Spectroscopy and Radiative Transfer, 38, 9

Trabelsi, T., Al-Mogren, M. M., Hochlaf, M., & Francisco, J. S. 2018, The Journal of Chemical Physics, 149, 064304

van der Tak, F. F. S., Boonman, A. M. S., Braakman, R., & van Dishoeck, E. F. 2003, Astronomy & Astrophysics, 412, 133

van Dishoeck, E. F., & Black, J. H. 1982, The Astrophysical Journal, 258, 533

van Dishoeck, E. F., Jonkheid, B., & van Hemert, M. C. 2006, Faraday Discussions, 133, 231

van Dishoeck, E. F., van Hemert, M. C., Allison, A. C., & Dalgarno, A. 1984, The Journal of Chemical Physics, 81, 5709

van Hemert, M. C., & van Dishoeck, E. F. 2008, Chemical Physics, 343, 292

Van Orden, A., & Saykally, R. J. 1998, Chemical Reviews, 98, 2313

Varandas, A. J. C., & Rocha, C. M. R. 2018, Philosophical Transactions of the Royal Society A: Mathematical, Physical and Engineering Sciences, 376, 20170145

Veseth, L. 1970, Theoretica chimica acta, 18, 368

Vidal, T. H. G., Loison, J.-C., Jaziri, A. Y., et al. 2017, Monthly Notices of the Royal Astronomical Society, 469, 435

Wakelam, V., Hersant, F., & Herpin, F. 2011, Astronomy & Astrophysics, 529, A112

Wakelam, V., Loison, J.-C., Herbst, E., et al. 2015, The Astrophysical Journal Supplement Series, 217, 20

Watson, J. K. G. 2008, Journal of Molecular Spectroscopy, 252, 5

Wehres, N., Romanzin, C., Linnartz, H., Winckel, H. V., & Tielens, A. G. G. M. 2010, Astronomy & Astrophysics, 518, A36

Welsh, B. A., Krechkivska, O., Nauta, K., et al. 2017, The Journal of Chemical Physics, 147, 024305

Werner, H.-J., & Knowles, P. J. 1985, J. Chem. Phys., 82, 5053

—. 1988, J. Chem. Phys., 89, 5803

Werner, H.-J., Knowles, P. J., Knizia, G., Manby, F. R., & Schütz, M. 2012, WIREs Comput Mol Sci, 2, 242

Werner, H.-J., & Meyer, W. 1981, The Journal of Chemical Physics, 74, 5802

Wollaston, W. H. 1802, Philosophical Transactions of the Royal Society of London, 92, 365

Woon, D. E., & Dunning, T. H. 1993, The Journal of Chemical Physics, 98, 1358

—. 1995, The Journal of Chemical Physics, 103, 4572

Xu, H., & Joens, J. A. 1993, Geophysical Research Letters, 20, 1035

Xu, Z., Luo, N., Federman, S. R., et al. 2019, The Astrophysical Journal, 882, 86

Xue, J., Yuan, X., Li, R., et al. 2020, Spectrochimica Acta Part A: Molecular and Biomolecular Spectroscopy, 241, 118679

Yamamoto, S. 2017, Introduction to Astrochemistry: Chemical Evolution from Interstellar Clouds to Star and Planet Formation, Astronomy and Astrophysics Library (Tokyo: Springer)

Yurchenko, S. N., Lodi, L., Tennyson, J., & Stolyarov, A. V. 2016, Computer Physics Communications, 202, 262. https://arxiv.org/abs/1601.06531

Zener, C. 1932, Proceedings of the Royal Society A: Mathematical, Physical and Engineering Sciences, 137, 696

Zhou, J., Jones, B., Yang, X., Jackson, W. M., & Ng, C. Y. 2008, The Journal of Chemical Physics, 128, 014305

Zuckerman, B., Morris, M., Palmer, P., & Turner, B. E. 1972, Astrophys. J., 173, L125